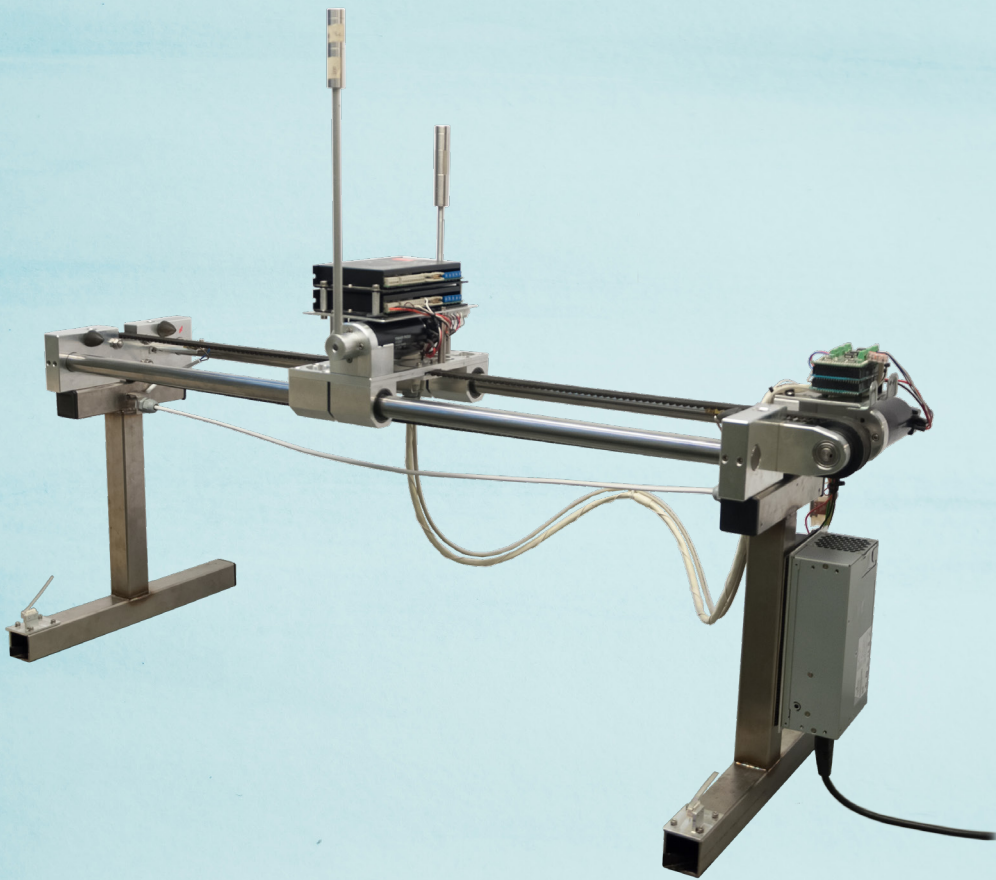


# SWING-UP AND STABILIZATION OF A CART PENDULUM AND TWIN PENDULUM SYSTEM

Using Nonlinear Control Strategies



**Niels Skov Vestergaard**

Master Thesis  
Control & Automation



**AALBORG UNIVERSITY**  
DENMARK



**AALBORG UNIVERSITY**  
STUDENT REPORT

**Master Thesis**

**Control and Automation**

Department of Electronic Systems

Fredrik Bajers Vej 7C

9220 Aalborg

**Title:**

Swing-Up and Stabilization of a Cart Pendulum and Twin Pendulum System

**Subtitle:**

Using Nonlinear Control Strategies

**Theme:**

Nonlinear Control

**Project Period:**

Autumn 2018

**Participants:**

Niels Skov Vestergaard

**Supervisor:**

John-Josef Leth

**Pages:** 76

**Concluded:** 2019-01-16

**Synopsis:**

This project is concerned with developing nonlinear control strategies for a cart pendulum system set-up provided in the Control and Automation Lab by Aalborg University (AAU).

The project is two part. The first part considers the cart pendulum system and with an additional pendulum attached the second part considered the twin pendulum system. The objective of both parts is to swing up, catch and stabilize the pendulums in upright position.

In the first part three energy based swing-up controllers are designed for the cart pendulum system. A sliding mode controller is developed to catch and stabilize the pendulum. One of the energy based swing-up strategies is implemented on the test setup along with the sliding mode controller.

In the second part knowledge from the first part is used to develop a swing-up strategy for the twin pendulum system. A Linear Quadratic Regulator (LQR) is designed as the stabilizing controller. The controllers are implemented and finally a Kalman filter is designed to estimate the unmeasured states of the twin pendulum system.

*Publication of this report's contents (including citation) without permission from the author is prohibited*



# Preface

This thesis made under the Control and Automation Master's Program at Aalborg University. The thesis was conducted in the fall of 2018 and supervised by John-Josef Leth, associate professor at Aalborg University.

The focus of the thesis has been to design and implement nonlinear control strategies for the cart pendulum and twin pendulum system. Each system is addressed in its own *part* of the thesis.

The reader is expected to have an engineering level knowledge within mathematics and physics along with some prior knowledge within nonlinear control theory.

Special thanks to Kirstine Juul Elbæk, Michael Wodstrup Vandborg and Rasmus Gundorff Sæderup who were kind enough to help with revision of the text and Rasmus in addition for graphical design of the cover.

**Text by:**

---

Niels Skov Vestergaard

# Contents

<b>1</b>	<b>Introduction</b>	<b>1</b>
	<b>Part I Cart Pendulum</b>	<b>2</b>
<b>2</b>	<b>System and Model</b>	<b>3</b>
2.1	System . . . . .	3
2.2	Model . . . . .	5
<b>3</b>	<b>Swing-Up Design</b>	<b>8</b>
3.1	Energy Control . . . . .	9
3.2	Sign-Based Energy Control . . . . .	16
3.3	Sat-Based Energy Control . . . . .	17
3.4	Cart Position and Velocity Control . . . . .	20
<b>4</b>	<b>Stabilization</b>	<b>24</b>
<b>5</b>	<b>Implementation</b>	<b>34</b>
5.1	Cart Friction and Mass Estimation . . . . .	34
5.2	Pendulum Friction . . . . .	36
5.3	MA Filter Design . . . . .	37
<b>6</b>	<b>Results</b>	<b>40</b>
	<b>Part II Twin Pendulum</b>	<b>46</b>
<b>7</b>	<b>System and Model</b>	<b>47</b>
7.1	System Addition . . . . .	47
7.2	Model . . . . .	50
<b>8</b>	<b>Swing-Up Design</b>	<b>54</b>
<b>9</b>	<b>Stabilization</b>	<b>58</b>
<b>10</b>	<b>State Estimation</b>	<b>62</b>
<b>11</b>	<b>Results</b>	<b>67</b>
<b>12</b>	<b>Conclusion</b>	<b>73</b>

# 1 | Introduction

This thesis is concerned with investigating, developing and applying nonlinear control strategies to a cart pendulum and twin pendulum system. Since both these systems have less actuators than degrees of freedom, they fall into the category of underactuated systems. For the cart pendulum a motor controls the cart while the pendulum can only be acted on through the system dynamics. Adding a second pendulum to get the twin pendulum system means the system only has one actuated of the now three degrees of freedom.

The control objective is to develop a swing-up procedure which brings the pendulums to the upright naturally unstable equilibrium. The concept used for the swing-up controllers is to bring the mechanical energy of each pendulum to match its potential energy in the unstable equilibrium.

Once the pendulums are close to the upright position, a catch controller is deployed which then stabilizes the pendulums. For the cart pendulum system a sliding mode controller is developed and for the twin pendulum a Linear Quadratic Regulator (LQR) is designed.

Though these two systems may not directly have other physical application than demonstration of control technique, they are extremely useful for studying control problems concerned with underactuated systems.

In general the study of underactuated robotics uses the natural dynamics of the mechanical systems, attempting to achieve extraordinary performance in terms of speed, efficiency or robustness [1]. An example of an underactuated system is a walking robot. From a simplified point of view the supporting leg can be seen as an inverted pendulum once the other leg leaves the ground. Popular walking robots such as ASIMO makes use of high-gain feedback in an attempt to cancel out the natural dynamics of the system. This is about 20 times less efficient than a human gait and results in stiff and unnatural walking [1]. This approach also limits the operating range and thus versatility of the system [1]. While developing a robust, versatile and natural walking robot is certainly not a simple problem, it is clear that exploiting natural dynamics by underactuation is a considerable step on the way.

So understanding and applying nonlinear control strategies to an isolated case like the cart pendulum and twin pendulum system could play an important role in the future of controlled underactuated systems.

# Part I

## Cart Pendulum

## 2 | System and Model

A brief overview of the relevant system for *Part 1* is presented in this chapter along with a model of the system.

### 2.1 System

A setup is provided by the Control and Automation Department at AAU, see Figure 2.1.

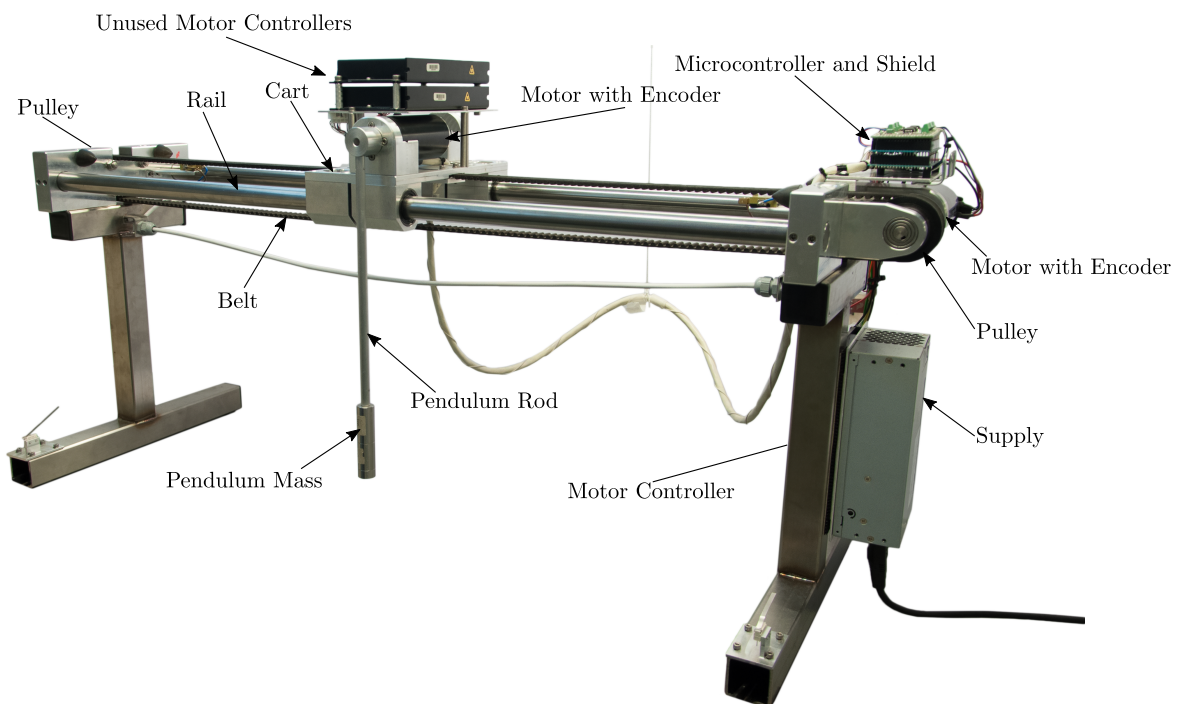


**Figure 2.1:** The setup provided by AAU. The motor controller in use is not directly visible in this picture as it is mounted behind the power supply.

As seen in Figure 2.1, the belt is attached to pulleys, one of which is driven by a brushed Maxon 370356 DC motor [2]. Another of these maxon motors is mounted on the pendulum but is disconnected and just used as a joint in this project. Both motors are fitted with an HEDS 5540 optical quadrature encoder allowing for relative position and angle of the cart and pendulum respectively [3].

The motor driving the belt is controlled using a Maxon ADS 50/10 motor controller configured in current control mode. The motor controller takes a  $\pm 10\text{V}$  input signal which then determines the armature current,  $i_a$ , see [4].

The primary control unit is a Teensy 3.6 microcontroller board. To program the board

through the onboard USB connection a bootloader is used along with the Teensyduino add-on for the Arduino IDE [5].

The encoders are decoded on a shield using Avago HCTL-2021-PLC decoders and read through an 8 bit parallel data bus on the microcontroller board resulting in 2000 tics pr. revolution. This ensures a resolution for the pendulum angle,  $\theta$ , of  $2\pi/2000 = \pi \times 10^{-3}$  rad/tic and  $2\pi r/2000 = 2\pi \cdot 0.028/2000 \approx 0.088 \times 10^{-3}$  m/tic for the cart position,  $x$ , see [6].

The supply circuit on the microcontroller board is powered by 5V which is regulated to 3.3 V resulting in a 0–3.3 V range for the 12 bit analog output [7]. This output is used to provide the motor controller with an armature current reference, thus, the microcontroller analog output is amplified through the shield to meet the  $\pm 10$  V input requirement of the motor controller [8].

The following relation between analog 12 bit output values,  $\text{bit}_{\text{DAC}}$ , from the microcontroller and armature current in the motor was found by a previous project group [8],

$$\text{bit}_{\text{DAC}} = 105.78 \cdot i_a + 1970 \quad , \quad (2.1)$$

and as a result of a force test, see [9], Equation 2.1 was corrected to,

$$\text{bit}_{\text{DAC}} = 111.9 \cdot i_a + 1970 \quad , \quad (2.2)$$

which is the relation used in this project. All the system parameters used in the design are listed in Table 2.1. It is assumed that all frictions in the system can be modeled as a combination of Coulomb and viscous frictions. Wires hanging from the cart are unmodeled and their weight along with that of the belt are contained in the estimation of the cart mass.

Parameter	Notation	Quantity	Unit
Nominal current (max. continuous current)	$I_N$	4.58	A
Torque constant	$\tau_m$	$93.4 \times 10^{-3}$	$\text{N} \cdot \text{m} \cdot \text{A}^{-1}$
Pendulum Rod Length	$l$	0.3169	m
Rail Length	$l_r$	0.89	m
Pulley Radius	$r$	0.028	m
Pendulum Mass	$m$	0.2235	kg
Cart Mass	$M$	6.28	kg
Cart Coulomb Friction	$b_{c,c}$	$f(x, \dot{x})$	N
Cart Viscous Friction	$b_{c,v}$	0	$\text{N} \cdot \text{m}^{-1} \text{ s}$
Pendulum Coulomb Friction	$b_{p,c}$	$4.1 \times 10^{-3}$	$\text{N} \cdot \text{m}$
Pendulum Viscous Friction	$b_{p,v}$	$0.5 \times 10^{-3}$	$\text{N} \cdot \text{m} \cdot \text{s}$

**Table 2.1:** The motor parameters,  $I_N$  and  $\tau_m$ , are given by maxon in [2]. The rod length is measured from the pendulum pivot point to the geometrical center of the pendulum mass. Pulley radius, rail length, pendulum mass and rod length, are measured parameters, while cart mass is estimated same as all frictions. The cart Coulomb friction turns out to be a function of the cart position in addition to velocity. Details on parameter estimation are found in the implementation section at the end of *Part 1*.

## 2.2 Model

The model is based on the generalized coordinates presented in Figure 2.2.

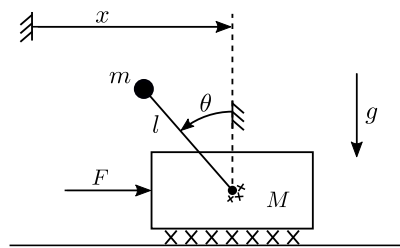


**Figure 2.2:** Mechanical drawing of the system, where  $\theta$  is the angle of the pendulum,  $x$  is the position of the center of the cart along the rail,  $F$  is the applied force and  $g$  is the gravitational acceleration. It is indicated that friction is modeled between cart and rail as well as in the pendulum joint.

The pendulum mass center is positioned at zero height at rest s.t. all energies in the system are positive. It is assumed that the pendulum rod is rigid and massless and that the pendulum weights are a point mass at the geometrical center of the weights.

The motor torque is given by direct relation to the armature current by the motor con-

stant,  $\tau_m = k_\tau i_a$ , such that,

$$F = \frac{1}{r} k_\tau i_a \quad . \quad (2.3)$$

To avoid excessive notation  $u = F$  is considered to be the control input in the remaining of this thesis, while keeping in mind the relation in Equation 2.3 along with the knowledge that  $u$  must be converted to armature current in implementation.

It is well known that the potential energy,  $U$ , and the kinetic energy,  $T$ , are given by, [10]

$$U = mgl(1 + \cos \theta) \quad (2.4)$$

$$T = \frac{1}{2}(M + m)\dot{x}^2 - m\dot{x}l \cos \theta \dot{\theta} + \frac{1}{2}ml^2\dot{\theta}^2 \quad . \quad (2.5)$$

The frictions, indicated in Figure 2.2, are, as mentioned, comprised of Coulomb and viscous frictions with values stated in Table 2.1. The viscous frictions are modeled as linear functions of velocities, [11, 12]

$$b_{p,v}\dot{\theta} \quad , \quad b_{c,v}\dot{x} \quad , \quad (2.6)$$

for the rotational and linear case respectively. The coulomb frictions are modeled as a constant with its sign depending on the signs of the velocities, such that, [11, 12]

$$\text{sgn}(\dot{\theta})b_{p,c} \quad , \quad \text{sgn}(\dot{x})b_{c,c} \quad . \quad (2.7)$$

This, however, introduces discontinuities at zero velocities. Thus, tanh-functions are used to obtain a continues approximation of the sign-functions,

$$\tanh(k_{\tanh}\dot{\theta})b_{p,c} \quad , \quad b_{c,v}\dot{x} - \tanh(k_{\tanh}\dot{x})b_{c,c} \quad , \quad (2.8)$$

where  $k_{\tanh} = 250$  to increase the steepness of the tanh-functions thereby obtaining a closer approximation of the sign-functions. Finally, by use of the Lagrange-d'Alembert Principle, [10]

$$\frac{d}{dt} \frac{\partial \mathcal{L}}{\partial \dot{\mathbf{q}}} - \frac{\partial \mathcal{L}}{\partial \mathbf{q}} = \mathbf{Q} \quad , \quad (2.9)$$

$$\mathbf{q} = \begin{bmatrix} \theta \\ x \end{bmatrix} \quad , \quad \mathbf{Q} = \begin{bmatrix} -b_{p,v}\dot{\theta} - \tanh(k_{\tanh}\dot{\theta})b_{p,c} \\ \frac{1}{r}k_\tau i_a - b_{c,v}\dot{x} - \tanh(k_{\tanh}\dot{x})b_{c,c} \end{bmatrix} \quad , \quad (2.10)$$

and  $\mathcal{L} = \mathcal{T} - \mathcal{U}$ , the dynamics of the system are found,

$$ml^2\ddot{\theta} - ml \cos \theta \ddot{x} - mgl \sin \theta = -b_{p,v}\dot{\theta} - \tanh(k_{\tanh}\dot{\theta})b_{p,c} \quad (2.11)$$

$$(M + m)\ddot{x} + ml \sin \theta \dot{\theta}^2 - ml \cos \theta \ddot{\theta} = u - b_{c,v}\dot{x} - \tanh(k_{\tanh}\dot{x})b_{c,c} \quad . \quad (2.12)$$

By setting up the dynamic equations, Equation 2.12 and 2.11, in the following manner,

$$\begin{aligned} & \begin{bmatrix} ml^2 & -ml \cos \theta \\ -ml \cos \theta & M + m \end{bmatrix} \begin{bmatrix} \ddot{\theta} \\ \ddot{x} \end{bmatrix} + \begin{bmatrix} 0 \\ ml \sin \theta \dot{\theta}^2 \end{bmatrix} + \\ & + \begin{bmatrix} b_{p,v} \dot{\theta} + \tanh(k_{\tanh} \dot{\theta}) b_{p,c} \\ b_{c,v} \dot{x} + \tanh(k_{\tanh} \dot{x}) b_{c,c} \end{bmatrix} + \begin{bmatrix} -mgl \sin \theta \\ 0 \end{bmatrix} = \begin{bmatrix} 0 \\ u \end{bmatrix} , \end{aligned} \quad (2.13)$$

the general form of an m-link robot is obtained, [13, 14]

$$\mathbf{M}(\mathbf{q})\ddot{\mathbf{q}} + \mathbf{C}(\mathbf{q}, \dot{\mathbf{q}}) + \mathbf{B}(\dot{\mathbf{q}}) + \mathbf{G}(\mathbf{q}) = \mathbf{F} , \quad (2.14)$$

where,

$\mathbf{M}(\mathbf{q})$  is the inertia matrix

$\mathbf{C}(\mathbf{q}, \dot{\mathbf{q}})$  is the Coriolis and centrifugal effects

$\mathbf{B}(\dot{\mathbf{q}})$  is the friction

$\mathbf{G}(\mathbf{q})$  is the force due to gravity

$\mathbf{F}$  is the input force vector .

Choosing  $[x_1 \ x_2 \ x_3 \ x_4]^T = [\theta \ x \ \dot{\theta} \ \dot{x}]^T$  as states results in the following nonlinear state space representation,

$$\begin{bmatrix} \dot{x}_1 \\ \dot{x}_2 \\ \dot{x}_3 \\ \dot{x}_4 \end{bmatrix} = \begin{bmatrix} x_3 \\ x_4 \\ \mathbf{M}^{-1}(x_1)(\mathbf{F} - \mathbf{C}(x_1, x_3) - \mathbf{B}(x_3, x_4) - \mathbf{G}(x_1)) \end{bmatrix} , \quad (2.15)$$

which is convenient when simulating the system. This representation is also used in the control designs.

### 3 | Swing-Up Design

In this chapter three swing-up controllers are designed, all based on [15]. The pendulum is started at rest,  $\theta = \pi$ , with the angle convention specified in Figure 2.2. The idea of the swing-up controller is to increase the mechanical energy in the system until it matches that of the desired end state,  $\theta = 0$  and  $\dot{\theta} = 0$ , that is, the upright position at rest. The minimum energy in the system occurs at the starting position at rest, which is considered to be zero as mentioned in the *Model* section 2.2. So the target energy is  $E_{\text{eq}} = 2mgl$ , that is, the potential energy of the pendulum in the unstable equilibrium.

Consider the pendulum dynamics from Equation 2.12, where  $J = ml^2$  is the pendulum inertia and frictions are assumed to be zero such that,

$$J\ddot{\theta} - ml \cos \theta a_c - mgl \sin \theta = 0 \quad . \quad (3.1)$$

This equation captures the behavior of the pendulum corresponding to some controlled acceleration  $a_c$  at the pivot point. This acceleration is viewed as the control input for now. The force needed to achieve this acceleration is considered at the end of the design. It is further convenient to describe the energy of the pendulum with the coordinate frame fixed at its pivot point, see Figure 3.1.

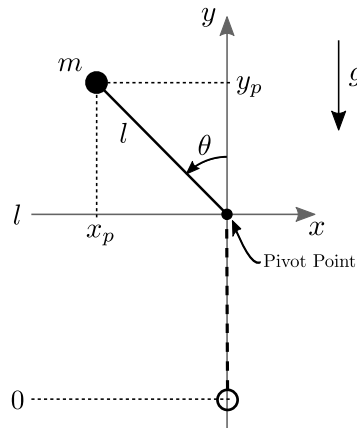


**Figure 3.1:** The energy used in the swing-up controller is described using this convention, where the coordinate frame is fixed at the pivot point of the pendulum. The zero reference is placed as before s.t. all energies are positive.

From Figure 3.1, the conversion from excessive to generalized coordinates is given by,

$$x_p = -l \sin \theta \quad , \quad y_p = l(\cos \theta + 1) \quad , \quad \dot{x}_p = -l \cos \theta \dot{\theta} \quad , \quad \dot{y}_p = -l \sin \theta \dot{\theta} \quad . \quad (3.2)$$

The mechanical energy in this coordinate frame is then,

$$E_p = mgy_p + \frac{1}{2}m\dot{x}_p^2 + \frac{1}{2}m\dot{y}_p^2 \quad (3.3)$$

$$E_p = mgl(\cos \theta + 1) + \frac{1}{2}m(-l \cos \theta \dot{\theta})^2 + \frac{1}{2}m(-l \sin \theta \dot{\theta})^2 \quad (3.4)$$

$$E_p = mgl(\cos \theta + 1) + \frac{1}{2}J(\cos^2 \theta + \sin^2 \theta)\dot{\theta}^2 \quad (3.5)$$

$$E_p = \frac{1}{2}J\dot{\theta}^2 + mgl(\cos \theta + 1) \quad . \quad (3.6)$$

The following sections explores different approaches of controlling the pendulum energy specified in Equation 3.6 to its desired reference.

### 3.1 Energy Control

A function candidate is proposed,

$$V(\theta, \dot{\theta}) = \frac{1}{2}E_{\Delta}^2 \quad , \quad (3.7)$$

where  $E_{\Delta}$  is the difference in energy in relation to the unstable equilibrium,

$$E_{\Delta} = E_p - E_{eq} \quad (3.8)$$

$$E_{\Delta} = \frac{1}{2}J\dot{\theta}^2 + mgl(\cos \theta + 1) - 2mgl \quad (3.9)$$

$$E_{\Delta} = \frac{1}{2}J\dot{\theta}^2 + mgl(\cos \theta - 1) \quad , \quad (3.10)$$

hence,

$$V = \frac{1}{2}(\frac{1}{2}J\dot{\theta}^2 + mgl(\cos \theta - 1))^2 \quad (3.11)$$

$$V = \frac{1}{2}(\frac{1}{2}J\dot{\theta}^2)^2 + \frac{1}{2}(mgl(\cos \theta - 1))^2 + \frac{1}{2}J\dot{\theta}^2 mgl(\cos \theta - 1) \quad (3.12)$$

$$V = \frac{1}{8}J^2\dot{\theta}^4 + \frac{1}{2}m^2g^2l^2(\cos^2 \theta + 1 - 2\cos \theta) + \frac{1}{2}J\dot{\theta}^2 mgl(\cos \theta - 1) \quad , \quad (3.13)$$

further,

$$\frac{\partial V}{\partial \theta} = -m^2g^2l^2 \cos \theta \sin \theta + m^2g^2l^2 \sin \theta - \frac{1}{2}J\dot{\theta}^2 mgl \sin \theta \quad (3.14)$$

$$\frac{\partial V}{\partial \dot{\theta}} = \frac{1}{2}J^2\dot{\theta}^3 + Jmgl(\cos \theta - 1)\dot{\theta} \quad , \quad (3.15)$$

where both Equation 3.14 and 3.15 are continuous,  $C^0$ , so  $V(\theta, \dot{\theta})$  is continuously differentiable,  $C^1$ , in the entire  $\mathbb{R}^2$ .

The idea is to reach the reference  $E_{\Delta} = 0$ , which happens when,

$$\frac{1}{2}J\dot{\theta}^2 + mgl(\cos \theta - 1) = 0 \quad (3.16)$$

$$\dot{\theta} = \pm \left( \frac{-2mgl(\cos \theta - 1)}{J} \right)^{\frac{1}{2}} \quad . \quad (3.17)$$

A plot of  $\dot{\theta}(\theta)$  from Equation 3.17 in the phase plane, see Figure 3.2, reveals a set of solutions joining the two unstable equilibrium points.

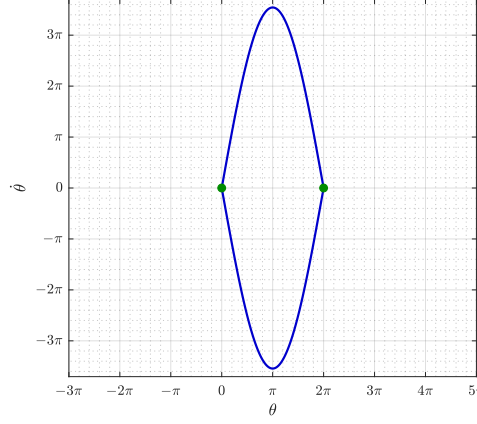


**Figure 3.2:** If the trajectories of the system are restricted to this set, the energy error is maintained at zero and the trajectories form a heteroclinic orbit.

If the energy reference is successfully tracked, the system will be restricted to this set rather than a single equilibrium point. Such a trajectory joining two equilibrium points is called a heteroclinic orbit.

Recall the system from Equation 3.1,

$$J\ddot{\theta} = ml \cos \theta a_c + mgl \sin \theta \quad , \quad (3.18)$$

the derivative of  $V$  is then evaluated along trajectories of the system,

$$\dot{V} = E_{\Delta} \dot{E}_{\Delta} \quad (3.19)$$

$$\dot{V} = E_{\Delta} (J\dot{\theta}\ddot{\theta} - mgl \sin \theta \dot{\theta}) \quad (3.20)$$

$$\dot{V} = E_{\Delta} (\dot{\theta} (ml \cos \theta a_c + mgl \sin \theta) - mgl \sin \theta \dot{\theta}) \quad (3.21)$$

$$\dot{V} = ml E_{\Delta} \cos \theta \dot{\theta} a_c \quad . \quad (3.22)$$

The idea is to find a control law,  $a_c$ , which allows trajectories of the system to reach the desired heteroclinic orbit. By studying LaSalle's Theorem 3.1.1, analysis of convergence to sets is made possible.

**Theorem 3.1.1 (LaSalle's Theorem)** *Consider the autonomous system,  $f(\mathbf{x}) = \dot{\mathbf{x}}$ , where  $f : \mathbb{D} \rightarrow \mathbb{R}^n$  is locally Lipschitz and  $\mathbf{x} = \mathbf{0}$  is an equilibrium point. Then if there exist some function  $V : \mathbb{D} \rightarrow \mathbb{R}$  and*

1.  $V(\mathbf{x})$  is  $C^1$
2.  $\exists c > 0$  s.t.  $\Omega_c = \{\mathbf{x} \in \mathbb{R}^n \mid V(\mathbf{x}) \leq c\} \subset \mathbb{D}$  is bounded
3.  $\dot{V}(\mathbf{x}) \leq 0 \quad \forall \mathbf{x} \in \Omega_c$

then  $\mathbf{x}(0) \in \Omega_c \Rightarrow \mathbf{x}(t) \xrightarrow{t \rightarrow \infty} M$ , where  $M$  is the largest invariant set in

$$E = \{\mathbf{x} \in \Omega_c \mid \dot{V}(\mathbf{x}) = 0\} \quad [16].$$

The first condition in LaSalle's Theorem 3.1.1 is already satisfied. Notice that the function candidate,  $V(\mathbf{x})$ , is not required to be positive definite.

The second condition states that some bounded set,  $\Omega_c$ , of solutions for which  $V(\mathbf{x})$  is less than or equal to some constant  $c$  must exist.

This ties into the third condition stating that the derivative of the function candidate must be negative semi-definite along trajectories of the system for all solutions in said set. The controlled acceleration at the pivot point,  $a_c$ , is then designed to satisfy the third condition in Theorem 3.1.1,

$$a_c = -kE_\Delta \cos \theta \dot{\theta} \quad , \quad (3.23)$$

where the tuning parameter,  $k > 0$ , is introduced to allow scaling the control output to fit the capabilities of the actuator. Inserting the control law yields,

$$\dot{V} = mlE_\Delta \cos \theta \dot{\theta} (-kE_\Delta \cos \theta \dot{\theta}) \quad (3.24)$$

$$\dot{V} = -kml(E_\Delta \cos \theta \dot{\theta})^2 \leq 0 \quad , \quad (3.25)$$

satisfying the third condition of Theorem 3.1.1 not only in  $\Omega_c$  but in the entire state space. This means any  $\infty > c > 0$  will satisfy the second condition. However, looking at the function candidate,

$$V = \frac{1}{8}J^2\dot{\theta}^4 + \frac{1}{2}m^2g^2l^2(\cos^2 \theta + 1 - 2\cos \theta) + \frac{1}{2}J\dot{\theta}^2mgl(\cos \theta - 1) \quad , \quad (3.26)$$

the angle is only present in periodic functions. Hence no value of  $c$  can bound the angle. If starting some arbitrary place in the state space, the energy reference is eventually tracked, but the heteroclinic orbit could settle between any two saddle points. To constrain further analysis and design to the desired region of operation,  $\Omega_c$  is defined as the set containing all points within and on the set in Figure 3.2, that is,

$$\Omega_c = \{\mathbf{x} \mid \dot{\theta} \leq \left( \frac{-2mgl(\cos \theta - 1)}{J} \right)^{\frac{1}{2}}, 0 \leq \theta \leq 2\pi\} \quad . \quad (3.27)$$

All conditions of LaSalle's Theorem 3.1.1 are satisfied, thus, if starting in  $\Omega_c$ , trajectories of the system will converge to  $M$  as time goes to infinity.  $M$  is the largest invariant set in  $E$ , which can be described as the union of sets for which Equation 3.25 is zero,

$$A = \{\mathbf{x} \in \Omega_c \mid E_\Delta = 0\} \quad (3.28)$$

$$B = \{\mathbf{x} \in \Omega_c \mid \cos \theta = 0\} \quad (3.29)$$

$$C = \{\mathbf{x} \in \Omega_c \mid \dot{\theta} = 0\} \quad (3.30)$$

$$E = A \cup B \cup C \quad . \quad (3.31)$$

To construct set  $M$  it is necessary to evaluate each set for invariance with respect to the controlled system. A proof is developed to show invariance of set  $A$ . Recall the relation between  $\dot{\theta}$  and  $\theta$  for  $E_\Delta = 0$  ,

$$\dot{\theta}_z = \pm \left( \frac{-2mgl(\cos \theta - 1)}{J} \right)^{\frac{1}{2}} \quad , \quad (3.32)$$

where  $\dot{\theta}_z$  is the angular velocity for which the energy error is zero. Further, consider the controlled system in following form,

$$\ddot{\theta} = \frac{1}{J}(-kml \cos \theta E_{\Delta} \cos \theta \dot{\theta} + mgl \sin \theta) \quad . \quad (3.33)$$

To prove that  $A$  is invariant with respect to Equation 3.33, the slope of  $\dot{\theta}_z$  is compared to the slope of the controlled system trajectories in the set. If the slopes are equal, then no trajectory can leave the set  $A$ , thus proving  $A$  is invariant with respect to the controlled system. The slope of  $\dot{\theta}_z$  is,

$$\frac{\partial \dot{\theta}_z}{\partial \theta} = \pm \frac{mgl \sin \theta}{J} \left( \frac{-2mgl(\cos \theta - 1)}{J} \right)^{-\frac{1}{2}} \quad (3.34)$$

$$\frac{\partial \dot{\theta}_z}{\partial \theta} = \frac{mgl \sin \theta}{J \dot{\theta}_z} \quad . \quad (3.35)$$

The slope of the trajectories of the controlled system, Equation 3.33, in set  $A$  is then,

$$b = \frac{\ddot{\theta}_z}{\dot{\theta}_z} \quad (3.36)$$

$$b = \frac{-kml \cos^2 \theta E_{\Delta}(\theta, \dot{\theta}_z) \dot{\theta}_z + mgl \sin \theta}{J \dot{\theta}_z} \quad (3.37)$$

$$b = \frac{-kml \cos^2 \theta (\frac{1}{2} J \dot{\theta}_z^2 + mgl(\cos \theta - 1)) \dot{\theta}_z}{J \dot{\theta}_z} + \frac{mgl \sin \theta}{J \dot{\theta}_z} \quad (3.38)$$

$$b = -kml \cos^2 \theta \frac{1}{2} \dot{\theta}_z^2 - \frac{1}{J} kml \cos^2 \theta mgl(\cos \theta - 1) + \frac{mgl \sin \theta}{J \dot{\theta}_z} \quad (3.39)$$

$$b = -kml \cos^2 \theta \frac{1}{2} \left( \frac{-2mgl(\cos \theta - 1)}{J} \right) - \frac{1}{l^2 m} km^2 l^2 g \cos^2 \theta (\cos \theta - 1) + \frac{mgl \sin \theta}{J \dot{\theta}_z} \quad (3.40)$$

$$b = -kml \cos^2 \theta \frac{1}{2} \frac{-2mgl(\cos \theta - 1)}{l^2 m} - k \cos^2 \theta mg(\cos \theta - 1) + \frac{mgl \sin \theta}{J \dot{\theta}_z} \quad (3.41)$$

$$b = k \cos^2 \theta mg(\cos \theta - 1) - k \cos^2 \theta mg(\cos \theta - 1) + \frac{mgl \sin \theta}{J \dot{\theta}_z} \quad (3.42)$$

$$b = \frac{mgl \sin \theta}{J \dot{\theta}_z} \quad , \quad (3.43)$$

where  $\ddot{\theta}_z$  is the angular acceleration of the controlled system in set  $A$ . Finally, since,

$$\frac{\partial \dot{\theta}_z}{\partial \theta} = b \quad , \quad (3.44)$$

the set  $A$  is invariant with respect to the controlled system. The set  $B$  is invariant only for the intersection  $B \cap A$ , any other values of the angular velocity will cause it to leave the set since  $\cos \theta = 0$  corresponds to a horizontal position of the pendulum. A similar

argument can be made for set  $C$ , however, in this case if  $\theta = \pi$ , the system stays in the set. So, the invariant part of set  $C$  excluding  $A$  is,

$$F = \{\mathbf{x} \in \Omega_c \mid \dot{\theta} = 0, \theta = \pi\} \quad , \quad (3.45)$$

thus the largest invariant set in  $E$  is,

$$M = A \cup F \quad . \quad (3.46)$$

The sets are visualized in Figure 3.3.

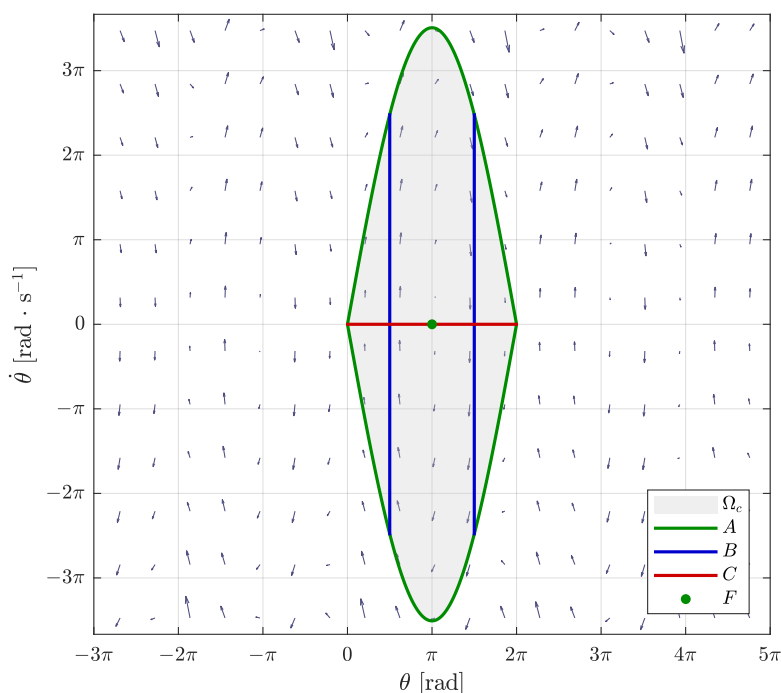


**Figure 3.3:** The set  $\Omega_c$  shown along with sets in  $\Omega_c$  for which  $\dot{V}(\mathbf{x}) = 0$ . Set  $A$  and  $F$  together form the largest invariant set  $M$  in  $E$ . The phase portrait of the controlled system shows how its trajectories line up with  $A$  indicating invariance of  $A$  with respect to the controlled system.

If this control law is started at zero angular velocity,  $\dot{\theta} = 0$ , in the stable equilibrium, the computed control is maintained at zero and the pendulum never swings up. So for this control law to work, the pendulum must be started slightly away from the stable equilibrium.

An extra step is needed to apply this control strategy. So far the control output is an acceleration,  $a_c$ , at the pivot point. It is possible to input the desired acceleration,  $a_c$ , into the second dynamic equation, Equation 2.12, and solve for the force needed to achieve this acceleration,

$$u = (M + m)a_c + ml \sin x_1 x_3^2 - ml \cos x_1 \dot{x}_3 \quad , \quad (3.47)$$

where the cart friction coefficients are set to zero again.

To calculate the force from this expression, Equation 3.47, it is also necessary to know the angular acceleration of the pendulum,  $\dot{x}_3$ , which can be solved for in the system dynamics, Equation 2.15, inserting known states and control input applied in the previous step,

$$\begin{bmatrix} \dot{x}_3 \\ \dot{x}_4 \end{bmatrix} = \begin{bmatrix} ml^2 & -ml \cos x_1 \\ -ml \cos x_1 & M + m \end{bmatrix}^{-1} \begin{bmatrix} -b_{p,v}x_3 - \tanh(k_{\tanh}x_3)b_{p,c} + mgl \sin x_1 \\ u_{last} - ml \sin x_1 x_3^2 \end{bmatrix}, \quad (3.48)$$

where  $u_{last}$  is the force applied in the previous step.

From Equation 3.48 the approximated angular acceleration is then,

$$\dot{x}_3 = \frac{(M + m)(-b_{p,v}x_3 - \tanh(k_{\tanh}x_3)b_{p,c} + mgl \sin x_1)}{l^2m(M + m - m \cos^2 x_1)} + \frac{\cos x_1(u_{last} - ml \sin x_1 x_3^2)}{l(M + m - m \cos^2 x_1)}. \quad (3.49)$$

Inserting Equation 3.49 into Equation 3.47 results in the control input,  $u$ , necessary to achieve the desired acceleration,  $a_c$ , at the pivot point. This method is used for all three swing-up controllers, so to avoid excessive notation the proceeding energy control laws are derived with  $a_c$  as the control parameter.

All simulations are performed using the nonlinear state space representation in Equation 2.15 and the matlab ODE45 solver with a relative tolerance of  $1 \times 10^{-7}$ . Initializing the angle,  $\theta$ , at  $\pi - 0.1$  to avoid zero control output as discussed, the energy difference struggles to reach its reference at zero, see Figure 3.4. The pendulum friction and cart inertia are included in the calculation of the force needed to obtain the desired acceleration. This, however, is not concerned with what is needed to obtain the required energy. So the offset seen in Figure 3.4 is caused by the control law, Equation 3.23, asking for insufficient acceleration.

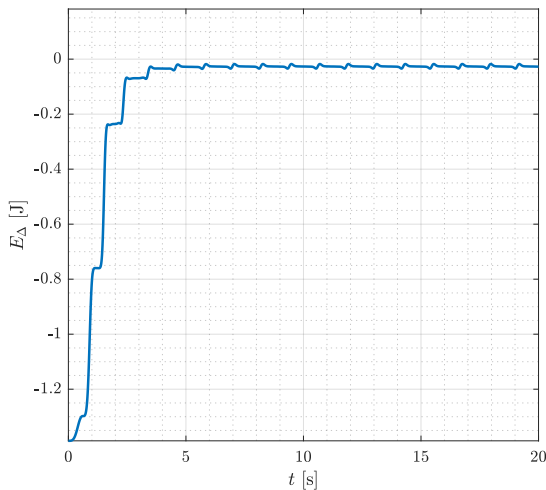


**Figure 3.4:** Simulation of the first energy control method. The energy error struggles to maintain zero value, due to pendulum friction and cart inertia exchanging energy with the pendulum.

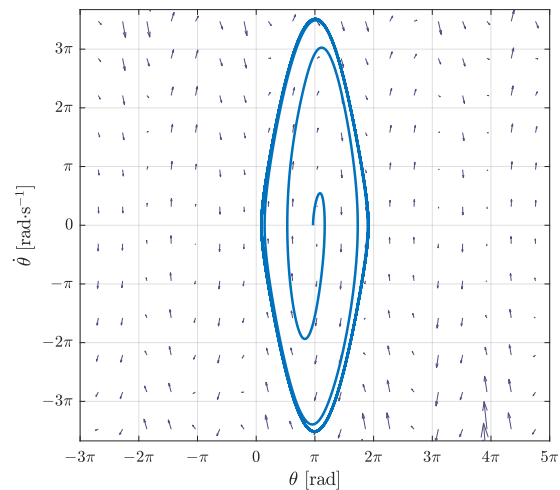


**Figure 3.5:** This phase portrait shows the attempt to reach the heteroclinic orbit. It falls short due to the insufficient acceleration asked by the control law.

The pendulum also falls short of reaching the heteroclinic orbit, see Figure 3.5. Further, since the energy of the pendulum is not affected by the position or velocity of the cart, this control law, Equation 3.23, is not concerned with controlling these. This becomes a problem in the physical setup as it has a rail length of 0.89 m, see Table 2.1. A traced animation is used to demonstrate this problem in Figure 3.6.

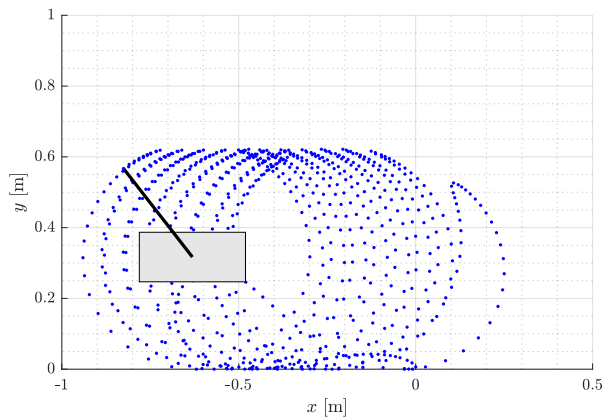


**Figure 3.6:** The cart drifts beyond the bounds of the physical system. This might not be a problem if the catch controller catches the pendulum in first try, but there is no guarantee of this being the case.

An other issue is the actuation which is limited in the real system by the maximum allowed continuous current, see Table 2.1. By tuning the parameter  $k$  in the control law, better performance can be obtained, however at the cost of excessive actuation.

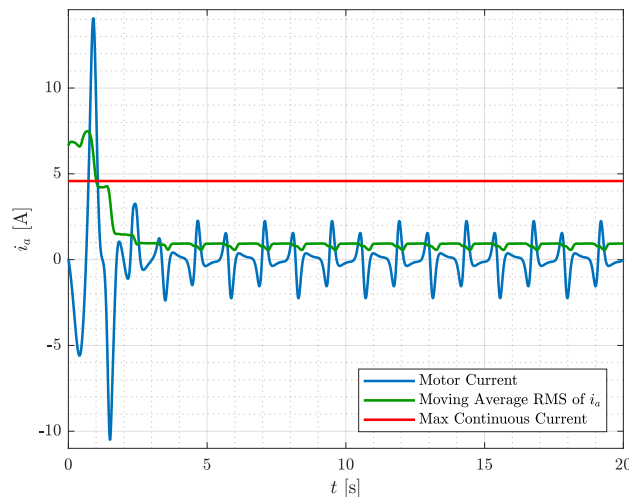


**Figure 3.7:** The motor current has high peaks in the beginning which likely exceeds the capabilities of the motor. The controller is tuned such that the RMS value of the current does not exceed the maximum continuous current requirement of the motor for a sustained period of time.

For these graphs  $k = 1.3$  to keep the motor current at acceptable levels. The motor current is shown in Figure 3.7 where the rolling RMS of  $i_a$  is used to approximate the continuous current load on the motor. Though the continuous current is acceptable, the

peaks in the start will be saturated in the real system, which would cause a longer rise time for the energy.

## 3.2 Sign-Based Energy Control

There are other ways to satisfy Equation 3.25 than the control law suggested in Equation 3.23. To achieve maximal actuation a sign-function can be used to determine the direction of actuation along with a gain  $k$  to adjust for the limits of the actuator as before,

$$a_c = k \operatorname{sgn}(-E_\Delta \cos \theta \dot{\theta}) \quad , \quad (3.50)$$

where,

$$\operatorname{sgn}(s(\theta, \dot{\theta})) = \begin{cases} 1 & s > 0 \vee \cos \theta \dot{\theta} = 0 \\ 0 & s = 0 \wedge \cos \theta \dot{\theta} \neq 0 \\ -1 & s < 0 \end{cases} \quad , \quad (3.51)$$

to avoid no actuation when starting at stable equilibrium. This adjustment reduces the set,

$$M = \{\mathbf{x} \in \Omega_c \mid E_\Delta = 0\} \quad , \quad (3.52)$$

such that convergence to  $M$  when starting in  $\Omega_c$ , by Theorem 3.1.1, now assures convergence to the energy reference and thus to the heteroclinic orbit.

The gain is tuned to  $k = 2.4$  in the following simulation. Looking at the energy in Figure 3.8, this strategy seems to work really well. From the phase portrait in Figure 3.9 it is evident that a near perfect heteroclinic orbit is reached.

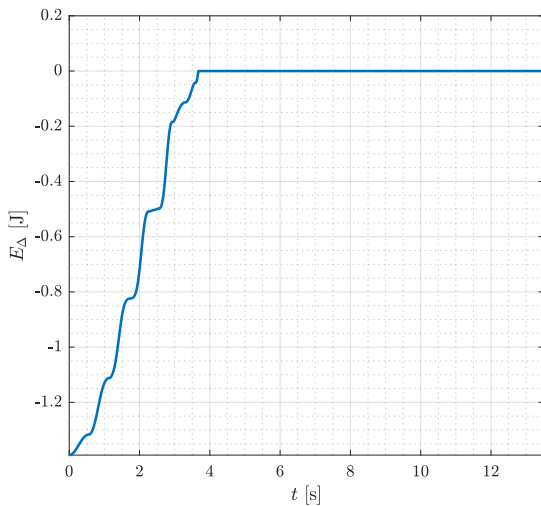


**Figure 3.8:** Using maximum actuation in the appropriate direction drives the energy error to zero and keeps it there.

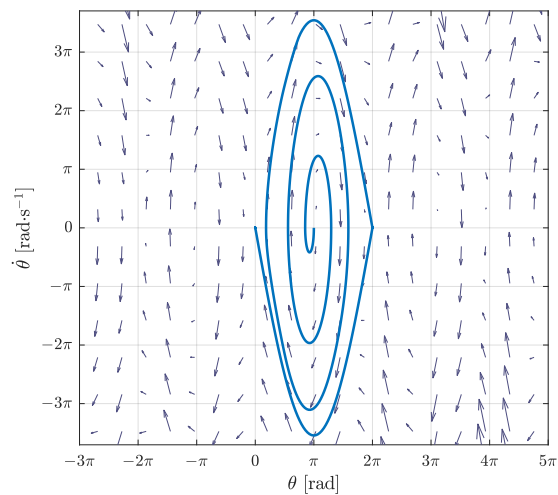


**Figure 3.9:** The heteroclinic orbit is reached very accurately.

In Figure 3.10 however, while the angle reaches the equilibrium as closely as possible without overshooting, this control law, as with the previous, does not account for position of the cart.

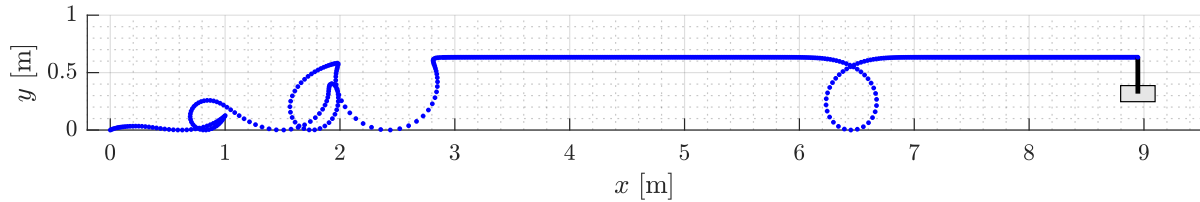


**Figure 3.10:** The cart drifts as before, since the controller is only concerned with the energy of the pendulum.

However, the bigger problem with this control law is obvious from Figure 3.11, where excessive switching shows on the control output.

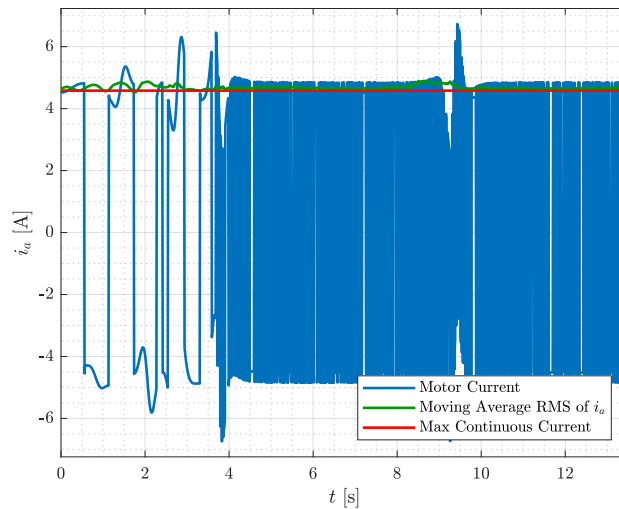


**Figure 3.11:** The sign-function in the control law causes excessive switching in the output, thus, the design is not feasible for a real system implementation.

This actuation behavior is not feasible in a real system and attempted implementation will cause chattering resulting in unwanted behavior and wear of the motor. In next section it is attempted to solve this issue, while keeping some of the performance of this approach.

### 3.3 Sat-Based Energy Control

To avoid the excessive switching of the sign-based controller a different strategy using a saturation function is investigated,

$$a_c = \text{sat}(-kE_{\Delta} \text{sgn}(\cos \theta \dot{\theta})) \quad , \quad (3.53)$$

where

$$\text{sgn}(s) = \begin{cases} 1 & s \geq 0 \\ -1 & s < 0 \end{cases}, \quad (3.54)$$

and the sat-function saturates at the minimum/maximum allowed acceleration. The known limitation is  $i_{max} = 4.58 \text{ A}$  as stated in Table 2.1, from which the maximum control,  $u$ , can be calculated,

$$u_{max} = \frac{k_{\tau}}{r}, \quad (3.55)$$

and finally, by disregarding the pendulum behavior and cart friction from the dynamics in Equation 2.12,

$$a_{max} = \frac{u_{max}}{M + m}. \quad (3.56)$$

As this is a crude estimate  $0.1 \text{ m} \cdot \text{s}^{-2}$  is subtracted from the estimated  $a_{max}$  in following simulations to stay within the actuation limits. The saturation function is then,

$$\text{sat}(s) = \begin{cases} s & |s| \leq a_{max} \\ \text{sgn}(s) a_{max} & |s| > a_{max} \end{cases}. \quad (3.57)$$

Notice how the sgn-function in this control law, Equation 3.53, only takes  $\cos \theta \dot{\theta}$  as input. Contrary to the sign-based controller which also included  $E_{\Delta}$  causing the need for complicated restrictions in the definition of the sgn-function.

Choice of  $k$  decides how aggressive the controller should be. Larger values of  $k$  drives the control into saturation faster thus actuating more like the sign-based controller in Equation 3.50. At lower values of  $k$  the operation will not reach saturation as fast thus behaving more like the first energy based controller in Equation 3.23. For an effective swing up behavior  $k = 200$  is chosen, thus approaching the behavior of the sign-based controller, which makes sense as this is the theoretically ideal solution.

This control strategy achieves the energy reference in about three seconds, Figure 3.12, as is the case of the sign-based strategy, Figure 3.8. Further, from Figure 3.13, the system still reaches a near perfect heteroclinic orbit.

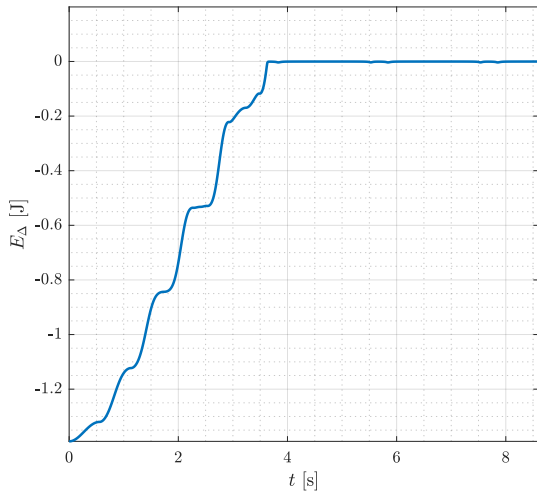


**Figure 3.12:** The sat-based controller shows no loss in performance when comparing the energy error to that of the sign-based approach.

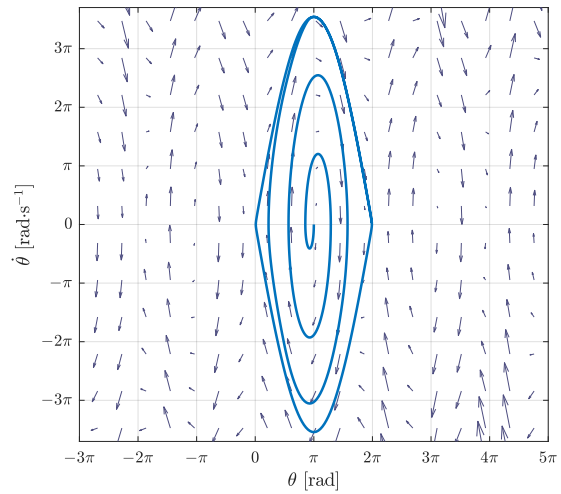


**Figure 3.13:** The heteroclinic orbit is still reached, however, with a more realistic trajectory at the approach of the equilibrium points.

The cart still drifts as expected, see Figure 3.14, and the equilibrium points are maintained for shorter duration, which is expected with less control switching. Figure 3.14.

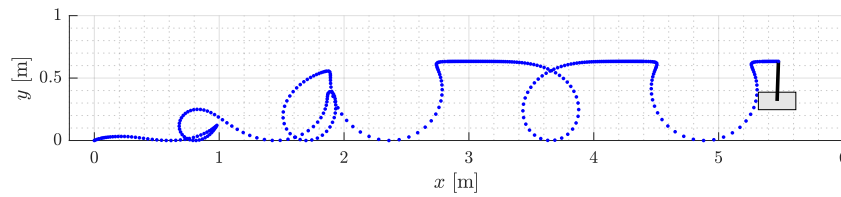


**Figure 3.14:** This strategy performs well. The drifting problem is solved later.

The excessive switching on the control output is successfully avoided, see Figure 3.15, resulting in a much more realistic control signal compared to that in Figure 3.11.

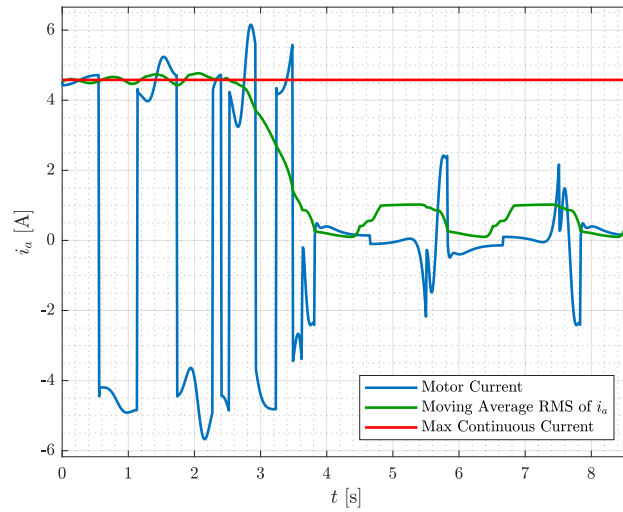


**Figure 3.15:** The control signal using the sat-based approach is much more realistic for implementation as the excessive switching of the sign-based controller is successfully avoided.

The design of the energy based control law, Equation 3.53, is concluded. The problem of controlling the cart position still remains. In the following, the performance of this control law is subjected to the disturbance caused by added control on the cart position and velocity.

### 3.4 Cart Position and Velocity Control

To solve the cart drifting problem along  $x$  a linear controller is designed and added to the control law,

$$a_c = \psi(x_1, x_3) + v(x_2, x_4) \quad , \quad (3.58)$$

where  $\psi(x_1, x_3)$  is the energy controller and  $v(x_2, x_4)$  is the linear controller. While these two controllers depend on different states, they still influence and act as unmodeled disturbances to one another. The position and velocity control,  $v(x_2, x_4)$ , adds and subtracts energy, therefore could cause the energy controller,  $\psi(x_1, x_3)$ , to overshoot. One solution to this potential problem could be to slightly lower the energy reference. However, swing-up is often designed with a higher energy reference such that the catch controller has some entry velocity at the unstable equilibrium.

With these considerations in mind, the design of  $v(x_2, x_4)$  is proceeded. Considering the cart without friction and assuming any influence of the pendulum dynamics and the energy control to be unmodeled disturbances of the system. This reduces the model to the mechanical drawing seen in Figure 3.16.

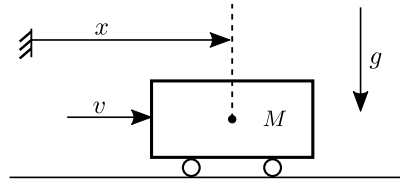


**Figure 3.16:** Mechanical drawing of the reduced model used for position control.

The dynamics are then,

$$M\ddot{x} = v \quad , \quad (3.59)$$

and selecting new states  $[z_1 \ z_2]^T = [x \ \dot{x}]^T$ , the linear state space is,

$$\begin{bmatrix} \dot{z}_1 \\ \dot{z}_2 \end{bmatrix} = \underbrace{\begin{bmatrix} 0 & 1 \\ 0 & 0 \end{bmatrix}}_{\mathbf{A}} \begin{bmatrix} z_1 \\ z_2 \end{bmatrix} + \underbrace{\begin{bmatrix} 0 \\ \frac{1}{M} \end{bmatrix}}_{\mathbf{B}} v \quad . \quad (3.60)$$

The closed loop poles are placed in  $p = [-1 \ -2]$  using matlab *place()*-command to obtain linear feedback gains,  $\mathbf{k}_1 = [10.5460 \ 15.8190]$ , resulting in the controller,

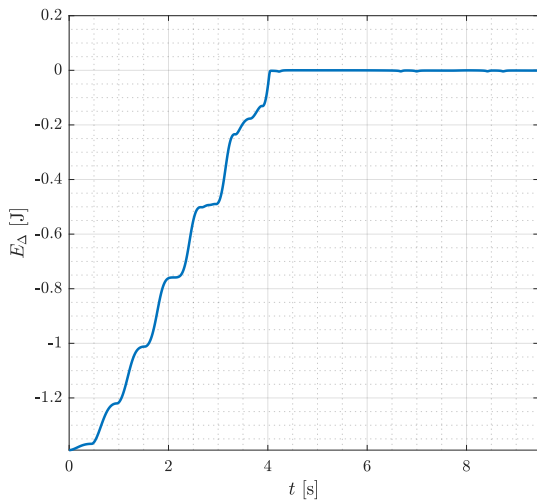
$$v = -\mathbf{k}_1 \mathbf{z} \quad , \quad (3.61)$$

where  $\mathbf{z} = [x \ \dot{x}]^T$ , such that,

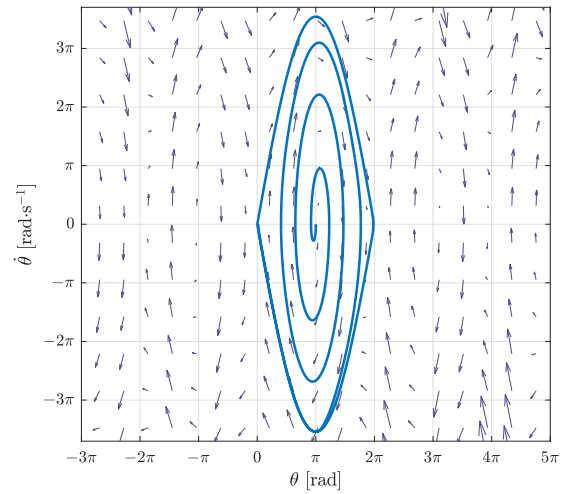
$$v(x_2, x_4) = -\mathbf{k}_1 [x_2 \ x_4]^T \quad , \quad (3.62)$$

in terms of the full system. This control is added to the sat-based design and simulations are run without changing any previously designed gains.

Figure 3.17 shows the energy error reaching zero, taking one second longer under the influence of the linear controller, compared to Figure 3.12.

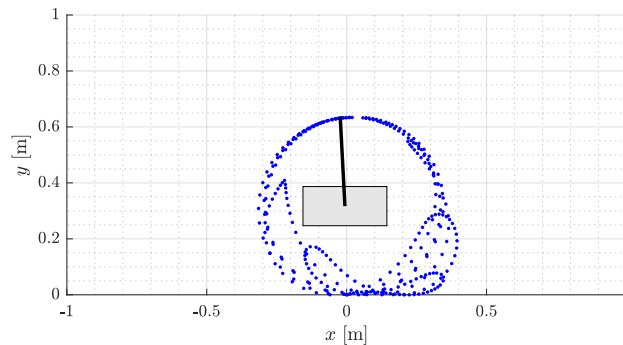


**Figure 3.17:** The sat-based controller reaches the reference in about four seconds, compared to three seconds it took without position and velocity control.



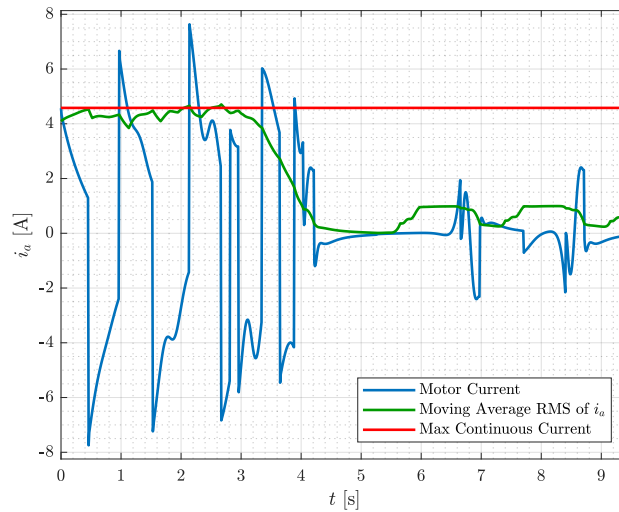
**Figure 3.18:** Though the sat-based energy controller reaches its reference one second slower when kept around  $x = 0$ , it still reaches the heteroclinic orbit with no overshoot.

In the phase portrait, see Figure 3.18, it is clear that the sat-based controller still reaches the heteroclinic orbit. Figure 3.19 shows how the linear control of the cart position and velocity successfully keeps the system within the available operating region of the real system.



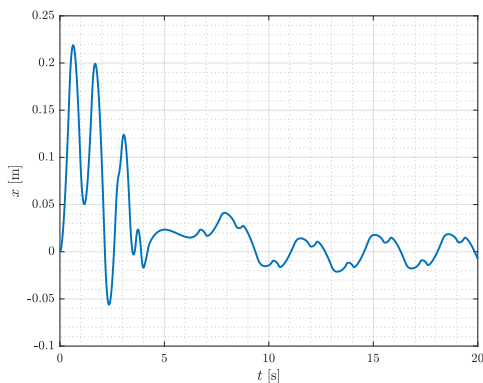
**Figure 3.19:** The linear control successfully keeps the cart around zero while the energy control approaches the unstable equilibrium.

Figure 3.20 shows the actuation required, the RMS is slightly lower than it was before the linear controller was added.



**Figure 3.20:** The control signal causes less continuous current but higher peaks compared to the same swing-up without control on the cart position.

Figure 3.21 show the position approaching zero as the energy control settles, which is ideal, as it means the energy controller still has room to operate without fighting the linear feedback controller too much. Similarly, the oscillations around zero are necessary for the energy controller to keep its reference. Further, as seen in Figure 3.22 the velocity of the cart is also eventually controlled to zero by the added liner controller.



**Figure 3.21:** The saturation based controller keeps the cart closer to zero, suggesting less actuation from the energy control.

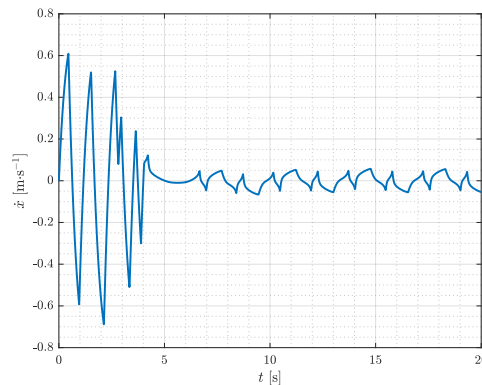


**Figure 3.22:** Zero velocity is obtained quite effectively after the energy reference is reached.

These two graphs are simulated over longer time to show that the linear controller reaches its reference.

This concludes the design of swing-up control.

## 4 | Stabilization

In this section the idea is to stabilize the pendulum in the unstable equilibrium. Ultimately this controller should be able to take over from the swing-up controller when some minimum catch angle is reached.

A sliding mode control strategy is employed to accomplish these goals. The design is based on [16].

Firstly, the model of the system, from Equation 2.15, is considered in following form,

$$\begin{bmatrix} \dot{x}_1 \\ \dot{x}_2 \\ \dot{x}_3 \\ \dot{x}_4 \end{bmatrix} = \underbrace{\begin{bmatrix} x_3 \\ x_4 \\ \mathbf{M}^{-1}(x_1)(-\mathbf{C}(x_1, x_3) - \mathbf{B}(x_3, x_4) - \mathbf{G}(x_1)) \end{bmatrix}}_{\mathbf{f}(\mathbf{x})} + \underbrace{\begin{bmatrix} 0 \\ 0 \\ \mathbf{M}^{-1}(x_1)\mathbf{F} \end{bmatrix}}_{\mathbf{g}(\mathbf{x})u}, \quad (4.1)$$

where,

$$\mathbf{M}^{-1} = \begin{bmatrix} \frac{(M+m)}{l^2 m(M+m-m \cos^2 x_1)} & \frac{\cos x_1}{l(M+m-m \cos^2 x_1)} \\ \frac{\cos x_1}{l(M+m-m \cos^2 x_1)} & \frac{1}{M+m-m \cos^2 x_1} \end{bmatrix}, \quad (4.2)$$

with states  $[x_1 \ x_2 \ x_3 \ x_4]^T = [\theta \ x \ \dot{\theta} \ \dot{x}]^T$  and input vector  $\mathbf{F} = [0 \ u]^T$  as before.

In Equation 4.1 the input,  $u$ , appear in two of the four state equations. To design a sliding mode controller for the system, it is transformed into *regular form*,

$$\begin{aligned} \dot{\boldsymbol{\eta}} &= \mathbf{f}_a(\boldsymbol{\eta}, \xi) \\ \dot{\xi} &= f_b(\boldsymbol{\eta}, \xi) + g_b(\boldsymbol{\eta}, \xi)u, \end{aligned} \quad (4.3)$$

where the input only appears on one state equation. The transform is then given by,

$$\mathbf{T}(\mathbf{x}) = \begin{bmatrix} \boldsymbol{\eta} \\ \xi \end{bmatrix} \Rightarrow \frac{\partial}{\partial t} \mathbf{T}(\mathbf{x}) = \begin{bmatrix} \dot{\boldsymbol{\eta}} \\ \dot{\xi} \end{bmatrix} \Rightarrow \frac{\partial}{\partial t} \mathbf{T}(\mathbf{x}) = \begin{bmatrix} \mathbf{f}_a(\boldsymbol{\eta}, \xi) \\ f_b(\boldsymbol{\eta}, \xi) + g_b(\boldsymbol{\eta}, \xi)u \end{bmatrix}, \quad (4.4)$$

further,

$$\frac{\partial \mathbf{T}}{\partial t} = \frac{\partial \mathbf{T}}{\partial \mathbf{x}} \dot{\mathbf{x}} \quad (4.5)$$

$$\begin{bmatrix} \mathbf{f}_a(\boldsymbol{\eta}, \xi) \\ f_b(\boldsymbol{\eta}, \xi) + g_b(\boldsymbol{\eta}, \xi)u \end{bmatrix} = \frac{\partial \mathbf{T}}{\partial \mathbf{x}} \mathbf{f}(\mathbf{x}) + \frac{\partial \mathbf{T}}{\partial \mathbf{x}} \mathbf{g}(\mathbf{x})u, \quad (4.6)$$

such that,

$$\frac{\partial \mathbf{T}}{\partial \mathbf{x}} \mathbf{f}(\mathbf{x}) = \begin{bmatrix} \mathbf{f}_a(\boldsymbol{\eta}, \xi) \\ f_b(\boldsymbol{\eta}, \xi) \end{bmatrix}, \quad \frac{\partial \mathbf{T}}{\partial \mathbf{x}} \mathbf{g}(\mathbf{x}) = \begin{bmatrix} \mathbf{0} \\ g_b(\boldsymbol{\eta}, \xi) \end{bmatrix}. \quad (4.7)$$

Equation 4.7 results in the following four equations,

$$\begin{aligned} \frac{\partial \eta_1}{\partial x_3} g_3 + \frac{\partial \eta_1}{\partial x_4} g_4 &= 0, & \frac{\partial \eta_2}{\partial x_3} g_3 + \frac{\partial \eta_2}{\partial x_4} g_4 &= 0 \\ \frac{\partial \eta_3}{\partial x_3} g_3 + \frac{\partial \eta_3}{\partial x_4} g_4 &= 0, & \frac{\partial \xi}{\partial x_3} g_3 + \frac{\partial \xi}{\partial x_4} g_4 &= g_b(\boldsymbol{\eta}, \xi), \end{aligned} \quad (4.8)$$

where,

$$\begin{bmatrix} g_3 \\ g_4 \end{bmatrix} u = \mathbf{M}^{-1}(x_1) \begin{bmatrix} 0 \\ u \end{bmatrix} \Rightarrow \begin{cases} g_3 = \frac{\cos x_1}{l(M+m-m \cos^2 x_1)} \\ g_4 = \frac{1}{M+m-m \cos^2 x_1} \end{cases}. \quad (4.9)$$

The following choice of coordinates to satisfy Equation 4.8 without loss of rank in  $\mathbf{T}$ , is based on the transform used for input-output linearization in [16].

Choosing output,  $h(x) = \theta$  or  $h(x) = x$ , both results in the relative degree,  $\rho = 2$ , since the output appears on the second derivatives,

$$\ddot{\theta} = \dot{x}_3 = f_3 + g_3 u \quad (4.10)$$

$$\ddot{x} = \dot{x}_4 = f_4 + g_4 u. \quad (4.11)$$

The suggested transform is then,

$$\mathbf{T}(\mathbf{x}) = \begin{bmatrix} \phi_1(\mathbf{x}) \\ \vdots \\ \phi_{n-\rho}(\mathbf{x}) \\ h(\mathbf{x}) \\ L_f h(\mathbf{x}) \\ \vdots \\ L_f^{\rho-1} h(\mathbf{x}) \end{bmatrix} \Rightarrow \begin{bmatrix} \eta_1 \\ \eta_2 \\ \eta_3 \\ \xi \end{bmatrix} = \begin{bmatrix} \phi_1(\mathbf{x}) \\ \phi_2(\mathbf{x}) \\ h(\mathbf{x}) \\ L_f h(\mathbf{x}) \end{bmatrix}, \quad (4.12)$$

where  $L_f h(\mathbf{x})$  is the *Lie derivative* of  $h(\mathbf{x})$  along  $f(\mathbf{x})$ . This results in two possible transforms,

$$h = \theta \Rightarrow \mathbf{T}_1 = \begin{bmatrix} \eta_1 \\ \eta_2 \\ \eta_3 \\ \xi \end{bmatrix} = \begin{bmatrix} \phi_1 \\ \phi_2 \\ x_1 \\ x_3 \end{bmatrix} \quad \text{and} \quad h = x \Rightarrow \mathbf{T}_2 = \begin{bmatrix} \eta_1 \\ \eta_2 \\ \eta_3 \\ \xi \end{bmatrix} = \begin{bmatrix} \phi_1 \\ \phi_2 \\ x_2 \\ x_4 \end{bmatrix}, \quad (4.13)$$

leaving  $\phi_1$  and  $\phi_2$  to be determined. This is done by satisfying,

$$\frac{\partial \eta_1}{\partial x_3} g_3 + \frac{\partial \eta_1}{\partial x_4} g_4 = 0 \quad (4.14)$$

$$\frac{\partial \eta_2}{\partial x_3} g_3 + \frac{\partial \eta_2}{\partial x_4} g_4 = 0 \quad , \quad (4.15)$$

from Equation 4.8. For  $\mathbf{T}_1$  the choice  $\phi_1 = x_2$  satisfies Equation 4.14 with no loss of rank in the transform. Conversely for  $\mathbf{T}_2$  the choice  $\phi_1 = x_1$  satisfies Equation 4.14 again with no loss of rank. This leaves  $\phi_2$  which, for both transforms, is determined by finding a solution to Equation 4.15,

$$\frac{\partial \eta_2}{\partial x_3} \frac{\cos x_1}{l(M + m - m \cos^2 x_1)} + \frac{\partial \eta_2}{\partial x_4} \frac{1}{M + m - m \cos^2 x_1} = 0 \quad , \quad (4.16)$$

choosing,

$$\frac{\partial \eta_2}{\partial x_4} = \frac{\cos x_1}{l} \quad , \quad \frac{\partial \eta_2}{\partial x_3} = -1 \quad , \quad (4.17)$$

such that,

$$\eta_2 = \frac{\cos x_1}{l} x_4 - x_3 \quad . \quad (4.18)$$

This results in the following two transform candidates,

$$\mathbf{T}_1 = \begin{bmatrix} x_2 \\ \frac{\cos x_1}{l} x_4 - x_3 \\ x_1 \\ x_3 \end{bmatrix} \quad , \quad \mathbf{T}_2 = \begin{bmatrix} x_1 \\ \frac{\cos x_1}{l} x_4 - x_3 \\ x_2 \\ x_4 \end{bmatrix} \quad . \quad (4.19)$$

It is desired for the transform,  $\mathbf{T}$ , to be continuously differentiable and have a continuously differentiable inverse,  $\mathbf{T}^{-1}$ . Such a transform is known as a diffeomorphism. Further,  $\mathbf{T}$  is a global diffeomorphism iff its Jacobian is nonsingular for all  $\mathbf{x} \in \mathbb{R}^n$  and  $\lim_{\|\mathbf{x}\| \rightarrow \infty} \|\mathbf{T}(\mathbf{x})\| = \infty$ , [16].

Thus the Jacobian of each transform is computed,

$$\mathbf{J}_1 = \frac{\partial \mathbf{T}_1(\mathbf{x})}{\partial \mathbf{x}} = \begin{bmatrix} 0 & 1 & 0 & 0 \\ -\frac{\sin x_1}{l} x_4 & 0 & -1 & \frac{\cos x_1}{l} \\ 1 & 0 & 0 & 0 \\ 0 & 0 & 1 & 0 \end{bmatrix} \quad (4.20)$$

$$\mathbf{J}_2 = \frac{\partial \mathbf{T}_2(\mathbf{x})}{\partial \mathbf{x}} = \begin{bmatrix} 1 & 0 & 0 & 0 \\ -\frac{\sin x_1}{l} x_4 & 0 & -1 & \frac{\cos x_1}{l} \\ 0 & 1 & 0 & 0 \\ 0 & 0 & 0 & 1 \end{bmatrix} \quad . \quad (4.21)$$

To check for singularity the determinant is found for the two Jacobian matrices,

$$\det(\mathbf{J}_1) = -\frac{\cos x_1}{l} \quad , \quad \det(\mathbf{J}_2) = 1 \quad . \quad (4.22)$$

If  $\cos x_1 = 0$  the Jacobian,  $\mathbf{J}_1$ , becomes singular. This only happens when the pendulum is in a horizontal position, which is outside the operating range of a stabilizing controller. However, the Jacobian,  $\mathbf{J}_2$ , is nonsingular for all  $\mathbf{x} \in \mathbb{R}^4$ . Further,  $\lim_{\|\mathbf{x}\| \rightarrow \infty} \|\mathbf{T}_2(\mathbf{x})\| = \infty$  so,

$$\mathbf{T} = \begin{bmatrix} \eta_1 \\ \eta_2 \\ \eta_3 \\ \xi \end{bmatrix} = \begin{bmatrix} x_1 \\ \frac{\cos x_1}{l} x_4 - x_3 \\ x_2 \\ x_4 \end{bmatrix} \quad , \quad (4.23)$$

is a global diffeomorphism and therefore chosen as the final system transform, with the inverse given by,

$$\mathbf{T}^{-1} = \begin{bmatrix} x_1 \\ x_2 \\ x_3 \\ x_4 \end{bmatrix} = \begin{bmatrix} \eta_1 \\ \eta_3 \\ \frac{\cos \eta_1}{l} \xi - \eta_2 \\ \xi \end{bmatrix} \quad . \quad (4.24)$$

The derivative of the transform, Equation 4.23, along the trajectories of the system is,

$$\begin{bmatrix} \dot{\eta}_1 \\ \dot{\eta}_2 \\ \dot{\eta}_3 \\ \dot{\xi} \end{bmatrix} = \begin{bmatrix} \dot{x}_1 \\ \frac{-\sin x_1}{l} \dot{x}_1 x_4 + \frac{\cos x_1}{l} \dot{x}_4 - \dot{x}_3 \\ \dot{x}_2 \\ \dot{x}_4 \end{bmatrix} \quad (4.25)$$

$$\begin{bmatrix} \dot{\eta}_1 \\ \dot{\eta}_2 \\ \dot{\eta}_3 \\ \dot{\xi} \end{bmatrix} = \begin{bmatrix} x_3 \\ \frac{-\sin x_1}{l} x_3 x_4 + \frac{\cos x_1}{l} f_4(\mathbf{x}) + \frac{\cos x_1}{l} g_4(\mathbf{x})u - f_3(\mathbf{x}) - g_3(\mathbf{x})u \\ x_4 \\ f_4(\mathbf{x}) + g_4(\mathbf{x})u \end{bmatrix} \quad , \quad (4.26)$$

from which the *regular form* is obtained by rearranging and using the inverse transform,

$$\begin{bmatrix} \dot{\eta}_1 \\ \dot{\eta}_2 \\ \dot{\eta}_3 \\ \dot{\xi} \end{bmatrix} = \begin{bmatrix} \mathbf{f}_a(\boldsymbol{\eta}, \phi(\boldsymbol{\eta})) \\ \text{-----} \\ f_b(\boldsymbol{\eta}, \phi(\boldsymbol{\eta})) \end{bmatrix} + \begin{bmatrix} 0 \\ 0 \\ 0 \\ \text{-----} \\ g_b(\boldsymbol{\eta}, \phi(\boldsymbol{\eta})) \end{bmatrix} \quad (4.27)$$

$$\begin{bmatrix} \dot{\eta}_1 \\ \dot{\eta}_2 \\ \dot{\eta}_3 \\ \dot{\xi} \end{bmatrix} = \begin{bmatrix} \frac{\cos \eta_1}{l} \xi - \eta_2 \\ \frac{-\sin \eta_1}{l} \left( \frac{\cos \eta_1}{l} \xi - \eta_2 \right) \xi + \frac{\cos \eta_1}{l} f_4(\boldsymbol{\eta}, \xi) - f_3(\boldsymbol{\eta}, \xi) \\ \xi \\ \text{-----} \\ f_4(\boldsymbol{\eta}, \xi) \end{bmatrix} \begin{bmatrix} 0 \\ 0 \\ 0 \\ \text{-----} \\ g_4(\boldsymbol{\eta}, \xi) \end{bmatrix}, \quad (4.28)$$

where,

$$\begin{aligned} f_3(\boldsymbol{\eta}, \xi) = & \frac{1}{l^2 m (M + m - m \cos^2 \eta_1)} \left[ (M + m) b_{p,v} \left( \eta_2 - \frac{\cos \eta_1 \xi}{l} \right) + \right. \\ & + (M + m) b_{p,c} \tanh \left( k_{\tanh} \left( \eta_2 - \frac{\cos \eta_1 \xi}{l} \right) \right) + m^2 g l \sin \eta_1 - b_{c,c} m l \tanh(k_{\tanh} \xi) \cos \eta_1 - \\ & \left. - m^2 l^2 \cos \eta_1 \sin \eta_1 \left( \eta_2 - \frac{\xi \cos \eta_1}{l} \right)^2 + M g l m \sin \eta_1 - b_{c,v} m l \xi \cos \eta_1 \right] \end{aligned} \quad (4.29)$$

$$\begin{aligned} f_4(\boldsymbol{\eta}, \xi) = & -\frac{1}{l(M + m - m \cos^2 \eta_1)} \left[ b_{c,v} l \xi - b_{p,v} \cos \eta_1 \left( \eta_2 - \frac{\cos \eta_1 \xi}{l} \right) + b_{c,c} l \tanh(k_{\tanh} \xi) - \right. \\ & - b_{p,c} \tanh \left( k_{\tanh} \left( \eta_2 - \frac{\cos \eta_1 \xi}{l} \right) \right) \cos \eta_1 + \\ & \left. + l^2 m \sin \eta_1 \left( \eta_2 - \frac{\xi \cos \eta_1}{l} \right)^2 - m g l \cos \eta_1 \sin \eta_1 \right] \end{aligned} \quad (4.30)$$

$$g_4(\boldsymbol{\eta}, \xi) = \frac{1}{M + m - m \cos^2 \eta_1} \quad (4.31)$$

With the system on regular form, design is proceeded by choosing a sliding manifold,

$$s = \xi - \phi(\boldsymbol{\eta}) \quad , \quad (4.32)$$

where  $\phi(\boldsymbol{\eta})$  is to be designed. If  $s$  is zero then  $\xi = \phi(\boldsymbol{\eta})$ , such that,

$$\dot{\boldsymbol{\eta}} = f_a(\boldsymbol{\eta}, \phi(\boldsymbol{\eta})) \quad , \quad (4.33)$$

is the reduced-order system with  $\phi(\boldsymbol{\eta})$  as control input. It is then sought to design  $\phi(\boldsymbol{\eta})$  such that Equation 4.33 is asymptotically stable at its origin.

To that end, the reduced-order system is linearized,

$$A = \frac{\partial \dot{\boldsymbol{\eta}}}{\partial \boldsymbol{\eta}} \bigg|_{\substack{\boldsymbol{\eta}=\mathbf{0} \\ \xi=0 \\ k_{\tanh}=1}} = \begin{bmatrix} 0 & -1 & 0 \\ -\frac{g}{l} & \frac{-b_{p,v}}{l^2 m} & 0 \\ 0 & 0 & 0 \end{bmatrix}, \quad B = \frac{\partial \dot{\boldsymbol{\eta}}}{\partial \xi} \bigg|_{\substack{\boldsymbol{\eta}=\mathbf{0} \\ \xi=0 \\ k_{\tanh}=1}} = \begin{bmatrix} \frac{1}{l} \\ \frac{b_{p,v} + b_{p,c} l}{l^3 m} \\ 1 \end{bmatrix}. \quad (4.34)$$

Checking for controllability,

$$\text{rank}(\mathcal{C}) = \text{rank}([ B \ AB \ A^2B ]) = 3 \quad , \quad (4.35)$$

and since the controllability matrix,  $\mathcal{C}$ , has full rank, the linearized system is controllable. A state feedback controller is designed for the linearized reduced-order system,

$$\phi(\boldsymbol{\eta}) = -\mathbf{k}\boldsymbol{\eta} \quad . \quad (4.36)$$

The poles are placed in  $\mathbf{p} = [ -4 \ -6 \ -7 ]$  using matlab *place()*-command to obtain the gains,  $\mathbf{k} = [ 7.2025 \ -1.2930 \ -5.4218 ]$ . Simulations of the controlled reduced-order system are run for both the linearized and the nonlinear system, see Figure 4.1.

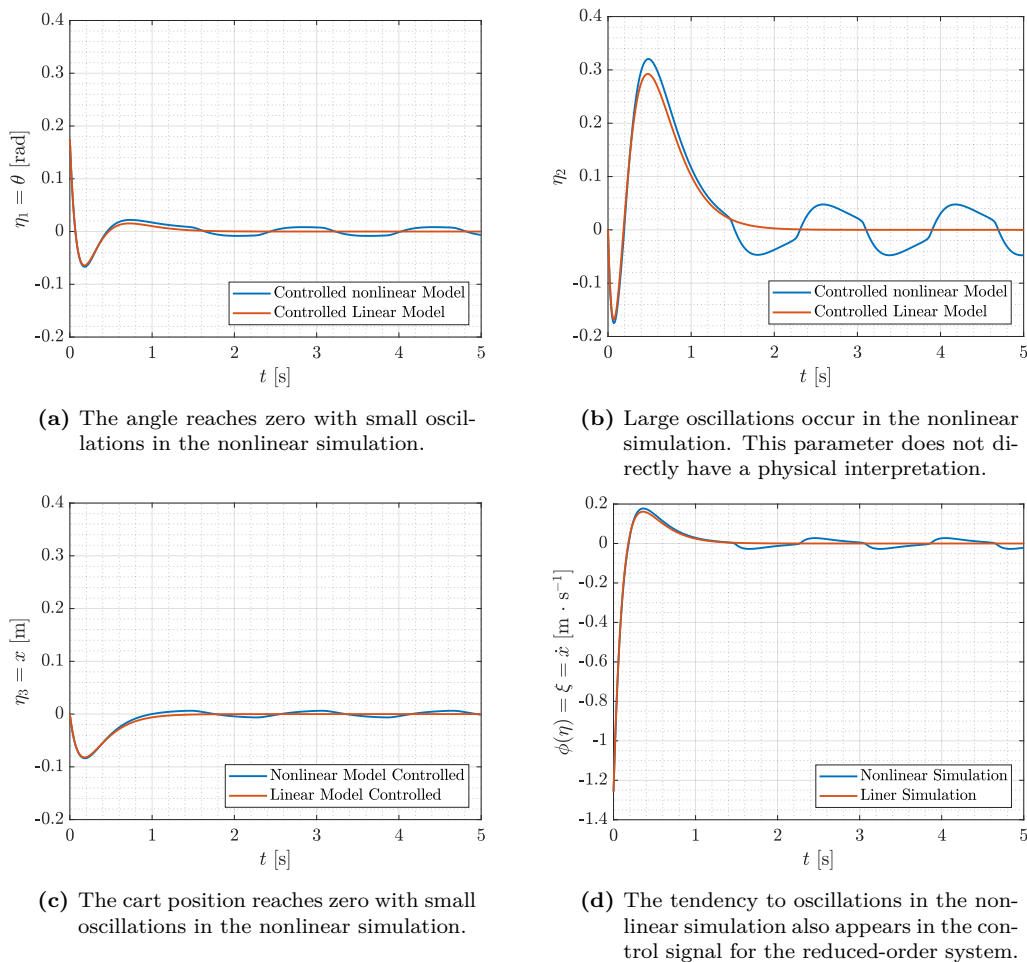


**Figure 4.1:** Nonlinear and linear simulation of the state feedback control designed for the linearized reduced-order system.

The reduced-order system is stabilized under the assumption that  $s$  is zero. Thus, the design of  $u$  is concerned with bringing  $s$  to zero.

**Theorem 4.0.1 (Lyapunov Stability Theorem)** Consider the autonomous system,  $f(\mathbf{x}) = \dot{\mathbf{x}}$ , where  $f : \mathbb{D} \rightarrow \mathbb{R}^n$  is locally Lipschitz and  $\mathbf{x} = \mathbf{0}$  is an equilibrium point. Then if  $\exists V : \mathbb{D} \rightarrow \mathbb{R}$  and

1.  $V(\mathbf{x})$  is  $C^1$
2.  $V(\mathbf{x}) > 0 \forall \mathbf{x} \in \mathbb{D} \setminus \{0\}$  and  $V(\mathbf{0}) = 0$
3.  $\dot{V}(\mathbf{x}) \leq 0$  in  $\mathbb{D}$

then  $\mathbf{x} = \mathbf{0}$  is stable. Further, if,

$$\dot{V}(\mathbf{x}) < 0 \text{ in } \mathbb{D} \setminus \{0\} \quad ,$$

then  $\mathbf{x} = \mathbf{0}$  is asymptotically stable [16].

A Lyapunov function candidate is proposed,

$$V(\boldsymbol{\eta}, \xi) = \frac{1}{2}s^2 \quad , \quad (4.37)$$

where  $s = \xi - \mathbf{k}\boldsymbol{\eta}$  hence,

$$V = \frac{1}{2}(\xi - \mathbf{k}\boldsymbol{\eta})^2 \quad (4.38)$$

$$V = \frac{1}{2}(\xi^2 + (\mathbf{k}\boldsymbol{\eta})^2) - \xi\mathbf{k}\boldsymbol{\eta} \quad (4.39)$$

$$V = \frac{1}{2}(\xi^2 + k_1^2\eta_1^2 + k_2^2\eta_2^2 + k_3^2\eta_3^2) + k_1k_2\eta_1\eta_2 + k_1k_3\eta_1\eta_3 + k_2k_3\eta_2\eta_3 - \xi(k_1\eta_1 + k_2\eta_2 + k_3\eta_3) \quad . \quad (4.40)$$

The partial derivatives are,

$$\frac{\partial V}{\partial \xi} = \xi - \mathbf{k}\boldsymbol{\eta} \quad (4.41)$$

$$\frac{\partial V}{\partial \eta_1} = k_1^2\eta_1 + k_1k_2\eta_2 + k_1k_3\eta_3 - k_1\xi \quad , \quad (4.42)$$

and similar results to Equation 4.42 are obtained for the partial derivatives with respect to  $\eta_2$  and  $\eta_3$ . Since all four partial derivatives are  $C^0$  then  $V$  is  $C^1$  in the entire  $\mathbb{R}^4$ , thus satisfying the first condition of the Lyapunov Stability Theorem 4.0.1. Further, from Equation 4.38, it is clear that  $V$  is positive definite in the entire state space without zero and zero in the origin, thus also satisfying the second condition.

To assess the third condition of Theorem 4.0.1, the derivative of the Lyapunov function candidate is found along trajectories of the system,

$$\dot{V} = s\dot{s} \quad (4.43)$$

$$\dot{V} = s(\dot{\xi} + \mathbf{k}\dot{\boldsymbol{\eta}}) \quad (4.44)$$

$$\dot{V} = s(f_b(\boldsymbol{\eta}, \xi) + g_b(\boldsymbol{\eta}, \xi)u + \mathbf{k}f_a(\boldsymbol{\eta}, \xi)) \quad (4.45)$$

$$\dot{V} = (\mathbf{k}f_a + f_b)s + g_bsu \quad (4.46)$$

$$\dot{V} = g_b s(\mathbf{k}f_a + f_b)g_b^{-1} + g_bsu \quad (4.47)$$

$$\dot{V} \leq g_b|s| |\mathbf{k}f_a + f_b| g_b^{-1} + g_bsu \quad . \quad (4.48)$$

This leads to the design of  $u$  which is chosen such that the third condition of Theorem 4.0.1 is satisfied,

$$u = -\text{sgn}(s)\beta(\boldsymbol{\eta}, \xi)g_b^{-1}(\boldsymbol{\eta}, \xi) \quad \text{where,} \quad \beta(\boldsymbol{\eta}, \xi) = \varrho(\boldsymbol{\eta}, \xi) + \beta_0 \quad (4.49)$$

$$\varrho(\boldsymbol{\eta}, \xi) = |\mathbf{k}f_a + f_b| \quad , \quad (4.50)$$

and  $\beta_0 > 0$  is a tuning parameter allowing  $\dot{V}$  to be positive definite, thereby guaranteeing asymptotic stability of the origin by Theorem 4.0.1,

$$\dot{V} < g_b|s| |\mathbf{k}f_a + f_b| g_b^{-1} - g_b \text{sgn}(s)s |\mathbf{k}f_a + f_b + \beta_0| g_b^{-1} \quad . \quad (4.51)$$

For implementation, the discontinuity introduced by the sign-function in the control law is cause for excessive switching and chattering due to delays in the real system. To circumvent this issue, a saturation function with a steep slope,  $1/\varepsilon$ , is used to approximate the sign-function,

$$\text{sat}(s/\varepsilon) = \begin{cases} s/\varepsilon & |s/\varepsilon| \leq 1 \\ \text{sgn}(s) & |s/\varepsilon| > 1 \end{cases} \quad , \quad (4.52)$$

hence,

$$u = -\text{sat}(s/\varepsilon)\beta(\boldsymbol{\eta}, \xi)g_b^{-1}(\boldsymbol{\eta}, \xi) \quad . \quad (4.53)$$

A simulation of the design is shown in Figure 4.2 and 4.3, starting from an initial angle of  $0.1 \text{ rad} \cdot \text{s}^{-1}$ . Both the angle and cart position are brought to zero. The small oscillations are thought to originate from the linear part of the design, where oscillations were observed in the simulation of the nonlinear reduced order system with linear control, see Figure 4.1.

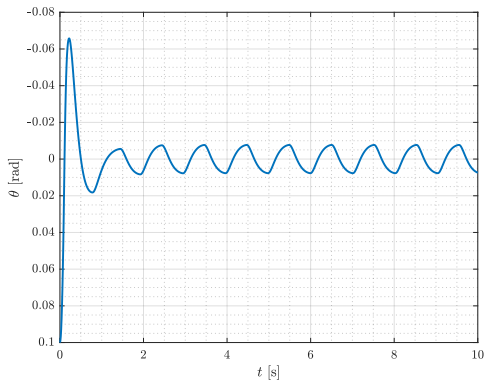


**Figure 4.2:** A simulation of the sliding mode design starting form an initial angle of  $0.1 \text{ rad} \cdot \text{s}^{-1}$  at zero angular velocity. The angle is maintained around zero with small oscillation.

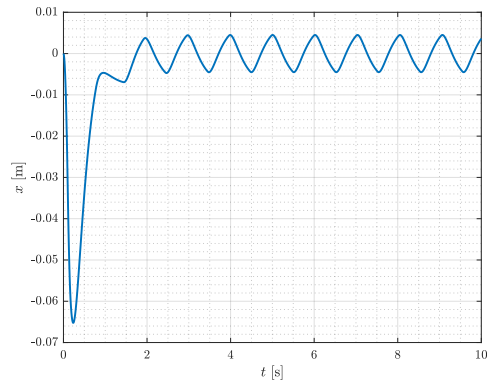


**Figure 4.3:** The cart position successfully returns to zero with small oscillations after the pendulum angle is brought to zero.

To achieve this behavior from relatively wide catch angle, a large peak occurs in the armature current, see Figure 4.4. However, with the short duration of the peak, this is

not considered a problem. If it is desired to bring down the peak current, the sliding mode controller could simply be activated at a narrower angle.

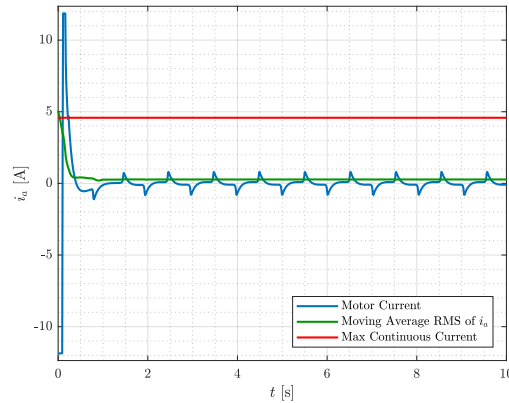


**Figure 4.4:** The control signal from the simulation in Figure 4.2 and 4.3. The peak current is rather large, which is to be expected given the relatively wide initial angle. It is not considered to be a problem, since the large current is only maintained for a short duration.

Finally the swing-up controller and the sliding mode controller are simulated in concert, where the sliding mode controller is activated at a catch angle of 0.1 rad. The result is seen in Figure 4.5 and Figure 4.6, where the swing-up controller brings the angle below the catch angle in seven swings, after which the system is stabilized in zero by the sliding mode controller.

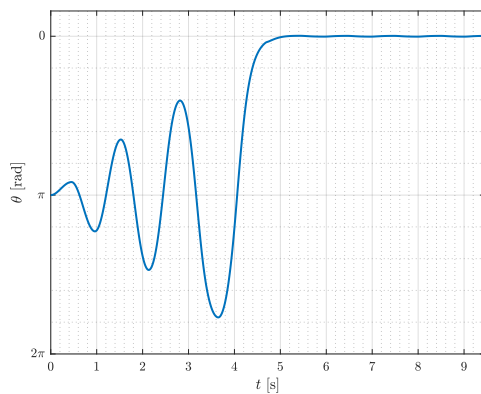


**Figure 4.5:** Simulation of the swing-up controller using sliding mode to catch the pendulum when the angle reaches below 0.1 rad.

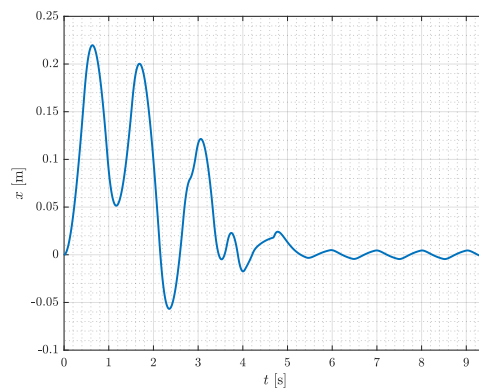


**Figure 4.6:** The cart position successfully returns to zero after the pendulum angle is stabilized at zero.

The needed actuation signal is seen in Figure 4.7 and though some peaks occur, the RMS stays below the rated continuous current limit of the motor.

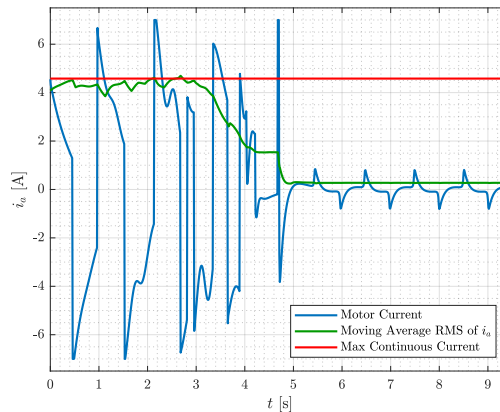


**Figure 4.7:** Control signal from the simulation in Figure 4.5 and 4.6. Again large peaks occur in the armature current, however, only for short durations and with the RMS staying below the rated continuous current limit.

The system was first transformed into *regular form* after which the reduced order system was stabilized using linearization and linear state feedback. Some small oscillations were observed in the nonlinear simulation of the controlled reduced order system. The sliding mode design was proceeded from there based on Lyapunov stability criteria, and the final control law was simulated stabilizing the system also in concert with the swing-up controller.

This concludes the stabilization design and carries into the final two chapters of *Part 1* where considerations in implementation are presented along with the final test results from the cart pendulum system setup.

# 5 | Implementation

To implement the control designs discussed here in *Part 1* it is necessary to estimate some parameters, compensate for any friction between the cart and the rail and filter the measurements obtained from the system. Such considerations, estimations and designs are discussed in this section.

## 5.1 Cart Friction and Mass Estimation

The control designs are carried out under the assumption that there is no friction between the cart and the rail. It turns out that this friction is rather complex and also depend on position and direction of the cart in addition to its velocity, this issue was also found by previous project groups [8].

To accommodate the no cart friction assumption, a feed forward friction compensator is designed. The idea is to simply counter the predicted friction at any given time directly in the control signal.

Since the friction depends on the cart position, the estimation must be done locally for each position on the rail. To do so, the pendulum masses are removed, the rods strapped to the cart to limit dynamics and the cart is made to oscillate around each centimeter of the rail. Each test is sustained for 20s and repeated for each centimeter, resulting in a total of 68 tests. This is the largest possible range for the test while avoiding impact at the ends of the rail. Each test spans on average 2.68 cm creating some overlap between tests. The reduced dynamics used for the estimation are given by,

$$(M + m)\ddot{x} = u - b_{c,v}\dot{x} - \tanh(k_{\tanh}\dot{x})b_{c,c} \quad . \quad (5.1)$$

The optimization fitting tool, Senstools [17], is used to estimate the model parameters. Since the mass is unknown it is also included for estimation. The mass is estimated to be 6.28 kg. With more parameters more manual tuning is required in order to start close enough for the optimization algorithm to converge. To reduce the number of parameters as much as possible, once estimated, the mass is fixed as part of the model. The remaining three parameters are viscous friction and coulomb friction for negative and positive velocities. After some trial and error it is concluded that the viscous friction is negligible compared to the coulomb frictions finally leaving only two parameters.

To make the estimations converge without too much manual tuning only part of each test is fitted, see Figure 5.1. The time window is moved, and the estimation is run again. The window is moved 34 times resulting in  $34 \cdot 68 = 2312$  estimations in total. Every time the test window is moved, the next estimate is started with the results of the previous estimate as its initial values.

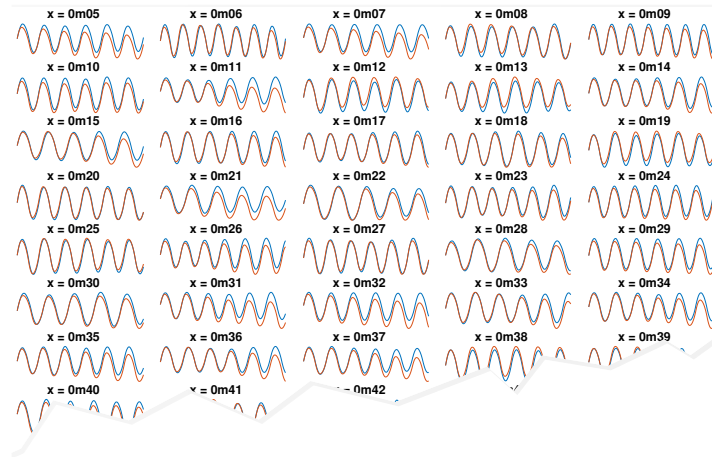


**Figure 5.1:** A snippet of the estimation of cart Coulomb friction. Each title shows where on the rail the test is done. This is one iteration of 34 moving over the 20 s tests.

To include as much data as possible, the estimate is repeated across the data for each test, resulting in 34 results for each position. The error norm is saved for all estimations, see Figure 5.3, and a weighed average using the error norm as weights is made for each position on the rail resulting in Figure 5.2.

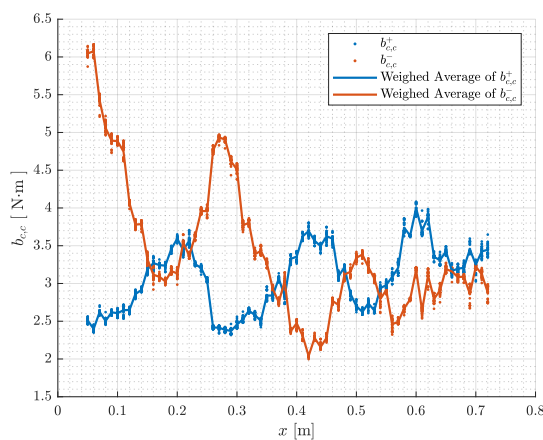


**Figure 5.2:** Results of the estimations, where the scattered points are all estimates and the lines are the weighed averages using the error norm of each estimate as weights.

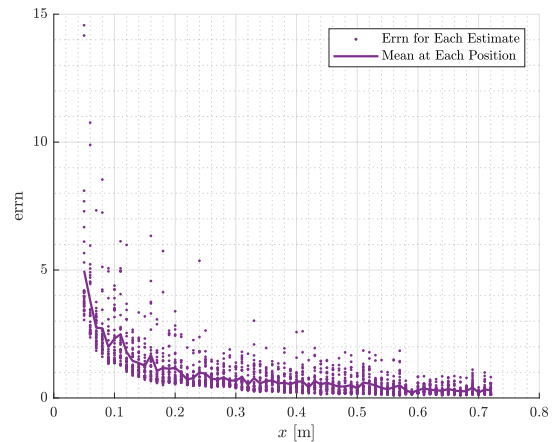


**Figure 5.3:** This shows the error norms for all estimates. There is a clear tendency to worse fits at the left end of the rail. The reason is unknown.

The estimations are worse near the left of the rail, see Figure 5.3. The cause for this is not known, however it is considered less important as the compensation is more critical near the middle of the rail where the pendulum is balanced.

The result in Figure 5.2 contains some undesired discontinuities. To solve this problem the resulting mean curves are up-sampled by linear interpolation, smoothed and finally down-sampled to obtain the smoothed result in Figure 5.4.

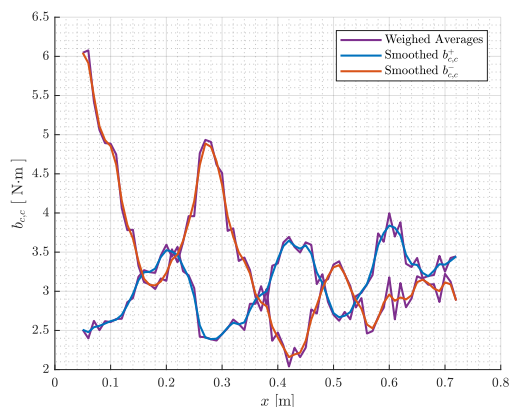


**Figure 5.4:** This is the final result of the estimation, which is up-sampled, smoothed and finally down-sampled to produce the values for implementation in lookup-table.

The result is implemented as lookup tables along with a linear interpolation function to avoid discontinuities between table entries. This determines the cart Coulomb friction based on velocity, direction and position, which is then added to the control signal to counter the friction term in the dynamics.

## 5.2 Pendulum Friction

With the cart mass estimated and its friction handled by friction compensation, the remaining estimate is pendulum friction. Again Senstools is used along with a reduced model of the pendulum,

$$ml^2\ddot{\theta} = mgl \sin \theta - b_{p,v}\dot{\theta} - \tanh(k_{\tanh}\dot{\theta})b_{p,c} \quad . \quad (5.2)$$

This model assumes there is no cart, so for the test, the cart is fixed to the rail. The result of the test and estimation is seen in Figure 5.5.

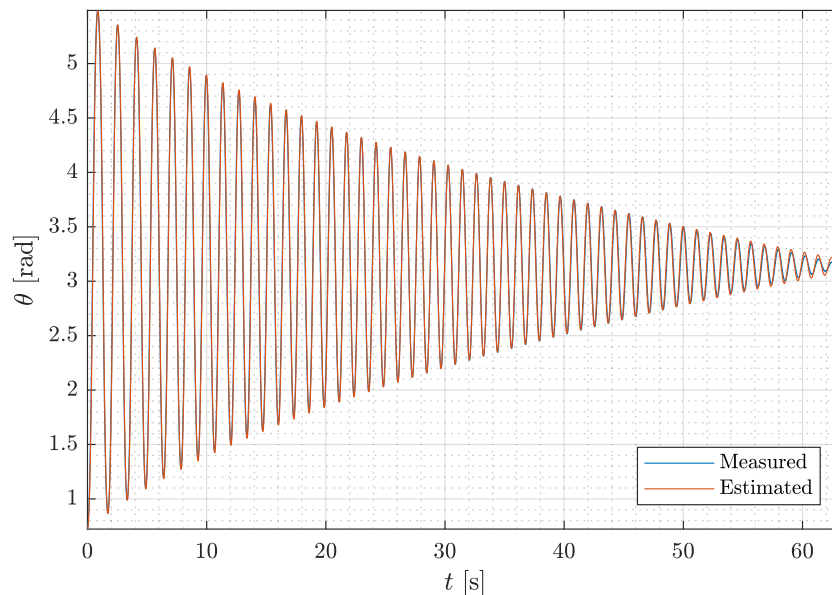


**Figure 5.5:** The fit resulting in the estimations of the pendulum friction.

To obtain a good fit, 22.5 g is added to the measured mass and 0.66 cm is subtracted from the measured length of the rod. This is presumed to be reasonable, since the rod is otherwise assumed to be massless which is not the case. The error in the assumption would move the mass center closer to the pivot point, thus reducing the effective length of the rod and adding some mass to the weight, corresponding to the adjustments. The pendulum Coulomb friction,  $b_{p,c}$ , is estimated to  $4.1 \times 10^{-3} \text{ N} \cdot \text{m}$  and the viscous friction,  $b_{p,v}$ , to  $0.5 \times 10^{-3} \text{ N} \cdot \text{m} \cdot \text{s}$ .

### 5.3 MA Filter Design

The measurements in the system are the position,  $x$ , of the cart and the angle,  $\theta$ , of the pendulum. Thus, the last two states,  $\dot{x}$  and  $\dot{\theta}$ , must be estimated for the implementation. To that end, a numerical differentiation is applied to the position measurements in order to obtain the velocities,

$$\dot{x}_n = \frac{x_n - x_{n-1}}{T_s} \quad , \quad (5.3)$$

where  $T_s$  is the sample time and  $x_n$  and  $x_{n-1}$  are the two latest samples. However, this approach causes noise in the velocities. Thus, an MA (Moving Average) filter is designed to smooth the signal,

$$\dot{x}_{est} = \frac{1}{N} \sum_{i=0}^N \dot{x}_N \quad , \quad (5.4)$$

where  $\dot{x}_N$  is the numerical differentiation based on the two latest measurements,  $\dot{x}_{est}$  is the filtered value and  $N$  is the window size of the filter. In Figure 5.6 and 5.7 the MA

filter is applied to the result of the numerical differentiation with two different window sizes. Since the interest here is quality of the signal, the following plots are not linked in time, but rather showing the signals where the filter characteristics shows clearly.

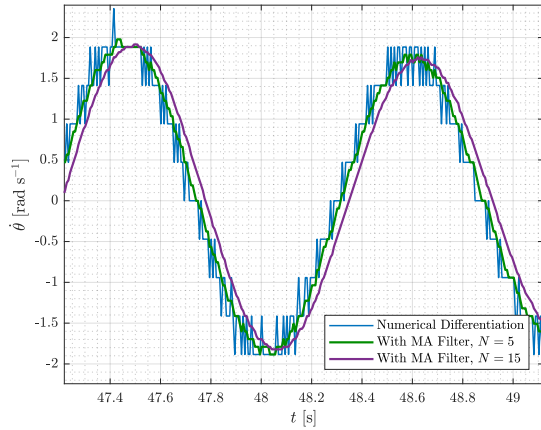


**Figure 5.6:** The result of applying the MA filter to the numerical differentiation of  $\theta$  with two window sizes. For  $N = 5$  a lot of noise is still in the signal, however, though  $N = 15$  removes more noise it also introduces unwanted delay.

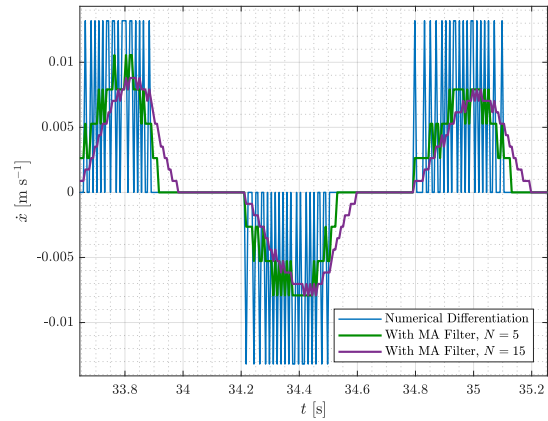


**Figure 5.7:** For  $\dot{x}$  the same result is observed, but since the signal is smaller relative to the noise, it more clearly shows the noise issue of the small window size.

The filter is implemented using a ring-buffer to minimize computation time and different window sizes are tested. Minimizing delay of the filter turns out to be more critical than further noise reduction, so a window size of five is chosen. The result of the implemented MA filter is shown in Figure 5.8 and 5.9.

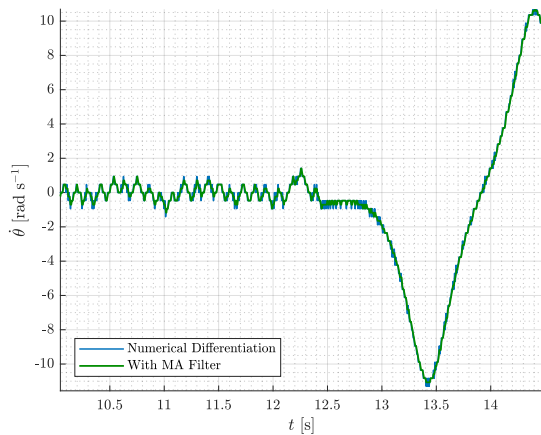


**Figure 5.8:** The resulting implementation of the MA filter with  $N = 5$  for estimation of  $\dot{\theta}$ .

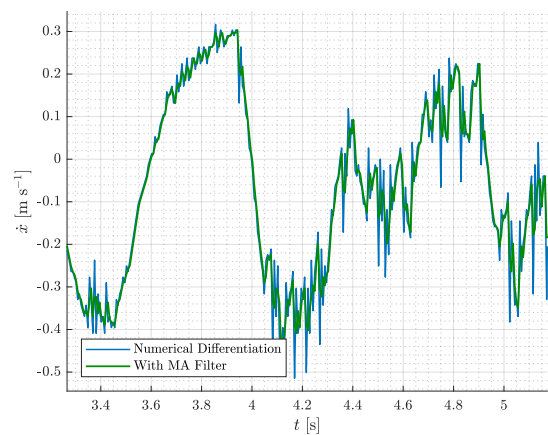


**Figure 5.9:** The implemented MA filter with  $N = 5$  for estimation of  $\dot{x}$ .

Though the MA filter still lets a lot of noise through, the design does suppress large jumps in the velocity with very minimal delay.

## Chapter 5. Implementation

This filter is only used in the swing-up sequence, an extended Kalman filter (EKF) implemented by a previous project group, [8], is used for the catch sequence as the switching nature of a sliding mode controller would cause oscillations with high noise levels around zero.

## 6 | Results

Here the results of the implemented control strategies developed in *Part 1* are presented. Firstly, the swing-up controller is approaching a heteroclinic orbit after seven swings, see Figure 6.1 and 6.2, same as achieved in simulation when accounting for actuation limitations.

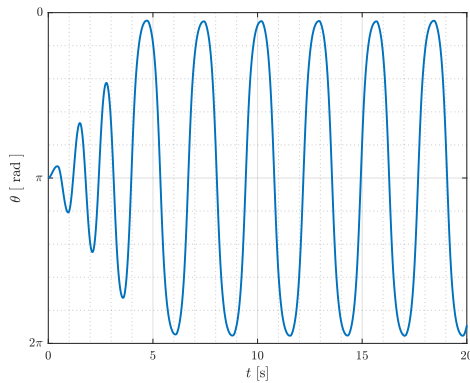


**Figure 6.1:** The swing-up controller approaches the equilibrium and almost reaches the heteroclinic orbit.

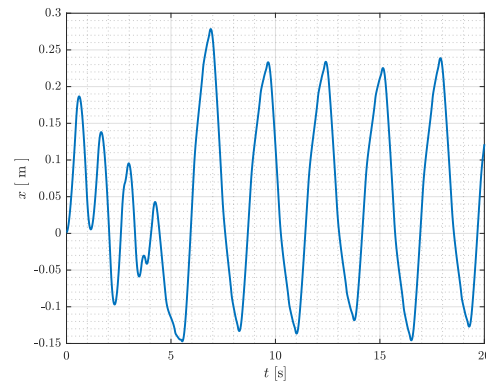


**Figure 6.2:** Though the cart oscillates more than in the simulation, it stays around zero and within the rail limits during the swing-up sequence.

The controller does fall slightly short of reaching the heteroclinic orbit which is also seen in Figure 6.4. The energy reference in Figure 6.3 reaches zero near the equilibrium points, but must be very slightly below zero when the angular velocity is zero, as otherwise the pendulum would reach equilibrium exactly.

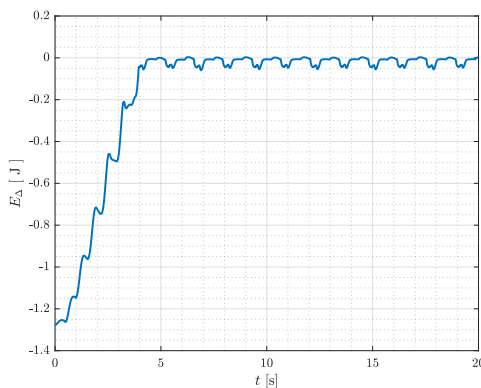


**Figure 6.3:** From the test in Figure 6.1 and 6.2 the energy reference is reached.

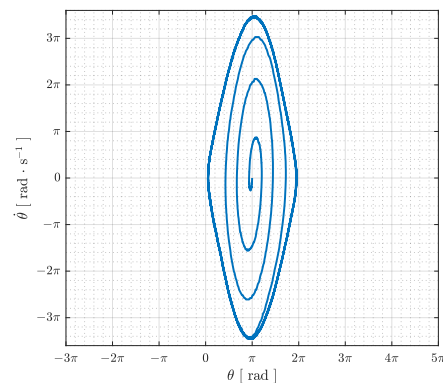


**Figure 6.4:** The pendulum almost reaches a heteroclinic orbit.

It is possible to gain closer proximity to the equilibrium point by increasing the energy

reference. In Figure 6.5 and 6.6 the energy reference is increased by 0.08 J to reach heteroclinic orbit.

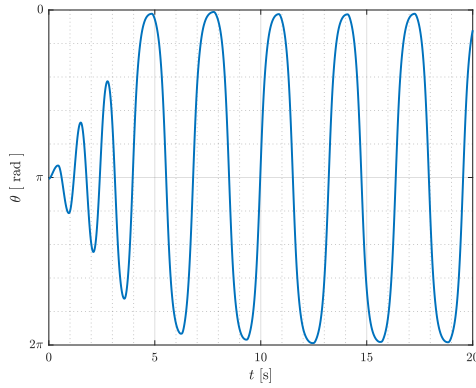


**Figure 6.5:** The swing-up controller approaches the equilibrium and eventually reaches the heteroclinic orbit.

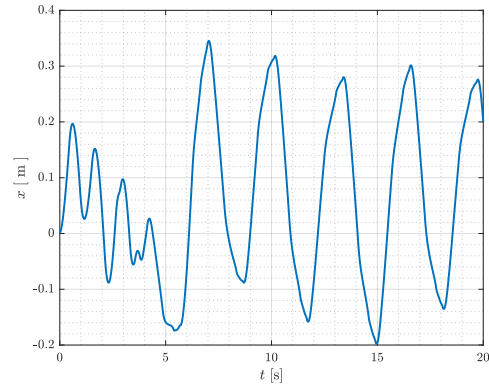


**Figure 6.6:** The cart does not approach zero position as much as it did in simulation. It does however stay within the constraints of the physical system, which is the main objective of the added position control for the swing-up sequence.

In Figure 6.7 the energy reference is slightly lifted causing a near perfect heteroclinic orbit in Figure 6.8.

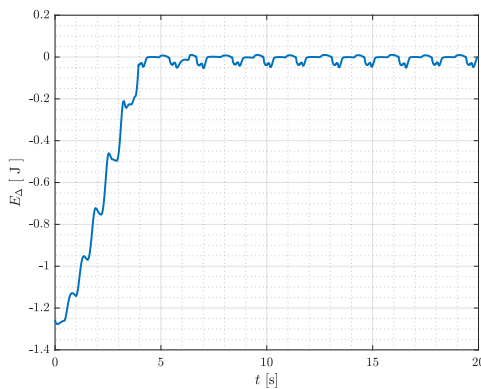


**Figure 6.7:** From the test in Figure 6.5 and 6.6 where the energy reference is raised by 0.08 J to get closer to the equilibrium point.

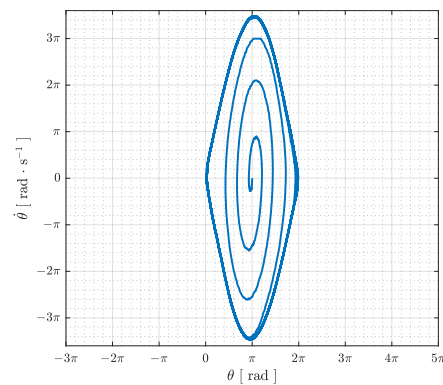


**Figure 6.8:** Near perfect heteroclinic orbit is reached due to the slight increase of the energy reference.

If the model and friction compensation was ideal, no energy offset would be needed, so if a high value was needed to approach equilibrium it might be worth to revisit this part of the design process.

Figure 6.9 shows the armature current of the motor used to achieve the swing-up behavior with the added energy reference. Though some peaks are present in the current signal, the

RMS value does not exceed the continuous current specification of the motor for extended periods of time.

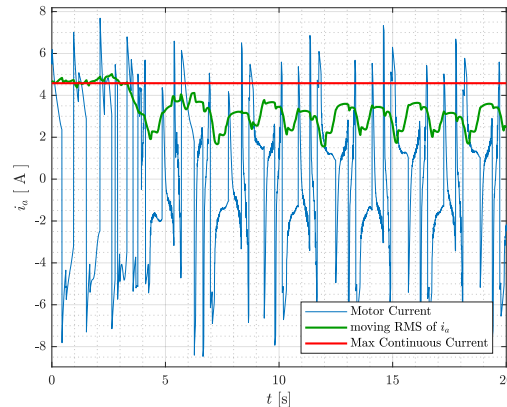


**Figure 6.9:** The RMS of the armature current is within respectable levels of the specified continuous current limit of the motor.

A test of the implemented sliding mode controller is seen in Figure 6.10 and 6.11 where the angle reaches zero.

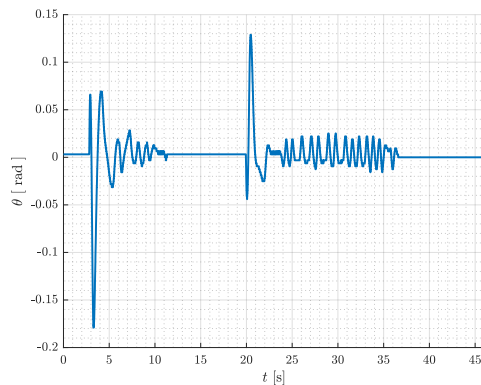


**Figure 6.10:** Test of sliding mode controller starting at zero. The controller is subjected to two disturbances after which it rebalances successfully bringing the angle back to zero.

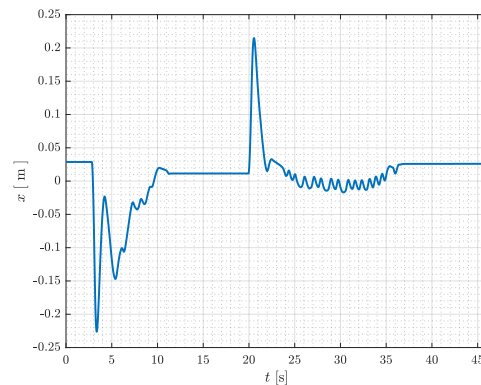


**Figure 6.11:** The cart returns approaches zero once the pendulum is rebalanced.

In the last part, after the 35 s mark, an offset in  $x$  is observed, this could be contributed to unmodeled friction keeping the control from exceeding the force of friction. The control signal is shown in Figure 6.12 where it does have a constant offset after the 35 s mark, supporting the hypothesis. However, the offset is also seen in the other stabilized regions of the test, where the control signal goes to zero. So while the first hypothesis might in part be true, something else is at least contributing to the problem, otherwise the control would still show an offset where the cart position does.

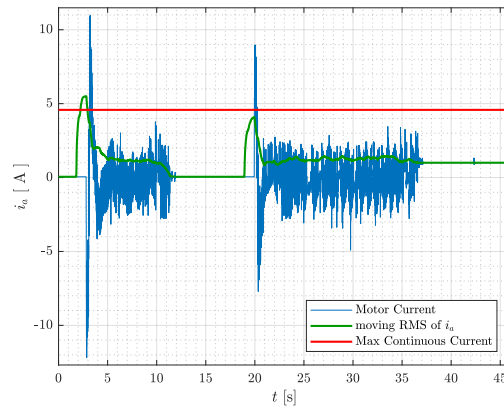


**Figure 6.12:** The armature current has an offset after 35 s which matches an offset in the position, however, around 15 s the same offset is seen in position with no offset in armature current.

When testing, an other problem relating to the position of the cart was observed. In Figure 6.13 the pendulum is only pushed once in the start of the test. The cart spontaneously diverges from zero position before correcting and re-stabilizing. When this happens, the angular velocity should not increase much, as seen by the FIR filter, which by nature does not introduce bias, however, the EKF shows an increase in angular velocity.

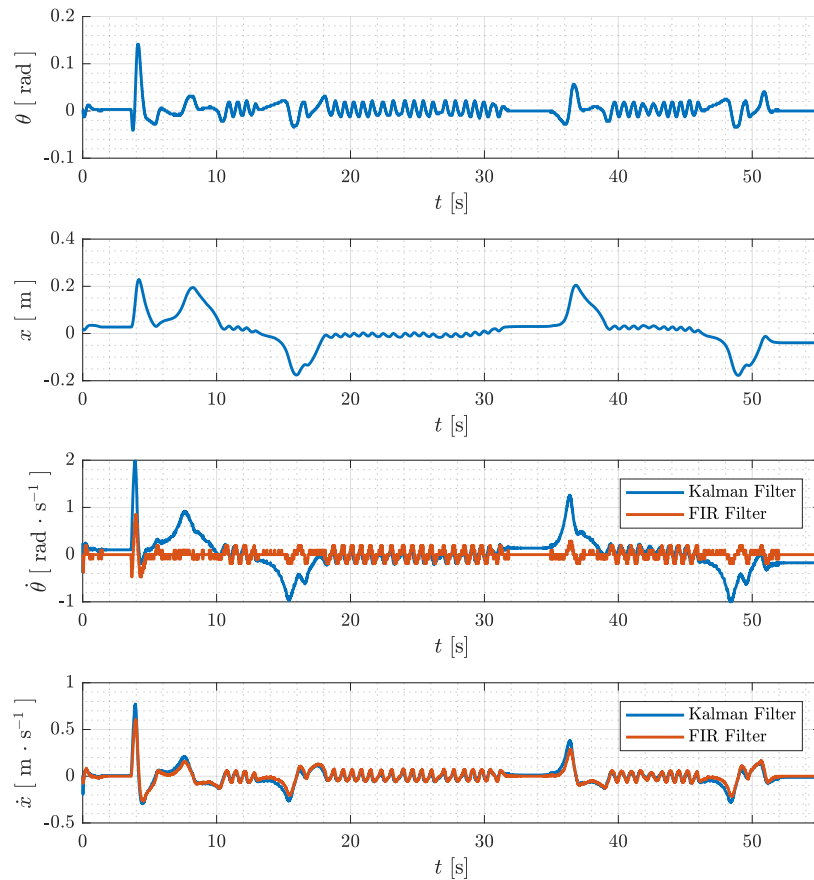


**Figure 6.13:** The system is perturbed about 4 s into the test, remaining disturbances are caused by a problem presumed to arise between friction compensation and the EKF.

If the friction compensation is too large, this could cause the cart to move away from equilibrium, and in that event, the EKF which is based on a system model, would get data which does not confine to the model, which might lead to a wrong estimation of the angular velocity, which would then amplify the problem.

When finally combining the two control strategies it is advantageous for the catch controller if the swing-up controller is designed to provide a bit of entry velocity at equilibrium. This makes for a more robust swing-up controller, in that, it always reaches the equilibrium in the same number of swings for every test. This means that the swing-up controller would overshoot without a catch controller. However, as the catch controller is enabled close to equilibrium, this helps the sliding mode controller by providing entry velocity at the maximum catch angle.

It is further noted that smaller catch angles causes less aggressive actuation of the sliding mode controller. After entering sliding mode the catch angle is increased, such that it stays in sliding mode unless the pendulum exceeds the maximum angle at which sliding mode can successfully re-stabilize the system. When this angle is exceeded, the swing-up controller is enabled and the catch angle is again reduced. As in simulation, a wrapped version of the angle is created such that the pendulum is always at zero when in upright position, this representation is only used by sliding mode.

Results of a test of the full implementation of the two controllers is shown in Figure 6.14 and 6.15.

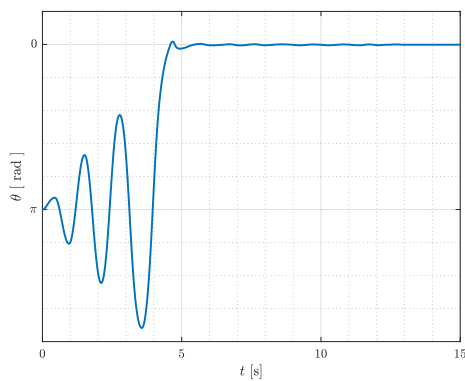


**Figure 6.14:** Test of the final design of swing-up with the higher energy reference and sliding mode controller successfully catching the pendulum after seven swings.

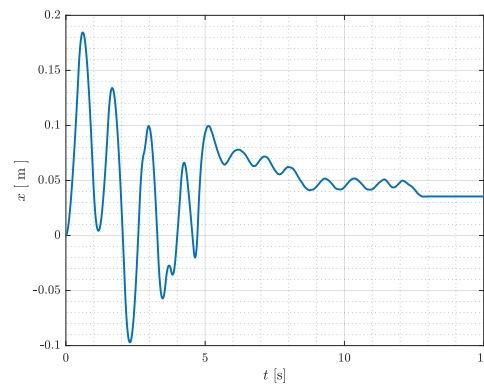


**Figure 6.15:** The cart keeps around zero on the rail, especially after the pendulum angle is controlled to zero.

The swing-up controller successfully hands over to sliding mode after seven swings and the sliding mode controller stabilizes the system in zero with some offset in the cart position. The moving average RMS of the actuation current briefly exceeds the continuous current rating of the motor when sliding mode catches the pendulum. As this is not happening over a prolonged period, it is not thought to be a problem,

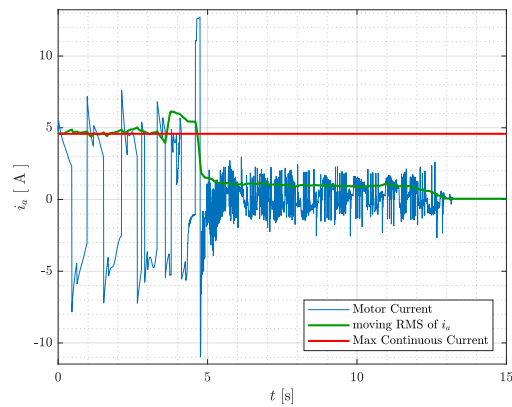


**Figure 6.16:** Armature current of the finished control system. It only briefly exceeds the motor specifications when the sliding mode controller takes over.

Three energy based swing-up designs were investigated, the sat-based version was chosen, a cart position controller was added and finally a stabilizing sliding mode controller was designed to catch the pendulum in equilibrium. The designs were successfully implemented and tested on the system setup concluding *Part 1* of this thesis.

## Part II

# Twin Pendulum

## 7 | System and Model

The cart pendulum system from *Part 1* is used again. However, here in *Part 2* an additional pendulum is mounted on the cart. The modification is discussed and a model for the changed system is developed in this chapter. The remaining of *Part 2* is concerned with estimating parameters, developing a state estimator, designing a swing-up controller and ultimately stabilizing the two pendulums in upright position.

### 7.1 System Addition

In Figure 7.1 the setup from *Part 1* is shown with the added pendulum. The new pendulum is mounted on a new motor (not directly visible in the figure), a brushed Maxon 370356 DC motor [2], same as for the first pendulum. The motor is not in use for this project and only acts as a joint with a HEDS 5540 optical quadrature encoder [3].

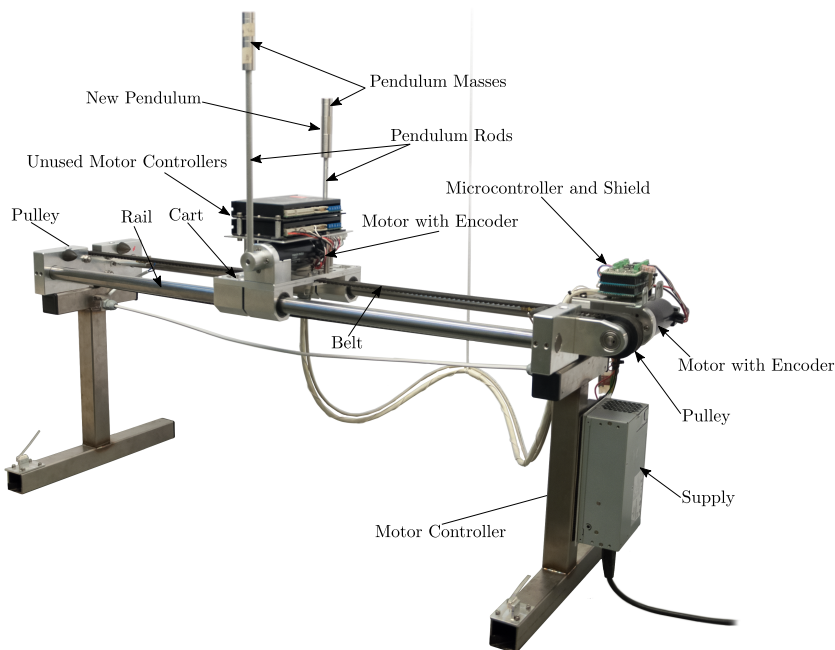


**Figure 7.1:** The setup from *Part 1* with a new pendulum attached on the back side of the cart. The motor controller in use is not directly visible here as it is mounted behind the supply.

The added pendulum measures 20 cm from pivot point to geometrical center of the 251 g weight at its end. The friction parameters are estimated again using Senstools, [17], and with the same reduced pendulum model as in *Part 1*.

Same as for the first pendulum, the mass is increased to obtain a good fit. In this case the pendulum mass is increased by 13.2 g, less than for the first pendulum, which makes sense since the added pendulum is shorter thus adding less mass to the system. For the first pendulum the length was decreased by 0.66 cm, while for the new pendulum the

measured length is used. Though the mass center should move towards the rod, it being shorter and with more mass at the end than the first pendulum, it makes sense that the mass center is moved so little for the new pendulum that the effect becomes negligible. Figure 7.2 shows the result of the estimation.

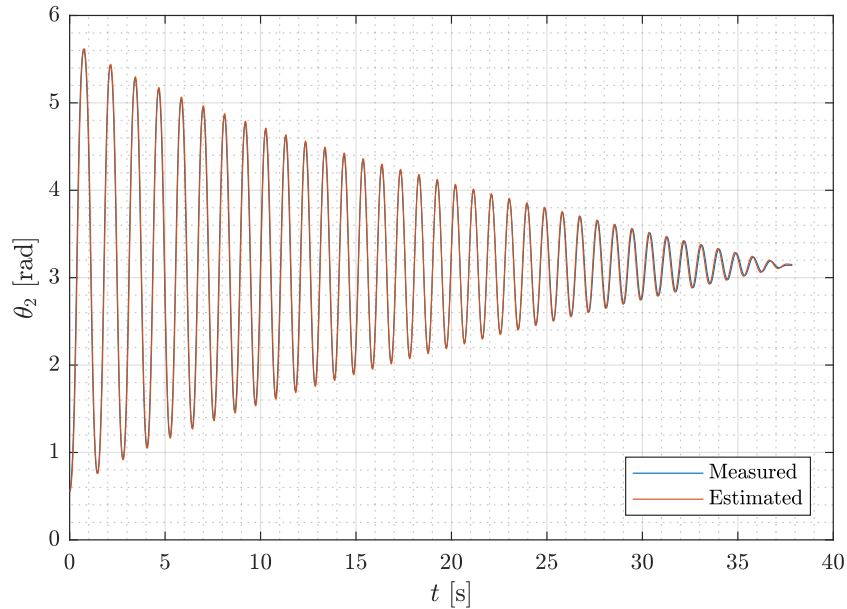


**Figure 7.2:** The fit resulting in the estimations of the new second pendulum friction, where  $\theta_2$  is the new pendulum angle.

In Table 7.1 all parameters for the twin pendulum system are gathered and notation is introduced to accommodate the added pendulum.

Parameter	Notation	Quantity	Unit
Nominal current (max. continuous current)	$I_N$	4.58	A
Torque constant	$\tau_m$	$93.4 \times 10^{-3}$	$\text{N} \cdot \text{m} \cdot \text{A}^{-1}$
Pendulum 1 Rod Length	$l_1$	0.3169	m
Pendulum 2 Rod Length	$l_2$	0.2000	m
Rail Length	$l_r$	0.89	m
Pulley Radius	$r$	0.028	m
Pendulum 1 Mass	$m_1$	0.2235	kg
Pendulum 2 Mass	$m_2$	0.2642	kg
Cart Mass	$M$	6.28	kg
Cart Coulomb Friction	$b_{c,c}$	$f(x, \dot{x})$	N
Cart Viscous Friction	$b_{c,v}$	0	$\text{N} \cdot \text{m}^{-1} \cdot \text{s}$
Pendulum 1 Coulomb Friction	$b_{p1,c}$	$4.1 \times 10^{-3}$	$\text{N} \cdot \text{m}$
Pendulum 1 Viscous Friction	$b_{p1,v}$	$0.5 \times 10^{-3}$	$\text{N} \cdot \text{m} \cdot \text{s}$
Pendulum 2 Coulomb Friction	$b_{p2,c}$	$5.7 \times 10^{-3}$	$\text{N} \cdot \text{m}$
Pendulum 2 Viscous Friction	$b_{p2,v}$	$0.1 \times 10^{-3}$	$\text{N} \cdot \text{m} \cdot \text{s}$

**Table 7.1:** Table of all system parameters including the estimated parameters for the added second pendulum. Notice the updated notation where *pendulum 1* is the pendulum also used in *Part 1* and *pendulum 2* is the newly attached pendulum.

In practice the new pendulum and motor were added before estimations were made in *Part 1*. This means parameters remain unchanged between the two versions of the setup allowing demonstration of both with the minimal modification of adding or removing the second pendulum mass.

## 7.2 Model

To model the twin pendulum system, consider the excessive coordinate convention in Figure 7.3 along with the generalized coordinates in the mechanical drawing, Figure 7.4.

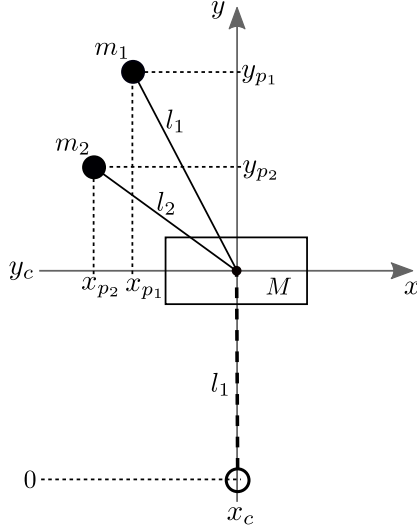


**Figure 7.3:** Twin pendulum system in excessive coordinates.

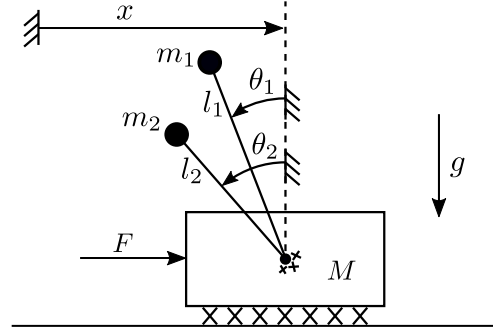


**Figure 7.4:** Mechanical drawing of the system with the added pendulum in generalized coordinates.

The energy method is applied. First the potential and kinetic energies, in terms of excessive coordinates, is found,

$$U = Mgy_c + m_1gy_{p_1} + m_2gy_{p_2} \quad (7.1)$$

$$T = \frac{1}{2}M\dot{x}_c^2 + \frac{1}{2}M\dot{y}_c^2 + \frac{1}{2}m_1\dot{x}_{p_1}^2 + \frac{1}{2}m_1\dot{y}_{p_1}^2 + \frac{1}{2}m_2\dot{x}_{p_2}^2 + \frac{1}{2}m_2\dot{y}_{p_2}^2 \quad (7.2)$$

The excessive coordinates and derivatives thereof are then expressed in terms of the generalized coordinates, using the conventions presented in Figure 7.3 and 7.4,

$$\begin{cases} x_c = x \\ y_c = l_1 \end{cases} \quad \begin{cases} x_{p_1} = x - l_1 \sin \theta_1 \\ y_{p_1} = l_1 + l_1 \cos \theta_1 \end{cases} \quad \begin{cases} x_{p_2} = x - l_2 \sin \theta_2 \\ y_{p_2} = l_1 + l_2 \cos \theta_2 \end{cases} \quad (7.3)$$

$$\begin{cases} \dot{x}_c = \dot{x} \\ \dot{y}_c = 0 \end{cases} \quad \begin{cases} \dot{x}_{p_1} = \dot{x} - l_1 \cos \theta_1 \dot{\theta}_1 \\ \dot{y}_{p_1} = -l_1 \sin \theta_1 \dot{\theta}_1 \end{cases} \quad \begin{cases} \dot{x}_{p_2} = \dot{x} - l_2 \cos \theta_2 \dot{\theta}_2 \\ \dot{y}_{p_2} = -l_2 \sin \theta_2 \dot{\theta}_2 \end{cases} \quad (7.4)$$

Inserting Equation 7.3 and 7.4 into the energy equations, Equation 7.1 and 7.2, yields,

$$U = Mgl_1 + m_1g(l_1 + l_1 \cos \theta_1) + m_2g(l_1 + l_2 \cos \theta_2) \quad (7.5)$$

$$T = \frac{1}{2}M\dot{x}^2 + \frac{1}{2}m_1(\dot{x} - l_1 \cos \theta_1 \dot{\theta}_1)^2 + \frac{1}{2}m_1(-l_1 \sin \theta_1 \dot{\theta}_1)^2 + \frac{1}{2}m_2(\dot{x} - l_2 \cos \theta_2 \dot{\theta}_2)^2 + \frac{1}{2}m_2(-l_2 \sin \theta_2 \dot{\theta}_2)^2 \quad (7.6)$$

Proceeding to compute the Lagrangian,

$$\mathcal{L} = T - U \quad (7.7)$$

$$\begin{aligned} \mathcal{L} = & \frac{1}{2}M\dot{x}^2 + \frac{1}{2}m_1(\dot{x}^2 + l_1^2 \cos^2 \theta_1 \dot{\theta}_1^2 - 2\dot{x}l_1 \cos \theta_1 \dot{\theta}_1) + \frac{1}{2}m_1l_1^2 \sin^2 \theta_1 \dot{\theta}_1^2 + \\ & + \frac{1}{2}m_2(\dot{x}^2 + l_2^2 \cos^2 \theta_2 \dot{\theta}_2^2 - 2\dot{x}l_2 \cos \theta_2 \dot{\theta}_2) + \frac{1}{2}m_2l_2^2 \sin^2 \theta_2 \dot{\theta}_2^2 - \\ & - (M + m_1 + m_2)gl_1 - m_1gl_1 \cos \theta_1 - m_2gl_2 \cos \theta_2 \end{aligned} \quad (7.8)$$

$$\begin{aligned} \mathcal{L} = & \frac{1}{2}(M + m_1 + m_2)\dot{x}^2 - (m_1l_1 \cos \theta_1 \dot{\theta}_1 + m_2l_2 \cos \theta_2 \dot{\theta}_2)\dot{x} + \\ & + \frac{1}{2}m_1l_1^2(\cos^2 \theta_1 + \sin^2 \theta_1)\dot{\theta}_1^2 + \frac{1}{2}m_2l_2^2(\cos^2 \theta_2 + \sin^2 \theta_2)\dot{\theta}_2^2 - \\ & - (M + m_1 + m_2)gl_1 - m_1gl_1 \cos \theta_1 - m_2gl_2 \cos \theta_2 \end{aligned} \quad (7.9)$$

$$\begin{aligned} \mathcal{L} = & \frac{1}{2}(M + m_1 + m_2)\dot{x}^2 - (m_1l_1 \cos \theta_1 \dot{\theta}_1 + m_2l_2 \cos \theta_2 \dot{\theta}_2)\dot{x} + \frac{1}{2}m_1l_1^2\dot{\theta}_1^2 + \\ & + \frac{1}{2}m_2l_2^2\dot{\theta}_2^2 - (M + m_1 + m_2)gl_1 - m_1gl_1 \cos \theta_1 - m_2gl_2 \cos \theta_2 \quad , \end{aligned} \quad (7.10)$$

and finally by using the Lagrange-d'Alembert Principle, [10]

$$\frac{d}{dt} \frac{\partial \mathcal{L}}{\partial \dot{\mathbf{q}}} - \frac{\partial \mathcal{L}}{\partial \mathbf{q}} = \mathbf{Q} \quad , \quad (7.11)$$

$$\mathbf{q} = \begin{bmatrix} \theta_1 \\ \theta_2 \\ x \end{bmatrix} \quad , \quad \mathbf{Q} = \begin{bmatrix} -b_{p_1,v}\dot{\theta}_1 - \tanh(k_{\tanh}\dot{\theta}_1)b_{p_1,c} \\ -b_{p_2,v}\dot{\theta}_2 - \tanh(k_{\tanh}\dot{\theta}_2)b_{p_2,c} \\ u - b_{c,v}\dot{x} - \tanh(k_{\tanh}\dot{x})b_{c,c} \end{bmatrix} \quad . \quad (7.12)$$

Note that, as in *Part 1*, the control output is seen as the force on the cart directly,  $u = F$ , to avoid excessive notation. Equation 7.11 is computed for each generalized coordinate starting with the first pendulum angle,  $\theta_1$ ,

$$\frac{d}{dt} \frac{\partial \mathcal{L}}{\partial \dot{\theta}_1} - \frac{\partial \mathcal{L}}{\partial \theta_1} = Q_1 \quad (7.13)$$

$$m_1l_1 \sin \theta_1 \dot{\theta}_1 \dot{x} - m_1l_1 \cos \theta_1 \ddot{x} + m_1l_1^2 \ddot{\theta}_1 - m_1l_1 \sin \theta_1 \dot{\theta}_1 \dot{x} - m_1gl_1 \sin \theta_1 = Q_1 \quad (7.14)$$

$$-m_1l_1 \cos \theta_1 \ddot{x} + m_1l_1^2 \ddot{\theta}_1 - m_1gl_1 \sin \theta_1 = -b_{p_1,v}\dot{\theta}_1 - \tanh(k_{\tanh}\dot{\theta}_1)b_{p_1,c} \quad , \quad (7.15)$$

similarly for the second pendulum angle,  $\theta_2$ ,

$$-m_2l_2 \cos \theta_2 \ddot{x} + m_2l_2^2 \ddot{\theta}_2 - m_2gl_2 \sin \theta_2 = -b_{p_2,v}\dot{\theta}_2 - \tanh(k_{\tanh}\dot{\theta}_2)b_{p_2,c} \quad , \quad (7.16)$$

and finally for the cart position,  $x$ ,

$$\frac{d}{dt} \frac{\partial \mathcal{L}}{\partial \dot{x}} - \frac{\partial \mathcal{L}}{\partial x} = Q_3 \quad (7.17)$$

$$\begin{aligned} & (M + m_1 + m_2)\ddot{x} + m_1l_1 \sin \theta_1 \dot{\theta}_1^2 - m_1l_1 \cos \theta_1 \ddot{\theta}_1 + \\ & + m_2l_2 \sin \theta_2 \dot{\theta}_2^2 - m_2l_2 \cos \theta_2 \ddot{\theta}_2 = u - b_{c,v}\dot{x} - \tanh(k_{\tanh}\dot{x})b_{c,c} \quad . \end{aligned} \quad (7.18)$$

The final dynamic equations for the twin pendulum system are then,

$$-m_1 l_1 \cos \theta_1 \ddot{x} + m_1 l_1^2 \ddot{\theta}_1 - m_1 g l_1 \sin \theta_1 = Q_1 \quad (7.19)$$

$$-m_2 l_2 \cos \theta_2 \ddot{x} + m_2 l_2^2 \ddot{\theta}_2 - m_2 g l_2 \sin \theta_2 = Q_2 \quad (7.20)$$

$$(M + m_1 + m_2) \ddot{x} + m_1 l_1 \sin \theta_1 \dot{\theta}_1^2 - m_1 l_1 \cos \theta_1 \ddot{\theta}_1 + m_2 l_2 \sin \theta_2 \dot{\theta}_2^2 - m_2 l_2 \cos \theta_2 \ddot{\theta}_2 = Q_3 \quad (7.21)$$

If one of the angles are fixed in these equations, that is,  $\theta_1$  or  $\theta_2$  and its derivatives are set to zero, then the system reduces to the cart pendulum system from *Part 1* with added mass from the extra pendulum. This added mass appears in the equations as an increase in cart mass, which makes sense as the pendulum is fixed to the cart in this scenario.

As for the cart pendulum system from *Part 1*, by arranging the dynamic equations,

$$\begin{aligned} & \begin{bmatrix} m_1 l_1^2 & 0 & -m_1 l_1 \cos \theta_1 \\ 0 & m_2 l_2^2 & -m_2 l_2 \cos \theta_2 \\ -m_1 l_1 \cos \theta_1 & -m_2 l_2 \cos \theta_2 & M + m_1 + m_2 \end{bmatrix} \begin{bmatrix} \ddot{\theta}_1 \\ \ddot{\theta}_2 \\ \ddot{x} \end{bmatrix} + \begin{bmatrix} 0 \\ 0 \\ m_1 l_1 \sin \theta_1 \dot{\theta}_1^2 + m_2 l_2 \sin \theta_2 \dot{\theta}_2^2 \end{bmatrix} + \\ & + \begin{bmatrix} -b_{p_1,v} \dot{\theta}_1 - \tanh(k_{\tanh} \dot{\theta}_1) b_{p_1,c} \\ -b_{p_2,v} \dot{\theta}_2 - \tanh(k_{\tanh} \dot{\theta}_2) b_{p_2,c} \\ -b_{c,v} \dot{x} - \tanh(k_{\tanh} \dot{x}) b_{c,c} \end{bmatrix} + \begin{bmatrix} -m_1 g l_1 \sin \theta_1 \\ -m_2 g l_2 \sin \theta_2 \\ 0 \end{bmatrix} = \begin{bmatrix} 0 \\ 0 \\ u \end{bmatrix} , \end{aligned} \quad (7.22)$$

the well known general form of an m-link robot is obtained, [13, 14]

$$\mathbf{M}(\mathbf{q}) \ddot{\mathbf{q}} + \mathbf{C}(\mathbf{q}, \dot{\mathbf{q}}) + \mathbf{B}(\dot{\mathbf{q}}) + \mathbf{G}(\mathbf{q}) = \mathbf{F} \quad , \quad (7.23)$$

where,

$\mathbf{M}(\mathbf{q})$  is the inertia matrix

$\mathbf{C}(\mathbf{q}, \dot{\mathbf{q}})$  is the Coriolis and centrifugal effects

$\mathbf{B}(\dot{\mathbf{q}})$  is the friction

$\mathbf{G}(\mathbf{q})$  is the force due to gravity

$\mathbf{F}$  is the input force vector .

Choosing states  $[x_1 \ x_2 \ x_3 \ x_4 \ x_5 \ x_6]^T = [\theta_1 \ \theta_2 \ x \ \dot{\theta}_1 \ \dot{\theta}_2 \ \dot{x}]^T$  results in the nonlinear

state space representation,

$$\begin{bmatrix} \dot{x}_1 \\ \dot{x}_2 \\ \dot{x}_3 \\ \dot{x}_4 \\ \dot{x}_5 \\ \dot{x}_6 \end{bmatrix} = \begin{bmatrix} & & & x_4 & & \\ & & & x_5 & & \\ & & & x_6 & & \\ & & & & & \\ \mathbf{M}^{-1}(x_1, x_2)(\mathbf{F} - \mathbf{C}(x_1, x_2, x_4, x_5) - \mathbf{B}(x_4, x_5, x_6) - \mathbf{G}(x_1, x_2)) & & & & & \end{bmatrix}, \quad (7.24)$$

which is used for simulation of the twin pendulum system.

## 8 | Swing-Up Design

This chapter contains a swing-up design for the twin pendulum system. As for the cart pendulum system in *Part 1* the design is based on [15]. The presented approach is similar to the sat-based energy controller, the final design from *Part 1*. Detailed nonlinear analysis is left out here since this design exploits the same principals as for the final cart pendulum swing-up controller in *Part 1*.

Both pendulums are started in  $\pi$  at rest and the design is based on the pendulum energies in the coordinate system fixed to the cart, thus reducing the generalized coordinates to,

$$\begin{cases} x_{p_1} = -l_1 \sin \theta_1 \\ y_{p_1} = l_1 + l_1 \cos \theta_1 \end{cases} \quad \begin{cases} x_{p_2} = -l_2 \sin \theta_2 \\ y_{p_2} = l_1 + l_2 \cos \theta_2 \end{cases} \quad \begin{cases} \dot{x}_{p_1} = -l_1 \cos \theta_1 \dot{\theta}_1 \\ \dot{y}_{p_1} = -l_1 \sin \theta_1 \dot{\theta}_1 \end{cases} \quad \begin{cases} \dot{x}_{p_2} = -l_2 \cos \theta_2 \dot{\theta}_2 \\ \dot{y}_{p_2} = -l_2 \sin \theta_2 \dot{\theta}_2 \end{cases} . \quad (8.1)$$

Since the energies of the two pendulums are described in a local coordinate system fixed to the cart, there is no cross-coupling, thus the energies are independent of one another,

$$E_{p_1} = m_1 g y_{p_1} + \frac{1}{2} m_1 \dot{x}_{p_1}^2 + \frac{1}{2} m_1 \dot{y}_{p_1}^2 \quad (8.2)$$

$$E_{p_2} = m_2 g y_{p_2} + \frac{1}{2} m_2 \dot{x}_{p_2}^2 + \frac{1}{2} m_2 \dot{y}_{p_2}^2 , \quad (8.3)$$

and in generalized coordinates,

$$E_{p_1} = \frac{1}{2} J_1 \dot{\theta}_1^2 + m_1 g l_1 (\cos \theta_1 + 1) \quad (8.4)$$

$$E_{p_2} = \frac{1}{2} J_2 \dot{\theta}_2^2 + m_2 g (l_2 \cos \theta_2 + l_1) , \quad (8.5)$$

where the inertia  $J_1 = m_1 l_1^2$  and  $J_2 = m_2 l_2^2$  and the energy in equilibrium for each pendulum is,

$$E_{eq_1} = 2m_1 g l_1 , \quad E_{eq_2} = m_2 g (l_1 + l_2) , \quad (8.6)$$

such that,

$$E_{\Delta_1} = E_{p_1} - E_{eq_1} = \frac{1}{2} J_1 \dot{\theta}_1^2 + m_1 g l_1 (\cos \theta_1 - 1) \quad (8.7)$$

$$E_{\Delta_2} = E_{p_2} - E_{eq_2} = \frac{1}{2} J_2 \dot{\theta}_2^2 + m_2 g l_2 (\cos \theta_2 - 1) . \quad (8.8)$$

Choosing the function candidate,

$$V(\theta_1, \theta_2, \dot{\theta}_1, \dot{\theta}_2) = \frac{1}{2} E_{\Delta_1}^2 + \frac{1}{2} E_{\Delta_2}^2 , \quad (8.9)$$

and with the dynamics given by,

$$J\ddot{\theta} = m_1 l_1 \cos \theta_1 a_c + m_1 g l_1 \sin \theta_1 \quad (8.10)$$

$$J\ddot{\theta} = m_2 l_2 \cos \theta_2 a_c + m_2 g l_2 \sin \theta_2 , \quad (8.11)$$

the derivative of  $V$  is evaluated along trajectories of the system,

$$\dot{V} = E_{\Delta_1} \dot{E}_{\Delta_1} + E_{\Delta_2} \dot{E}_{\Delta_2} \quad (8.12)$$

$$\begin{aligned} \dot{V} = & E_{\Delta_1} (J_1 \dot{\theta}_1 \ddot{\theta}_1 - m_1 g l_1 \sin \theta_1 \dot{\theta}_1) \\ & + E_{\Delta_2} (J_2 \dot{\theta}_2 \ddot{\theta}_2 - m_2 g l_2 \sin \theta_2 \dot{\theta}_2) \end{aligned} \quad (8.13)$$

$$\begin{aligned} \dot{V} = & E_{\Delta_1} (\dot{\theta}_1 (m_1 l_1 \cos \theta_1 a_c + m_1 g l_1 \sin \theta_1) - m_1 g l_1 \sin \theta_1 \dot{\theta}_1) \\ & + E_{\Delta_2} (\dot{\theta}_2 (m_2 l_2 \cos \theta_2 a_c + m_2 g l_2 \sin \theta_2) - m_2 g l_2 \sin \theta_2 \dot{\theta}_2) \end{aligned} \quad (8.14)$$

$$\dot{V} = G a_c \quad , \quad (8.15)$$

where,

$$G = m_1 l_1 E_{\Delta_1} \cos \theta_1 \dot{\theta}_1 + m_2 l_2 E_{\Delta_2} \cos \theta_2 \dot{\theta}_2 \quad . \quad (8.16)$$

Following control law for the pivot point acceleration,  $a_c$ , is chosen such that  $\dot{V}$  is negative semi-definite,

$$a_c = \text{sat}(-kG) \quad , \quad (8.17)$$

where  $k$  is a tuning parameter and,

$$\text{sat}(s) = \begin{cases} s & |s| \leq a_{max} \\ \text{sgn}(s) a_{max} & |s| > a_{max} \end{cases} \quad . \quad (8.18)$$

This control law exhibits the same properties as the first design in *Part 1*, thus the largest invariant set also contains the stable equilibrium at  $\pi$ , which is the starting position of the pendulums. For this design, the issue is solved by applying a large current,  $i_{max} = 4.58$  A, for 0.1 s before initiating the swing-up sequence, thus starting at some initial values for which the control signal is different from zero.

The controller for cart position from *Part 1* is used unchanged in this design.

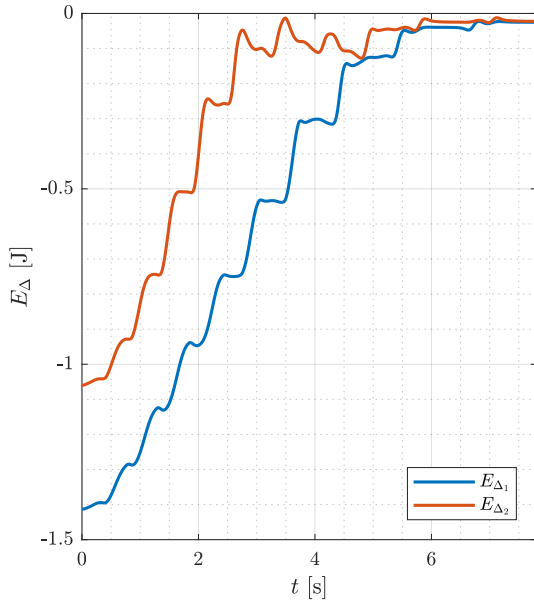


**Figure 8.1:** The mechanical energy for each pendulum approach that of their respective equilibrium points shown here by difference in energy.

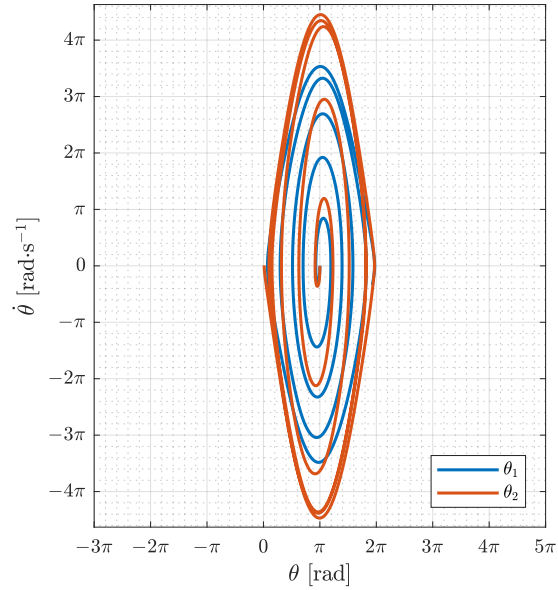


**Figure 8.2:** Both pendulums of the twin system successfully reaches their heteroclinic orbit. Notice how the shorter pendulum (red) reaches higher angular velocity at its orbit than the longer pendulum (blue), which makes sense as the shorter pendulum has a higher frequency.

The design is implemented for simulation, see Figure 8.1 and 8.2, effectively driving the energy differences to zero and reaching a heteroclinic orbit for both pendulums. In these simulations the gain is chosen to  $k = 16$  and  $0.022\text{ J}$  is added to the energy references to reach orbit. In Figure 8.3 and 8.4 it is seen that though the two pendulums reach their heteroclinic orbits, they do not necessarily reach equilibrium simultaneously. However, using a wrapped version of the angles, same as in *Part 1*, it is possible to catch both pendulums while in opposing equilibrium points. Such a scenario is seen most clearly at the end in Figure 8.3 and 8.4 about 11 swings into the simulation.

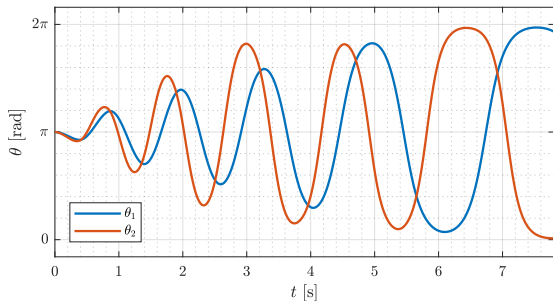


**Figure 8.3:** Due to different lengths of the two pendulums the frequencies are different thus the signals drift compared to one another.

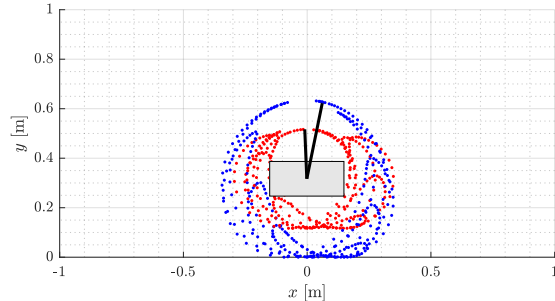


**Figure 8.4:** The two pendulums meet in upright position but at opposing equilibrium points.

The control signal used to obtain the behavior in these simulations are shown in Figure 8.5.

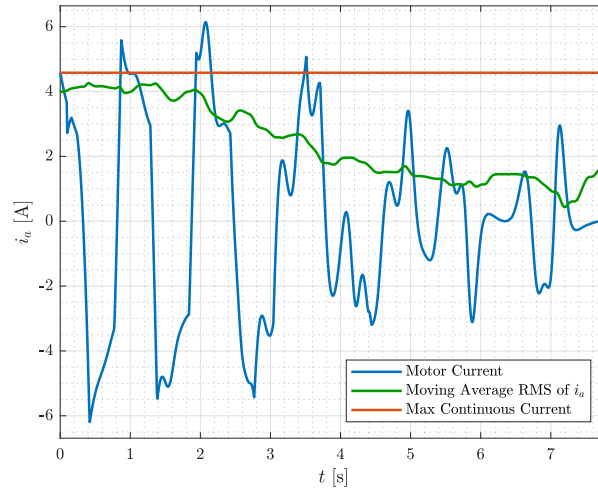


**Figure 8.5:** The control signal required for the twin pendulum swing-up behavior simulated in this chapter is within the limits of the motor.

Figure 8.6 and 8.7 shows that the position control from *Part 1* also works well with the twin pendulum swing-up design.

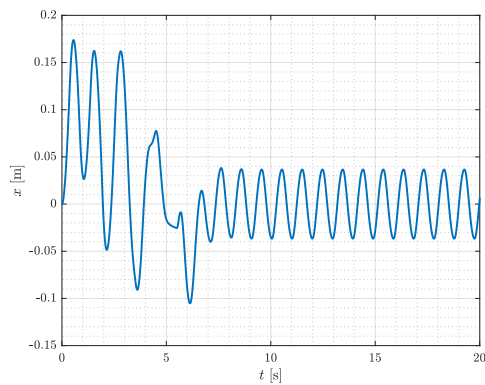


**Figure 8.6:** The position control design used in *Part 1* also shows good results for the twin pendulum.

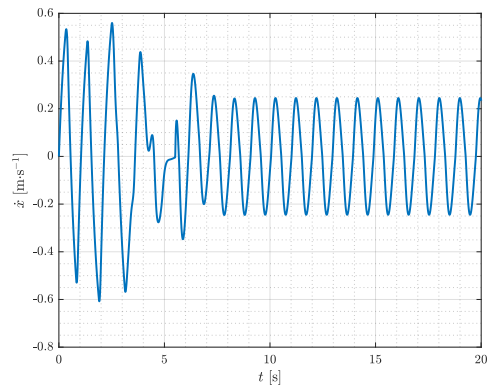


**Figure 8.7:** Both states,  $x$  and  $\dot{x}$ , are successfully brought to around zero while still allowing the swing-up controller to maintain orbit.

This concludes the swing-up design for the twin pendulum. Following is the design of a stabilizing controller in the end of which the swing-up controller is slightly altered to bring the two pendulums in range of the catch controller.

## 9 | Stabilization

In this chapter a Linear Quadratic Regulator (LQR) is designed to stabilize the twin pendulum in upright position taking over from the swing-up controller. The design is based on [18, 19] using the method described in [20].

The nonlinear state space system from Equation 7.24 is linearized,

$$\mathbf{A} = \left. \frac{\partial \mathbf{f}(\mathbf{x})}{\partial \mathbf{x}} \right|_{\substack{\mathbf{x}=\mathbf{0} \\ u=0 \\ k_{\tanh}=1}}, \quad \mathbf{B} = \left. \frac{\partial \mathbf{f}(\mathbf{x})}{\partial u} \right|_{\substack{\mathbf{x}=\mathbf{0} \\ u=0 \\ k_{\tanh}=1}}, \quad (9.1)$$

$$\mathbf{A} = \begin{bmatrix} 0 & 0 & 0 & 1 & 0 & 0 \\ 0 & 0 & 0 & 0 & 1 & 0 \\ 0 & 0 & 0 & 0 & 0 & 1 \\ \frac{g(M+m_1)}{Ml_1} & \frac{gm_2}{Ml_1} & 0 & -\frac{(M+m_1)(b_{p1,c}+b_{p1,v})}{Ml_1^2 m_1} & -\frac{b_{p2,c}+b_{p2,v}}{Ml_1 l_2} & 0 \\ \frac{gm_1}{Ml_2} & \frac{g(M+m_2)}{Ml_2} & 0 & -\frac{b_{p1,c}+b_{p1,v}}{Ml_1 l_2} & -\frac{(M+m_2)(b_{p2,c}+b_{p2,v})}{Ml_2^2 m_2} & 0 \\ \frac{gm_1}{M} & \frac{gm_2}{M} & 0 & -\frac{b_{p1,c}+b_{p1,v}}{Ml_1} & -\frac{b_{p2,c}+b_{p2,v}}{Ml_2} & 0 \end{bmatrix} \quad (9.2)$$

$$\mathbf{B} = \begin{bmatrix} 0 & 0 & 0 & \frac{1}{Ml_1} & \frac{1}{Ml_2} & \frac{1}{M} \end{bmatrix}^T. \quad (9.3)$$

The controllability and observability matrices are computed for the linearized system,

$$\mathbf{C} = \begin{bmatrix} \mathbf{B} & \mathbf{AB} & \mathbf{A}^2\mathbf{B} & \mathbf{A}^3\mathbf{B} & \mathbf{A}^4\mathbf{B} & \mathbf{A}^5\mathbf{B} \end{bmatrix} \Rightarrow \text{rank}(\mathbf{C}) = 6 \quad (9.4)$$

$$\mathbf{O} = \begin{bmatrix} \mathbf{C} \\ \mathbf{CA} \\ \mathbf{CA}^2 \\ \mathbf{CA}^3 \\ \mathbf{CA}^4 \\ \mathbf{CA}^5 \end{bmatrix} \Rightarrow \text{rank}(\mathbf{O}) = 6, \quad (9.5)$$

and since  $\mathbf{C}$  and  $\mathbf{O}$  both have full rank, the system is controllable and observable. It is interesting to note that if friction is set to zero and both pendulums are given same length, then  $\mathbf{C}$  loses rank, that is, the system would no longer be controllable. This is true even if the pendulum masses are different.

Designing the LQR amounts to minimizing the cost function,

$$\mathcal{J} = \int_0^{\infty} \mathbf{x}^T \mathbf{Q} \mathbf{x} + \mathbf{u}^T \mathbf{R} \mathbf{u} dt \quad . \quad (9.6)$$

where  $\mathbf{Q}$  and  $\mathbf{R}$  are weighing matrices for the states and input respectively. In this case Bryson's rule is used for tuning  $\mathbf{Q}$  and  $\mathbf{R}$  such that,

$$Q_{ii} = \frac{1}{x_{i,max}^2} \quad , \quad R_{ii} = \frac{1}{u_{i,max}^2} \quad , \quad (9.7)$$

where  $x_{i,max}$  are the maximum state errors and  $u_{i,max}$  are the maximum inputs.

The gain vector,  $\mathbf{F}$ , is given by,

$$\mathbf{F} = -\mathbf{R}^{-1} \mathbf{B}^T \mathbf{P} \quad , \quad (9.8)$$

where  $\mathbf{P}$  is the state-transfer matrix and can be found by solving the Algebraic Riccati equation,

$$\mathbf{A}^T \mathbf{P} + \mathbf{P} \mathbf{A} - \mathbf{P} \mathbf{B} \mathbf{R}^{-1} \mathbf{B}^T \mathbf{P} + \mathbf{Q} = \mathbf{0} \quad . \quad (9.9)$$

In this case there is only one input  $u$  so  $R$  is scalar. The tuned  $\mathbf{Q}$  and  $R$  are given by,

$$\mathbf{Q} = \text{diag}(1, 1, \frac{1}{0.01^2}, 1, 1, 1) \quad , \quad R = \frac{1}{3.3357^2} \quad , \quad (9.10)$$

resulting in the state feedback gain,

$$\mathbf{F} = [ -5058.01 \quad 4037.40 \quad 296.63 \quad -892.48 \quad 553.70 \quad 256.29 ] \quad . \quad (9.11)$$

During implementation it is found that the controller struggles to drive the cart position,  $x$ , to zero. This is the reason why  $x$  is the only punished state in Equation 9.10. The issue is further discussed in *Results* chapter 11. A simulation of the control design is seen in Figure 9.1 and 9.2.

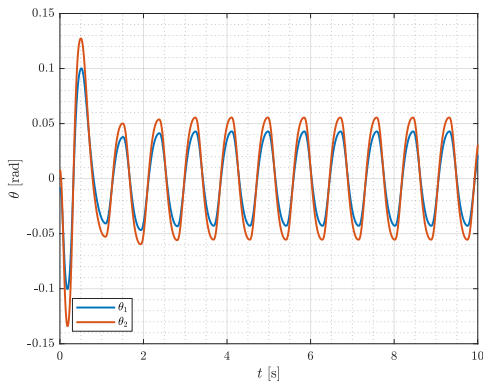


**Figure 9.1:** A simulation of the LQR design stabilizing the two pendulums around zero with oscillations.

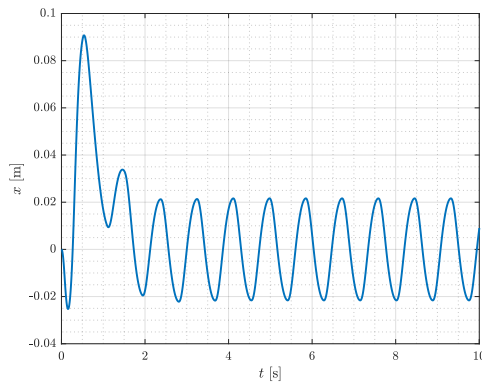


**Figure 9.2:** The cart position initially moves away from zero but returns to stabilize with some oscillations.

The required armature current for the LQR design is shown in Figure 9.3, where the RMS current stays within the motor's maximum continuous current limit.

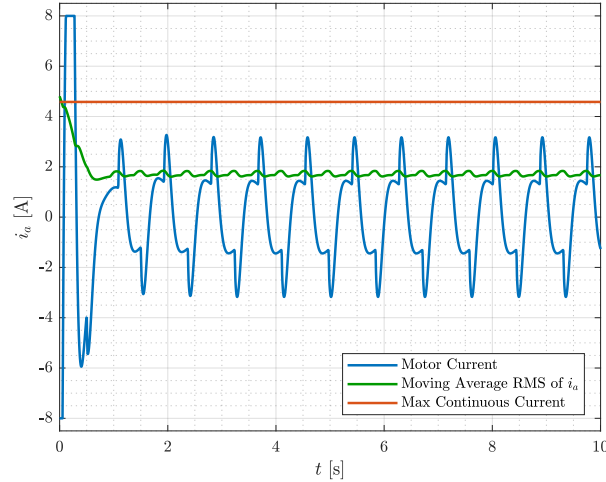


**Figure 9.3:** The control signal required by the LQR design is considered reasonable with only short pulses exceeding the maximum continuous current rating of the motor.

With both the swing-up and stabilizing controller designed for the twin pendulum system, it is, in simulation, attempted to swing up and then catch both pendulums in upright position.

The swing-up controller bringing the pendulum energy errors to zero ensures convergence to the heteroclinic orbit of each pendulum. However, it does not promise timing such that both pendulums reach the equilibrium simultaneously. For this reason it is found necessary to split the tuning gain  $k$  such that the new control law becomes,

$$G = k_1 m_1 l_1 E_{\Delta_1} \cos \theta_1 \dot{\theta}_1 + k_2 m_2 l_2 E_{\Delta_2} \cos \theta_2 \dot{\theta}_2 \quad (9.12)$$

$$a_c = \text{sat}(-G) \quad . \quad (9.13)$$

It is further found useful to tune the energy reference of each pendulum separately. In the following simulations, see Figure 9.4 and 9.5, the energy reference of the first pendulum,  $E_{\Delta_1}$ , is increased by 0.030 J and for the second pendulum  $E_{\Delta_2}$  is increased by 0.028 J. The gains are tuned to  $k_1 = 25$  and  $k_2 = 17$ .

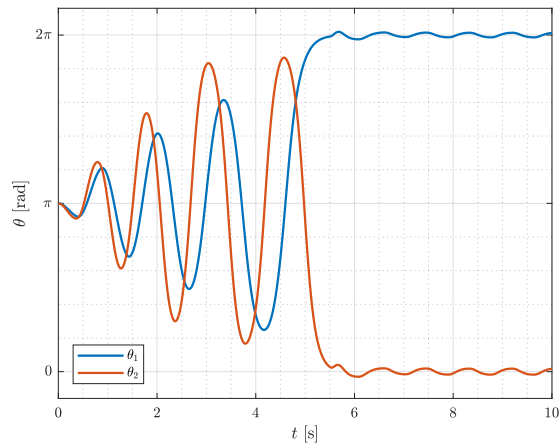


**Figure 9.4:** A simulation of the twin pendulum using the energy based swing-up controller and catching with the LQR.

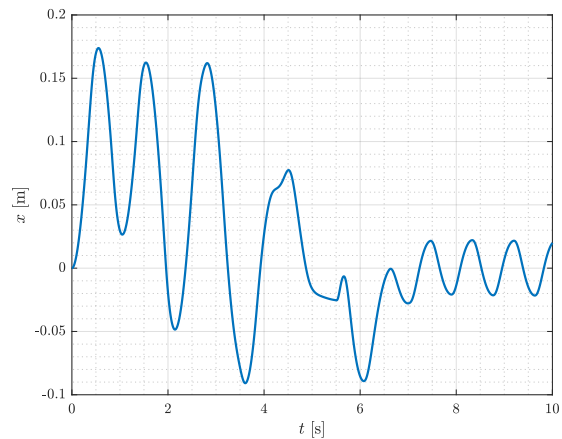


**Figure 9.5:** The  $x$  position controller keeps the cart away from the rail edge while the swing-up controller approaches equilibrium.

The control signal used to obtain the result in Figure 9.4 and 9.5 is shown in Figure 9.6.

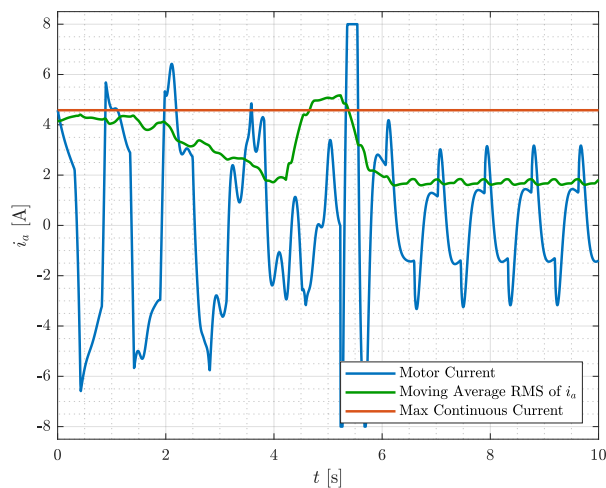


**Figure 9.6:** The needed armature current for the simulated behavior of swing-up and catch.

The energy control strategy from *Part 1* was successfully adapted as a swing-up controller for twin pendulum system. Further the swing-up controller was tuned to bring both pendulums into equilibrium at the same time for the LQR controller to catch both pendulums in simulation.

To implement the control strategies, the next chapter is concerned with estimating the three unmeasured states of the twin pendulum system.

# 10 | State Estimation

There are three measurable states in the twin pendulum system, the pendulum angles,  $\theta_1$  and  $\theta_2$ , and the position of the cart,  $x$ . The remaining three states, the pendulum velocities,  $\dot{\theta}_1$  and  $\dot{\theta}_2$ , and the cart velocity,  $\dot{x}$ , must be estimated. In this chapter a Kalman filter is designed based on [21, 22].

The pendulum angles are measured with a resolution of  $\Delta_\theta = \pi \times 10^{-3}$  rad/tic and the cart position with a resolution of  $\Delta_x = 0.088 \times 10^{-3}$  m/tic. This causes the quantization problem illustrated for  $\theta_1$  in Figure 10.1. This is less of an issue for  $x$  since its measurement resolution is two orders of magnitude higher than that of the angles.

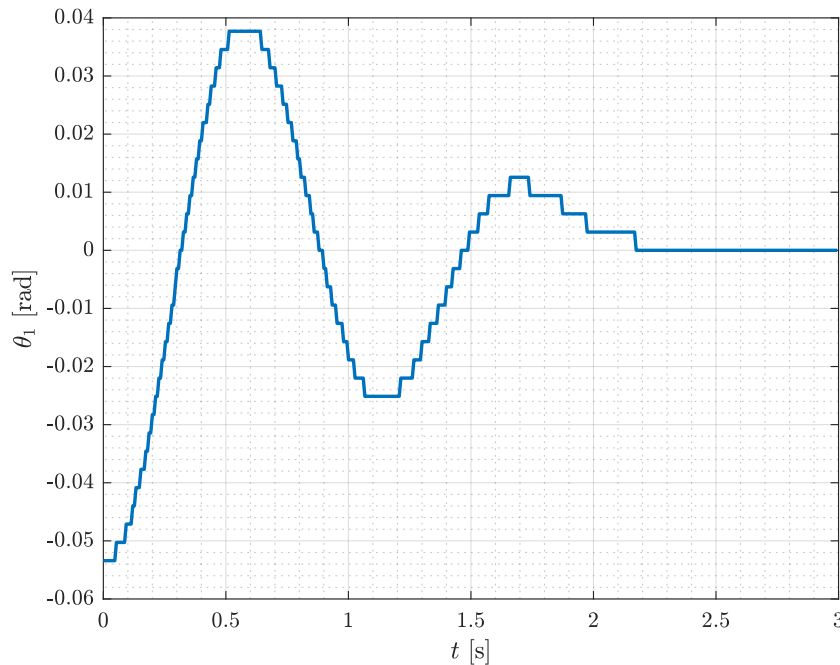


**Figure 10.1:** Angle measurement of the first pendulum shows how the quantization is more significant than any potential underlying noise.

To estimate the three unmeasured states and solve the quantization problem a Kalman filter is designed. In the design process it is useful to have a simulation exhibiting the same issues as the real system. To that end a simple quantization model, [23, p. 35], is proposed,

$$x_q = \Delta \left\lfloor \frac{x}{\Delta} + \frac{1}{2} \right\rfloor, \quad (10.1)$$

where  $x_q$  is the quantized state,  $x$  is the un-quantized simulated state and  $\Delta$  is the measurement resolution of said state. To see if the model behaves like the real measurements, the original signal from Figure 10.1 is smoothed and then quantized using Equation 10.1. The result is seen in Figure 10.2 where the modeled quantization of the smoothed signal approaches the original measured signal.

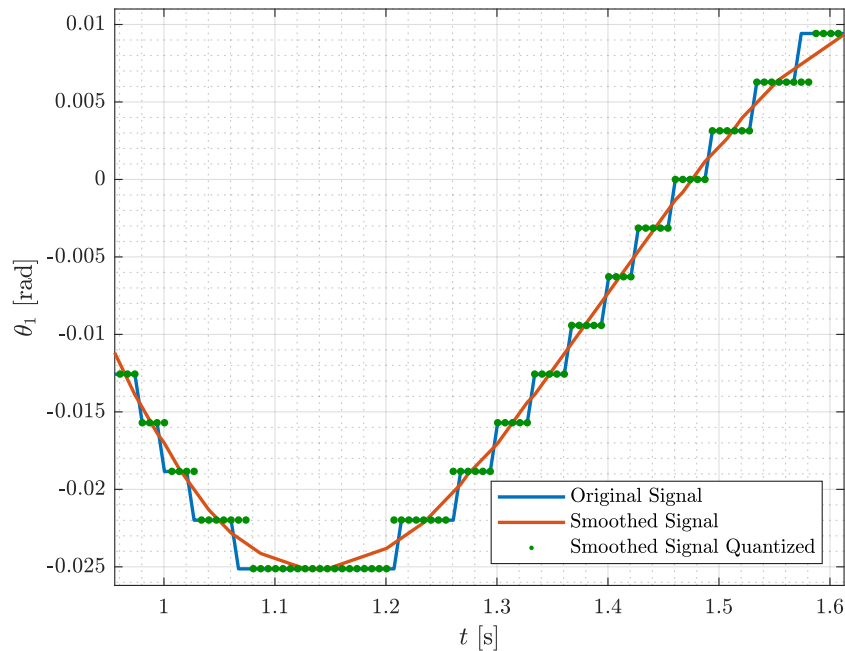


**Figure 10.2:** The original measured signal (blue) is smoothed (red) and the smoothed signal is then quantized (green) using the model from Equation 10.1. This is used as a way to simulate measurements in the Kalman filter design process.

In this manner it is possible to simulate the system obtaining true values for all six states along with a quantized version for the Kalman filter.

The Kalman filter is designed using the following discrete linear model,

$$\mathbf{x}_k = \mathbf{F}\mathbf{x}_{k-1} + \mathbf{G}u_{k-1} + \mathbf{w}_{k-1} \quad , \quad \mathbf{w} \sim \mathcal{N}(0, \mathbf{Q}) \quad (10.2)$$

$$\mathbf{y}_k = \mathbf{H}\mathbf{x}_k + \mathbf{v}_k \quad , \quad \mathbf{v} \sim \mathcal{N}(0, \mathbf{R}) \quad , \quad (10.3)$$

where,

- $\mathbf{x}$  is the states  $\mathbf{F}$  is the system matrix
- $u$  is the input  $\mathbf{G}$  is the input matrix
- $\mathbf{y}$  is the measurements  $\mathbf{H}$  is the output matrix
- $\mathbf{w}$  is the process noise drawn from a normal distribution with covariance  $\mathbf{Q}$
- $\mathbf{v}$  is the measurement noise drawn from a normal distribution with covariance  $\mathbf{R}$  .

In the following the Kalman filter algorithm is presented in three steps.

### Initialization

The previous predicted state vector,  $\hat{\mathbf{x}}_{k-1}$ , is initialized to the current measurements,  $y_k$ ,

$$\hat{\mathbf{x}}_{k-1} = y_k \quad , \quad (10.4)$$

and the previous state error covariance  $\mathbf{P}_{k-1}$  is initialized to some initial guess  $\mathbf{P}_0$  here set to the identity matrix,

$$\mathbf{P}_{k-1} = \mathbf{P}_0 \quad . \quad (10.5)$$

When the Kalman filter is running  $\mathbf{P}$  will converge to some steady state values which is then used as  $\mathbf{P}_0$  in the implementation for faster convergence.

### Prediction

A prediction of the states is calculated using the discrete system model,

$$\hat{\mathbf{x}}_{k|k-1} = \mathbf{F}\hat{\mathbf{x}}_{k-1} + \mathbf{G}u_{k-1} \quad , \quad (10.6)$$

where  $\hat{\mathbf{x}}_{k|k-1}$  is the predicted states at time  $k$  using previous estimate and input. Note that  $k|k-1$  reads “ $k$  given  $k-1$ ”. Similarly a prediction of the state error covariance matrix is computed,

$$\mathbf{P}_{k|k-1} = \mathbf{F}\mathbf{P}_{k-1}\mathbf{F}^T + \mathbf{Q} \quad , \quad (10.7)$$

using the previous state error covariance matrix,  $\mathbf{P}_{k-1}$ , with state dynamics,  $\mathbf{F}$ , and the process noise covariance,  $\mathbf{Q}$ .

### Update

The predicted state error covariance matrix,  $\mathbf{P}_{k|k-1}$ , is then used along with the output matrix,  $\mathbf{H}$ , and the measurement noise error covariance,  $\mathbf{R}$ , to compute the Kalman gain,

$$\mathbf{K}_k = \mathbf{P}_{k|k-1}\mathbf{H}^T(\mathbf{H}\mathbf{P}_{k|k-1}\mathbf{H}^T + \mathbf{R})^{-1} \quad . \quad (10.8)$$

Finally the estimated states are updated using the previous estimated states,  $\hat{\mathbf{x}}_{k-1}$ , the Kalman gain,  $\mathbf{K}_k$ , and the difference between measured output,  $y_k$ , and predicted output,

$$\hat{\mathbf{x}}_k = \hat{\mathbf{x}}_{k-1} + \mathbf{K}_k(y_k - \mathbf{H}\hat{\mathbf{x}}_{k-1}) \quad , \quad (10.9)$$

where  $\mathbf{H}\hat{\mathbf{x}}_{k-1} = \hat{y}_{k-1}$  is the predicted output. The state error covariance matrix is also updated,

$$\mathbf{P}_k = (\mathbf{I} - \mathbf{K}_k\mathbf{H})\mathbf{P}_{k|k-1} \quad , \quad (10.10)$$

where  $\mathbf{I}$  is the identity matrix.

The measurement noise covariance is tuned such that the quantization problem is solved without causing divergence from the trend of the data, see Figure 10.3,

$$\mathbf{R} = \text{diag}(100, 100, 10) \quad . \quad (10.11)$$

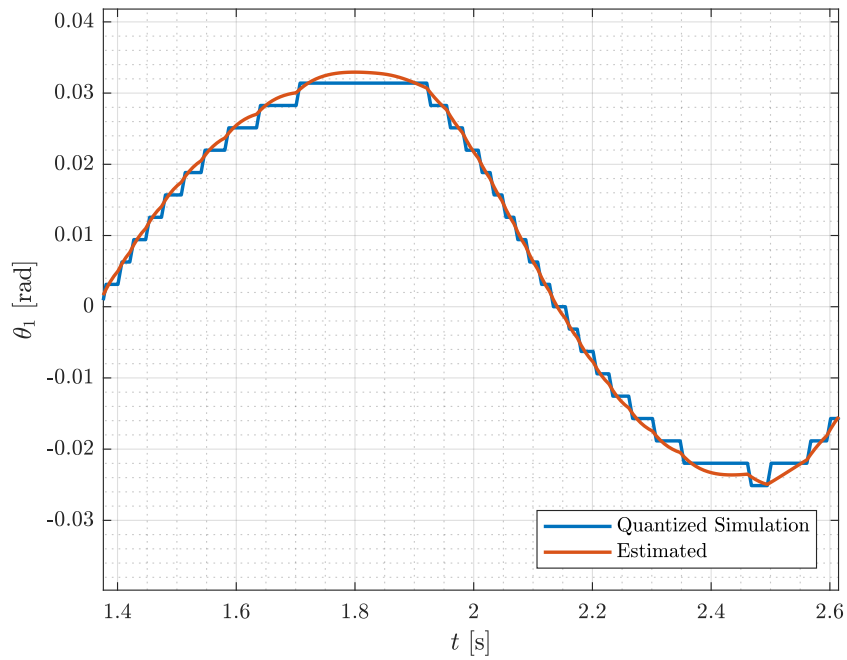


**Figure 10.3:** The Kalman filter successfully overcomes the quantization problem in simulation. A similar result is obtained for  $\theta_2$ .

The process noise covariance matrix is tuned to get as true estimations of the derivatives as possible while maintaining low noise levels, see simulation in Figure 10.4,

$$\mathbf{Q} = \text{diag}(1, 1, 1, 100, 100, 10) \quad , \quad (10.12)$$

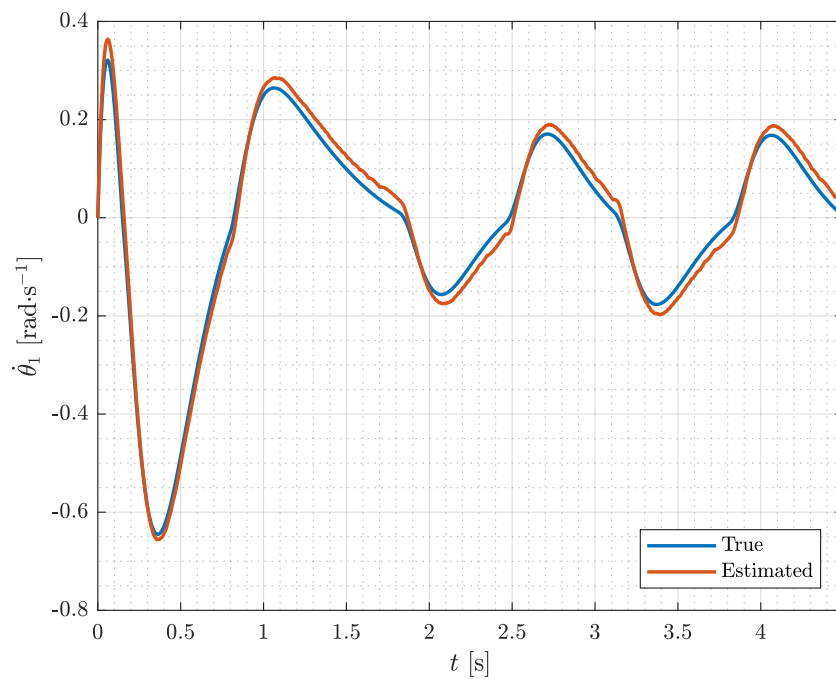


**Figure 10.4:** Simulation of LQR controller used for tuning the Kalman filter to get a good estimation of the state derivatives. A similar result is obtained for  $\theta_2$ .

Since the quantization problem is less significant for the position measurements compared to the angle measurements, the filter obtains near perfect results in simulation, see Figure 10.5 and 10.6.

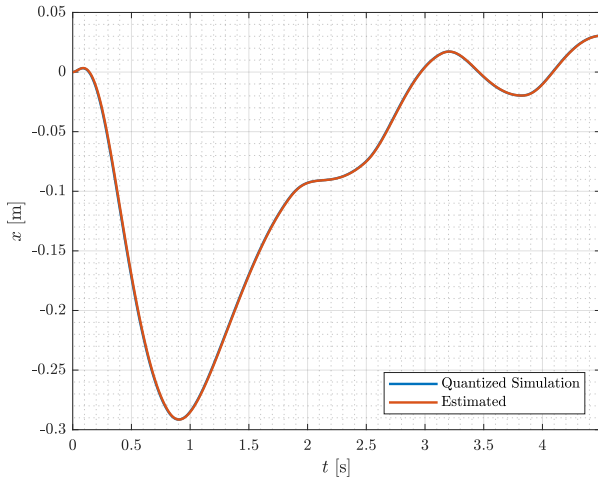


**Figure 10.5:** The quantization of  $x$  is so insignificant that it does not show on the plot.

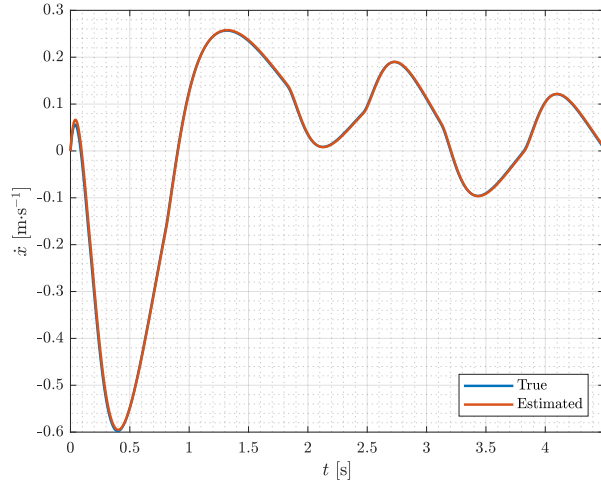


**Figure 10.6:** Given the good position measurements, the Kalman filter successfully estimates the cart velocity.

This concludes state estimation for the twin pendulum system. With all parameters estimated and the Kalman filter designed for state estimation any remaining comments on implementation are addressed when presenting the results in the next chapter.

# 11 | Results

The swing-up controller, LQR and the Kalman filter for the twin pendulum are implemented on the system and the results presented here. The swing-up controller approaches equilibrium for both pendulums, see Figure 11.1. However, when tuning the gain of one pendulum the behavior of the other pendulum is affected.

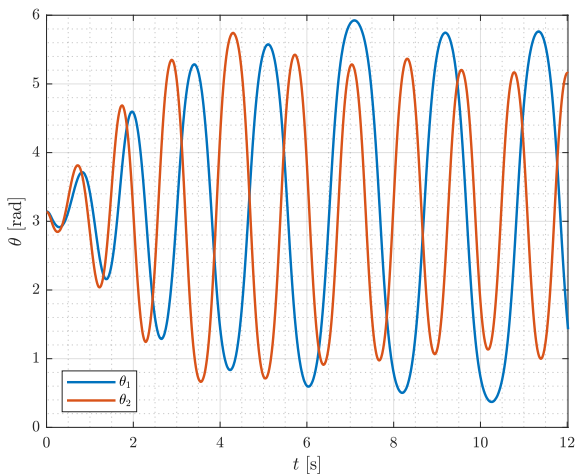


**Figure 11.1:** Swing-up controller attempting to approach equilibrium for both pendulums.

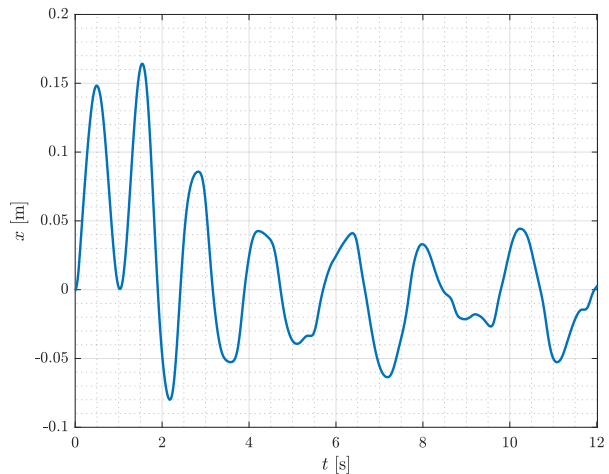


**Figure 11.2:** The position controller keeps the cart within the operating range.

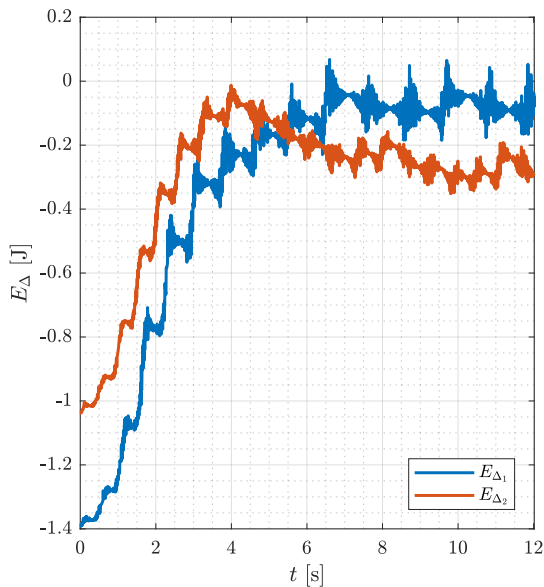


**Figure 11.3:** The energy error of each pendulum. As the first pendulum catches up the second pendulum loses energy.

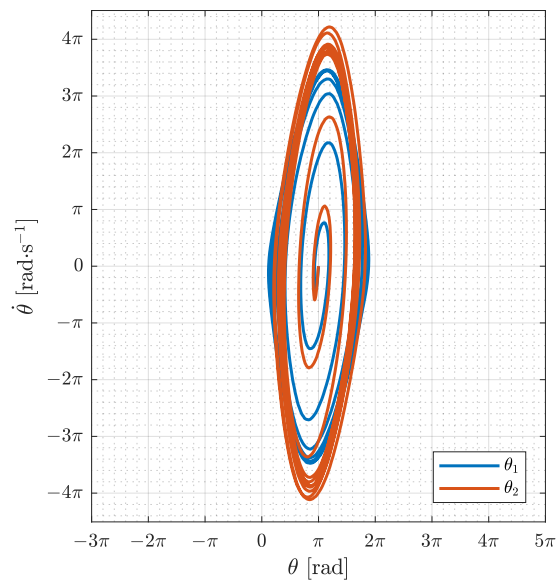


**Figure 11.4:** The phase portrait is not symmetrical consistently hitting high velocity after passing  $\pi$ , downward position.

This makes it difficult to find the right balance to let both pendulums reach equilibrium at the same time. It is only made more difficult by the position control further adding disturbance to the swing-up controller. Figure 11.2 shows the position controller successfully keeping the cart in away from the edges of the rail. In Figure 11.3 the second pendulum first reaches for zero energy error reference, however, as the energy of the first pendulum increases, the second pendulum loses energy. As known from simulations in the design, with more time it should be possible to tune the gains against each other until a balance is achieved and both pendulums approach zero energy error. In Figure 11.4 the phase portrait is slightly skewed compared to simulation, showing peak velocity after passing  $\pi$ , the reason is unknown.

A test of the implemented LQR is seen in Figure 11.5 where both pendulums are started in zero. The controller does keep both pendulums around zero, however with a lot of oscillations.

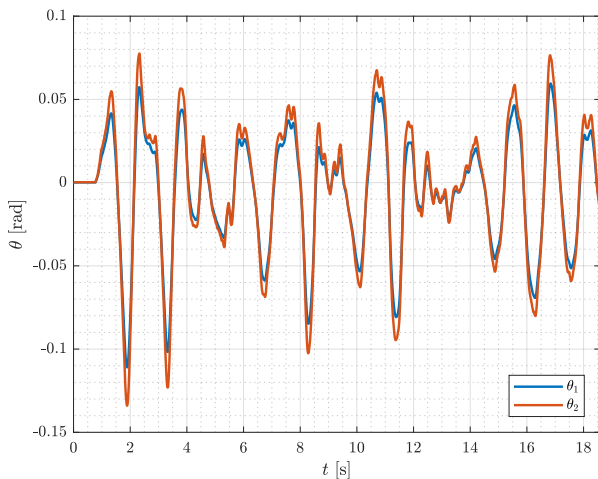


**Figure 11.5:** The LQR successfully keeps both pendulums in upright position.

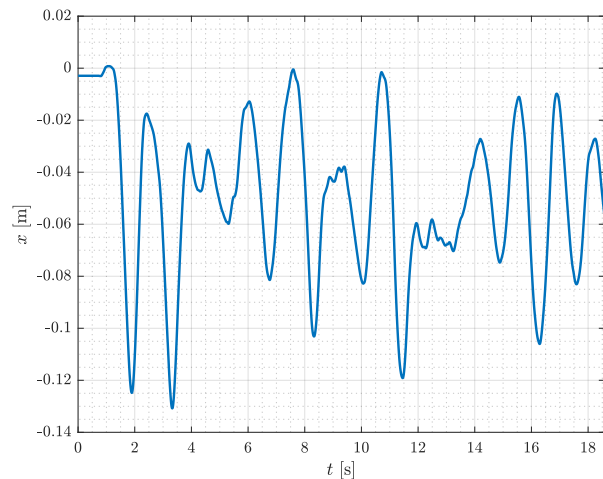


**Figure 11.6:** In this test the cart position is kept close to center.

During test of the LQR design a problem of keeping the cart around zero on the rail was encountered. In Figure 11.6 the controller does rather well compared to other tests. When initializing the system for each test all three encoders must be reset such that zero position is known. Originally the pendulums were reset when hanging downward and initialized to  $\pi$ . It was found that initializing the pendulums in upright position caused the LQR controller to converge to different parts of the rail, while with the other approach the cart consistently stayed on the right side of the rail. From this it is thought that small errors in initialized angle away from true vertical position is enough to cause an imbalance in the feedback driving the cart to one side until the position error becomes large enough to counter the angle error. On these grounds the result seen here are from a test with more fortunate initialization of the pendulum angles.

The control signal cooresponding to this LQR test is seen in Figure 11.7.

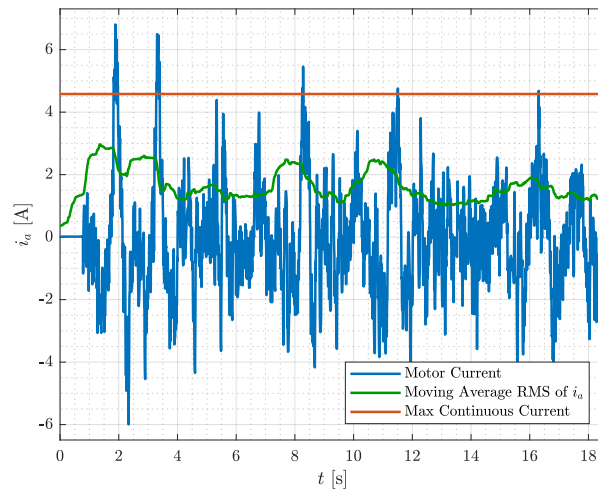


**Figure 11.7:** The control signal used to achieve the results in Figure 11.5 and 11.6.

In Figure 11.8 the swing-up controller is tuned to  $k1 = 9.5$ ,  $k2 = 2.77$  and the energy reference of the first pendulum,  $E_{\Delta_1}$ , is increased by 0.175 J while for the second pendulum  $E_{\Delta_2}$  is increased by 0.020 J. The result starts to look more like the simulations, however, in this case the first pendulum overshoots before the second pendulum reaches equilibrium. It is not known whether the LQR will be able to catch the twin pendulum even with further tuning. However, this swing-up design shows promise, that with more tuning and perhaps deploying a nonlinear control strategy for the stabilizing controller, eventually catching the twin pendulum on the given setup should be possible.

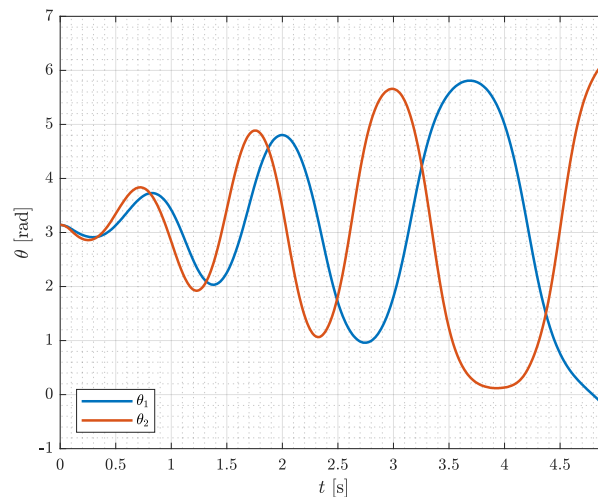


**Figure 11.8:** The swing-up controller is tuned showing promise that catching the twin pendulum on the real system should be possible with more tuning and possibly a nonlinear control strategy for the stabilizing controller.

In the phase plot, see Figure 11.9, it is seen that the pendulums do not reach zero velocity when approaching equilibrium. The control signal used to swing up the pendulums is seen

in Figure 11.10, as in simulation a high but short pulse is given in the beginning of the test to start the swing-up controller.

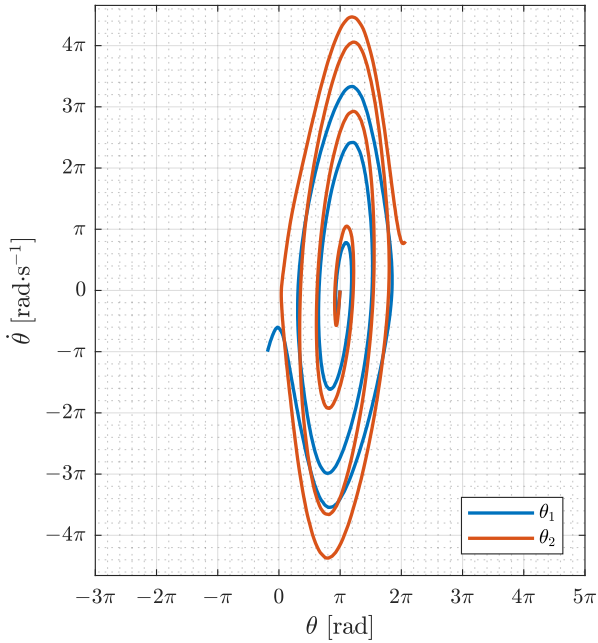


**Figure 11.9:** The phase plot shows how both pendulums approach equilibrium with relatively high velocities.

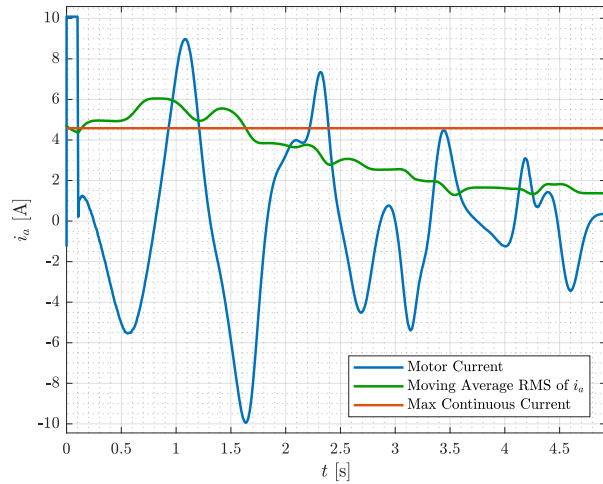


**Figure 11.10:** The armature current is a quite high, but does not sustain high current.

The Kalman filter is implemented in c-code. The quantization problem is solved same as in simulation, see Figure 11.11 and 11.12 where the measurements are smoothed. The test of the Kalman filter is run with the LQR to keep the system around zero where the linear estimator is meant to operate.

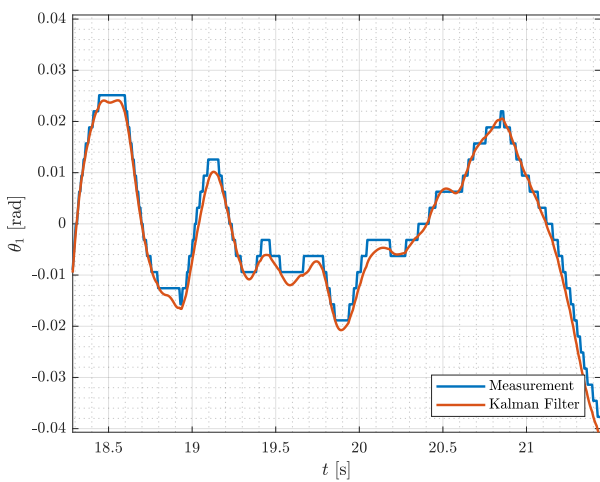


**Figure 11.11:** The quantization from measurement resolution is overcome by use of the Kalman filter.

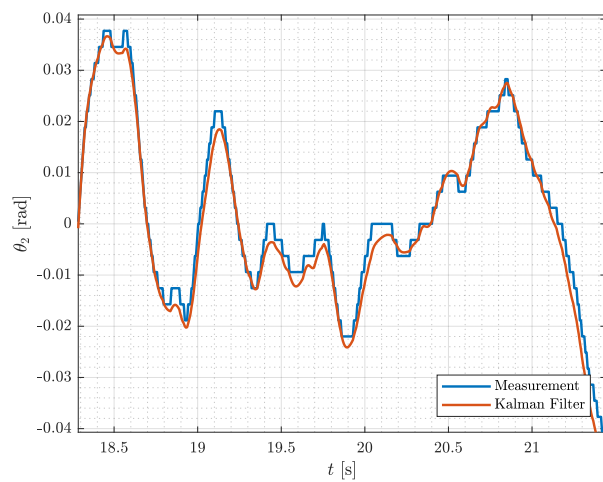


**Figure 11.12:** The Kalman filter shows good results for both pendulums.

In Figure 11.13 and 11.14 the Kalman filter successfully estimates the angel derivatives. An MA filter with a window size of 10 is used for comparison, notice how the MA filter is delayed compared to the Kalman filter.

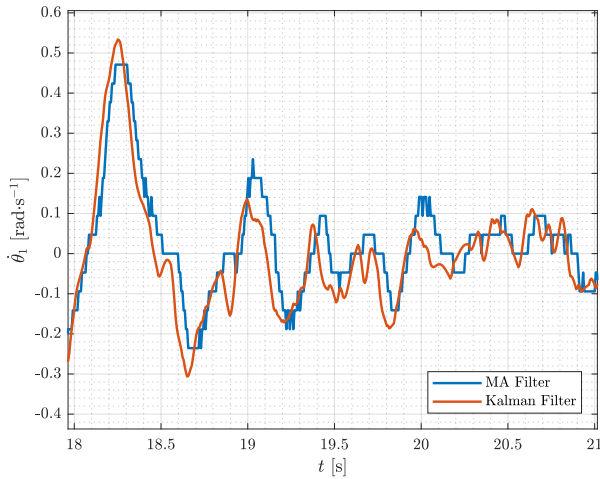


**Figure 11.13:** The angular velocity of the first pendulum estimated by the Kalman filter.

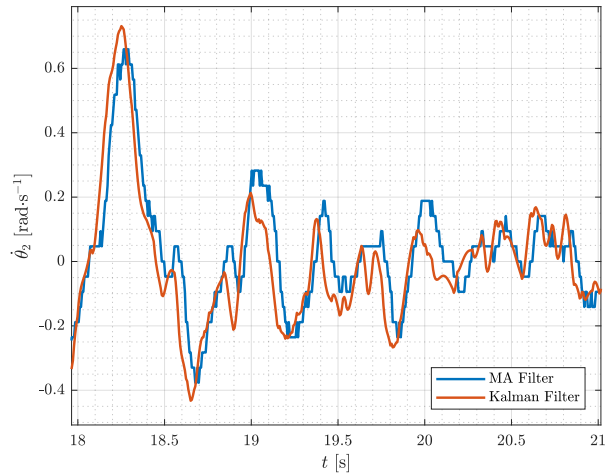


**Figure 11.14:** The velocity of the second pendulum shows similar results.

With higher resolution on the cart position the Kalman filter shows better results and no MA filter is needed to show the trend of the derivative, see Figure 11.15 and 11.16.

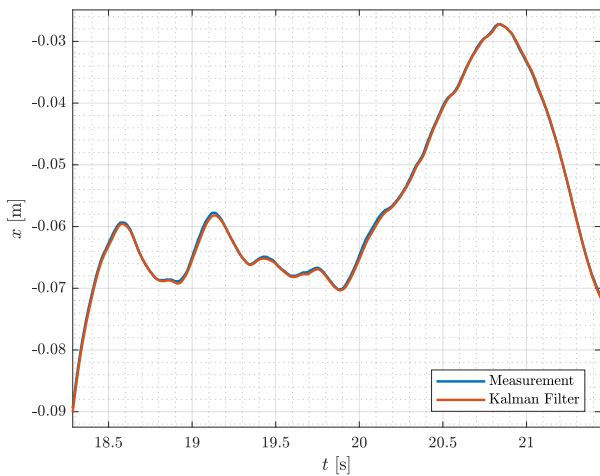


**Figure 11.15:** Almost no quantization noise causes no need for smoothing by the Kalman filter.

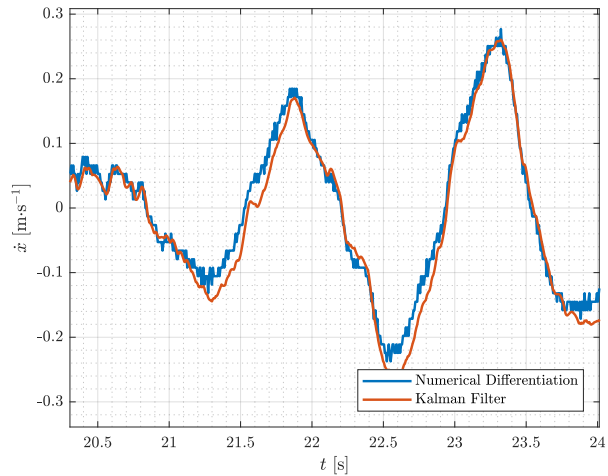


**Figure 11.16:** The estimated cart velocity leaves no noise and follows the trend of the numerical differentiation.

A swing-up controller based on the principles from *Part 1* was designed and successfully tested in simulation. Further, an LQR was designed to stabilize the system in zero. The stabilizing controller was in simulation capable of catching the twin pendulum after the swing-up sequence. A Kalman filter was designed and implemented to remove quantization noise from the measurements and estimate the three derivative states. Both control

designs were implemented on the twin pendulum system and works separately to some degree. Catching the twin pendulum after swing-up was attempted but not successful. It is thought that further tuning of the swing-up controller and possibly a nonlinear control design for the stabilizing controller could solve this issue. This concludes *Part 2* of this thesis.

## 12 | Conclusion

In *Part 1* of this thesis the cart pendulum system was investigated. A test setup provided in the Control and Automation Lab by AAU was used as a platform for implementation and test of the control strategies developed.

The objective was to swing up the pendulum from downward position, then catch and stabilize it in upright position. To achieve this behavior on an underactuated nonlinear system, two control strategies were implemented in the final design.

A model of the cart pendulum system was put forth and a simulation was developed to use during the design.

In the process three energy based swing-up controllers were designed and tested in simulation. Though inefficient, the first controller was the simplest form of the idea and therefore useful in understanding the underlying principals of the energy based control strategies. For that reason, this is also where the nonlinear analysis of the energy based swing-up controller was investigated. It showed that, by Lasalle's Theorem, deploying this control strategy, the pendulum would converge to the set connecting two equilibrium points, thus eventually reaching heteroclinic orbit.

The second swing-up controller was a sign-based controller with the same underlying logic as the first design, but using a sign function to give maximum control output in the desired direction. While the controller worked in simulation, the sign-function caused excessive switching making it undesirable for implementation.

Though the sign-based controller could not be implemented, it showed an ideal swing-up behavior. This made the basis for the final sat-based controller in which most of the performance of the sign-based controller was maintained while eliminating the switching issue.

All three swing-up controllers caused the cart in simulation to drift off the physical limitations of the rail. To solve this issue a simple linear state feedback controller was designed and successfully kept the cart position around zero, the middle of the rail.

To catch the pendulum in upright position after the swing-up procedure, a sliding mode controller was developed. This involved a system transformation, linear state feedback stabilization of the reduced order model in the transformation and finally a sliding surface based in the Lyapunov Stability Theorem.

In the implementation of these controllers it was necessary to estimate frictions in the system and mass of the cart. The friction between cart and rail proved challenging to model, and after analyzing the result of 68 tests along the rail, it was found that the friction depends on both position and direction of the cart. To manage this friction a lookup table was implemented with online interpolation between points to estimate and finally compensate for the cart friction along the rail. This friction compensation showed good results, but is not considered a perfect map or model of the cart friction.

To obtain estimates of the unmeasured states an extended Kalman filter (provided by a

previous project group) was used for stabilization and a moving average filter was designed and implemented for the swing-up controller.

With all parameters accounted for the sliding mode and sat-based swing-up controller were successfully implemented and tested on the cart pendulum setup. The cart did on occasion diverge from zero before returning and re-stabilizing. It is thought to be an issue caused by imperfect friction compensation and possibly amplified by the extended Kalman filter not receiving likely dynamical behavior from the system based on the given input.

**In *Part 2*** an additional pendulum was mounted on the test setup from *Part 1*, making it a twin pendulum system. This adds the challenge by a second unactuated link in the system.

The objective was to use the knowledge and experience gained in *Part 1* to develop a strategy for swinging up and catching both pendulums in upright position.

A model was developed and implemented for simulation of the twin pendulum system and the new friction parameters for the second pendulum were estimated.

The design of the twin swing-up controller was based on the same principals as for the sat-based energy controller for the cart pendulum system and showed good results in simulation.

To stabilize and eventually catch the two pendulums and LQR was designed. The swing-up controller and LQR were successfully simulated together.

Since an other two states were added to the system by the new pendulum a new state estimator was needed. Thus, a Kalman filter was designed, tuned and successfully implemented to smooth measurement quantization and estimate the three derivative states.

Finally the swing-up and LQR controller were implemented on the twin pendulum system. The swing-up design shows good results, however further tuning is needed to bring the pendulums to equilibrium simultaneously for the catch controller to take over. Though exhibiting a lot of oscillations, the LQR successfully stabilized the two pendulums in upright position.

**Future Work:** It would be interesting to see further attempts at estimating the cart friction. One could combine a position and direction dependent friction model with machine learning. The machine learning algorithm could then adjust and learn the rail friction given random control inputs until the model error is brought close to zero.

Further tuning of the swing-up controller combined with a sliding mode design for the twin pendulum system is a clear next step. Developing an extended Kalman filter for the twin pendulum system would also be interesting to see.

# Bibliography

- [1] Russ Tedrake. *Underactuated robotics: Learning, planning, and control for efficient and agile machines course notes for MIT 6.832*. Version Working draft edition. 2009. URL: <http://citeseerx.ist.psu.edu/viewdoc/download?doi=10.1.1.396.3212&rep=rep1&type=pdf>.
- [2] Maxon RE Motor. Oct. 8, 2018. URL: [https://www.maxonmotor.com/medias/sys\\_master/root/8825409470494/17-EN-133.pdf](https://www.maxonmotor.com/medias/sys_master/root/8825409470494/17-EN-133.pdf).
- [3] Avago Technologies. *HEDM-55xx/560x & HEDS-55xx/56xx*. Aug. 15, 2018. URL: [https://www.infineon.com/dgdl/Infineon-Encoder\\_HEDS-5540-A14-AP-v01\\_00-EN.pdf?fileId=5546d46147a9c2e40147d3d593970357](https://www.infineon.com/dgdl/Infineon-Encoder_HEDS-5540-A14-AP-v01_00-EN.pdf?fileId=5546d46147a9c2e40147d3d593970357).
- [4] Maxon Controller. Aug. 15, 2018. URL: <https://www.maxonmotor.com/maxon/view/product/control/Servoverstaerker-4-Q-DC/201583>.
- [5] *sparkfun Teensy 3.6*. Aug. 15, 2018. URL: <https://www.sparkfun.com/products/14057>.
- [6] *HCTL-2021 PLC Avago Datasheet*. Aug. 15, 2018. URL: <https://datasheet.octopart.com/HCTL-2021-PLC-Avago-datasheet-7580518.pdf>.
- [7] *K66 Sub-Family Reference Manual*. Aug. 15, 2018. URL: <https://cdn.sparkfun.com/datasheets/Dev/Arduino/Boards/K66P144M180SF5RMV2.pdf>.
- [8] Jonas Ørndrup Jesper H. Hørgensen. *Non-linear Control and Machine Learning on an Inverted Pendulum on a Cart*. Master Thesis. 2018.
- [9] Niels Skov Vestergaard. *Sliding Mode Stabilization and Phase Plane Trajectory Planning for a Cart Pendulum System*. 9<sup>th</sup> Semester Project. 2018.
- [10] Rafael Wisniewski. *Mechanical Systems II. Lagrange Mechanics*. Aalborg University, 2013.
- [11] Charles M. Close, Dean K. Frederick, and Jonathan C. Newell. *Modeling and Analysis of Dynamic Systems*. Wiley, 2001.
- [12] H. Olsson et al. *Friction Models and Friction Compensation*. Nov. 28, 1997.
- [13] Mark W. Spong, Seth Hutchinson, and M. Vidyasagar. *Robot Dynamics and Control*. 2nd ed. Wiley, 2005.
- [14] Lorenzo Sciavicco and Bruno Siciliano. *Modelling and Control of Robot Manipulators*. 2nd ed. Lorenzo Sciavicco and Bruno Siciliano. London: Springer, 2012.
- [15] Karl Johan Åström and Katsuhisa Furuta. “Swinging up a pendulum by energy control”. In: *Automatica* 36.2 (2000), pp. 287–295.
- [16] Hassan K. Khalil. *Nonlinear Systems*. 3rd ed. 2015.
- [17] Morten H. Knudsen. “Experimental modeling of dynamic systems: an educational approach”. In: *IEEE Transactions on Education* 49.1 (Feb. 2006), pp. 29–38.

## Appendix Bibliography

- [18] Michael S Triantafyllou and Franz S Hover. *Maneuvering and control of marine vehicles*. Massachusetts of Institute of Technology, 2003.
- [19] Gene F Franklin et al. *Feedback control of dynamic systems*. Addison-Wesley Reading, MA, 1994.
- [20] *lqrd*. 2018. URL: <https://se.mathworks.com/help/control/ref/lqrd.html>.
- [21] F Haugen. “Kompendium for Kyb. 2, ved Høgskolen i Oslo, Telemark University College, Department of Electrical Engineering”. In: *Information Technology and Cybernetics* (2015).
- [22] Matthew B Rhudy, Roger A Salguero, and Keaton Holappa. “A Kalman Filtering Tutorial For Undergraduate Students”. In: *International Journal of Computer Science & Engineering Survey (IJCSES)* 8 (2017), pp. 1–18.
- [23] T. Dutoit and F. Marques. *Applied Signal Processing: A MATLAB™-Based Proof of Concept*. US: Springer, 2010.

**Swing-up and Stabilization of a Cart  
Pendulum and Twin Pendulum System**  
Using Nonlinear Control Strategies

Niels Skov Vestergaard  
January 2019

Control & Automation

Aalborg University  
Department of Electronic Systems  
Fredrik Bajers Vej 7  
9220 Aalborg Øst



**AALBORG UNIVERSITY**  
DENMARK